Universiteit Leiden
The Netherlands

Mechanisms of Ewing sarcoma metastasis : biochemistry and biophysics

Beletkaia, E.

Citation

Beletkaia, E. (2015, December 9). *Mechanisms of Ewing sarcoma metastasis : biochemistry and biophysics*. Retrieved from https://hdl.handle.net/1887/37000

Version:	Not Applicable (or Unknown)
License:	Leiden University Non-exclusive license
Downloaded from:	https://hdl.handle.net/1887/37000

Note: To cite this publication please use the final published version (if applicable).

Cover Page

Universiteit Leiden

Leiden University Repository

The handle http://hdl.handle.net/1887/37000 holds various files of this Leiden University dissertation.

Author: Beletkaia, Elena
Title: Mechanisms of Ewing sarcoma metastasis : biochemistry and biophysics
Issue Date: 2015-12-09

Mechanisms of Ewing Sarcoma Metastasis

Biochemistry and Biophysics

PROEFSCHRIFT

ter verkrijging van
de graad van Doctor aan de Universiteit Leiden,
op gezag van Rector Magnificus prof. mr. C.J.J.M. Stolker,
volgens besluit van het College voor Promoties
te verdedigen op woensdag 9 december 2015
klokke 10.00 uur

door

Elena Beleţkaia

geboren te Chişinău (Moldova)
in 1989

Promotor: Prof. dr. T. Schmidt
Co-promotor: Dr. B. E. Snaar-Jagalska

Promotiecommissie:

Dr. S. F. Fenz (Julius-Maximilians University, Würzburg, Germany)
Prof. dr. M. Bünemann (Philipps University, Marburg, Germany)
Prof. dr. M. Dogterom
Prof. dr. E. Eliel
Prof. dr. P. C. W. Hogendorn

ISBN 978-90-8593-234-5
Casimir PhD series Delft-Leiden 2015-28
An electronic version of this thesis can be found at
https://openaccess.leidenuniv.nl

This work is part of the research programme TOPGO.L.10.064, which is financed by the Netherlands Organisation for Scientific Research (NWO).

For Katherine

Contents

1 Introduction **1**
1.1 Ewing sarcoma 3
1.2 Ewing sarcoma's origin 4
1.3 EWS/FLI fusion protein 5
1.4 CXCR4 6
1.4.1 CXCR4 structure 6
1.4.2 Activation mechanism 8
1.4.3 CXCR4 signaling 8
1.4.4 CXCR4 in cancer metastasis 9
1.5 Ewing sarcoma metastasis 10
1.5.1 CXCR4 in ES metastasis 10
1.5.2 Other modulators of ES metastasis 10
1.5.3 Anchorage-independent growth 11
1.6 Cancer mechanics 12
1.6.1 Cellular stiffness 12
1.6.2 Role of the extracellular matrix 12
1.7 Thesis outline 14
1.8 Appendix 16
1.9 References 19

2 CXCR4 signaling control **29**
2.1 Introduction 31
2.2 Materials and Methods 33
2.2.1 Cell culture and transfection 33
2.2.2 Sample preparation 33
2.2.3 Global CXCL12 stimulation assay 33
2.2.4 Calcium assay 33
2.2.5 Actin depolymerization 34

2.2.6 Endocytosis inhibition 34
2.2.7 $G_{\alpha i}$ inhibition 34
2.2.8 Single-molecule imaging 34
2.2.9 Time-lapse microscopy 36
2.2.10 Simulation of diffusion on a vesicle 36
2.3 Results 37
2.3.1 CXCR4-eYFP is functional in A673-CXCR4 cells . 37
2.3.2 CXCR4 do not homodimerize upon activation in A673 cells 39
2.3.3 Activation of CXCR4 causes immobilization of the receptors 41
2.3.4 Actin cytoskeleton is not responsible for CXCR4 immobilization 43
2.3.5 CXCR4 in endocytotic vesicles contribute to the immobile receptor fraction 45
2.3.6 G-proteins control CXCR4 immobilization 47
2.3.7 Cross-talk between G-protein dependent and independent pathways 48
2.4 Discussion 50
2.5 Supplemental figures 55
2.6 Acknowlegement 57
2.7 References 58

3 G-protein activation mode by CXCR4 65
3.1 Introduction 67
3.2 Materials and Methods 69
3.2.1 Cell culture and transfection 69
3.2.2 Confocal microscopy 69
3.2.3 Single-molecule imaging 69
3.3 Results 70
3.3.1 Receptor interaction is required for G-protein localization to the plasma membrane 70
3.3.2 Mobility of membrane proteins is unaltered on cell-substrate adhesion 74
3.3.3 Binding of $G_{\alpha i}$ to CXCR4 requires receptor activation 76
3.3.4 $G_{\alpha q}$ is pre-coupled to an inactive CXCR4 receptor 78
3.4 Discussion 79
3.5 Acknowlegement 82

3.6 References 83

4 Construction of optoCXCR4 87
4.1 Introduction 89
4.2 Materials and Methods 91
4.2.1 Cell culture 91
4.2.2 Sequences alignments 91
4.2.3 Whole-plasmid cloning 92
4.2.4 Cell transfection 92
4.2.5 Microscopy 92
4.2.6 Dual reporter activity assay 93
4.3 Design and characterization of an optoCXCR4 receptor . . 94
4.3.1 Design of optoCXCR4 94
4.3.2 Cloning of various optoCXCR4 constructs 96
4.3.3 Optimization of cell transfection 99
4.3.4 Localization of the chimeric receptors 100
4.3.5 Functionality of the optoCXCR4 constructs 102
4.3.6 Fast optoCXCR4 internalization 103
4.4 Conclusions 104
4.5 Supplemental figures 106
4.6 Acknowlegement 108
4.7 References 109

5 Mechanics of ES metastasis 113
5.1 Introduction 115
5.2 Materials and Methods 116
5.2.1 Cell culture and viral transfection 116
5.2.2 Collagen gel assay 117
5.2.3 Micropillar preparation 117
5.2.4 Microscopy 118
5.2.5 Force detection 119
5.2.6 Immunostaining 119
5.2.7 Cell area detection 119
5.2.8 2D migration rate detection 119
5.3 Results 120
5.3.1 Cell phenotype depends on substrate modification 120
5.3.2 Cell invasion in 3D is stiffness dependent 122
5.3.3 Ewing sarcoma cells change their mechanical phenotype on micropillar arrays of varying stiffness . 124

5.3.4 Dynamic force development depends on substrate stiffness 126
5.3.5 Activation of cells did not alter their morphological and mechanical phenotype 128
5.4 Discussion 130
5.5 Supplemental figures 133
5.6 References 136

Summary **141**

Samenvatting **145**

Publications **149**

Curriculum Vitae **151**

Chapter 1

Introduction

1.1 Ewing sarcoma

Ewing sarcoma (ES) is a special type of bone cancer, first described by Dr. James Ewing in his paper 'Diffusive endothelioma of bone' (Ewing, 1972; Appendix 1). Gathered under a common name and further referred as Ewing sarcoma (ES for short) this group of aggressive neoplasms includes Ewing sarcoma of bone, extra-skeletal Ewing sarcoma, Askin tumor and peripheral primitive neuroectodermal tumor (Delattre et al., 1994; Iwamoto, 2007; Potratz et al., 2012). Today Ewing sarcoma represents the second most common bone cancer among adolescents and young adults (Delattre et al., 1994; Lamhamedi-Cherradi et al., 2014; Ludwig, 2008). About 80% of the patients diagnosed with Ewing sarcoma are younger then 20 years old. It is rarely diagnosed in patients older then 30-40 years old (Iwamoto, 2007; Karosas, 2010). To the present day the oldest patient documented case of Ewing sarcoma belongs to a 85 years old female patient (Monument et al., 2015).

Ewing sarcoma predominantly develops in bone with the most common sites being the long bones (Fig. 1.1; Barker et al., 2005; Iwamoto, 2007; Karosas, 2010; Ludwig, 2008; Potratz et al., 2012). In soft tissues Ewing sarcoma may develop in older patients. The earliest symptom of ES is pain, followed by swelling and fever (Iwamoto, 2007; Karosas, 2010). Ewing sarcoma is often overlooked (Karosas, 2010; Nedelcu et al., 2014), the diagnosis frequently is delayed by weeks and up to years (Ludwig, 2008; Nedelcu et al., 2014). The increased time to ES diagnosis is primarily associated with older age of patient and tumor site (Brasme et al., 2014). Tumor sites associated with increased time to diagnosis are skull, ribs, vertebrae, limbs, pelvis, and hand or foot (Brasme et al., 2014). Innumerous studies together with the development of chemotherapy (1962) and multi-modal cancer-treatment protocols increased the 5-years survival rate for Ewing sarcoma patients with localized tumor from 10% to 70% (Iwamoto, 2007; Karosas, 2010; Lamhamedi-Cherradi et al., 2014; Liebner, 2015; Potratz et al., 2012). Patient survival and metastasis formation was shown to be not significantly associated with time to diagnosis (Brasme et al., 2014). However, in more then half of the diagnosed Ewing sarcoma cases micrometastases are presumed to be present (Lamhamedi-Cherradi et al., 2014). Contrary to the positive achievement in treatment of localized tumors, the long-term (5-years) survival for Ewing sarcoma patients with metastasis, however, remain below the 30% mark (Lamhamedi-Cherradi et al., 2014; Ludwig, 2008;

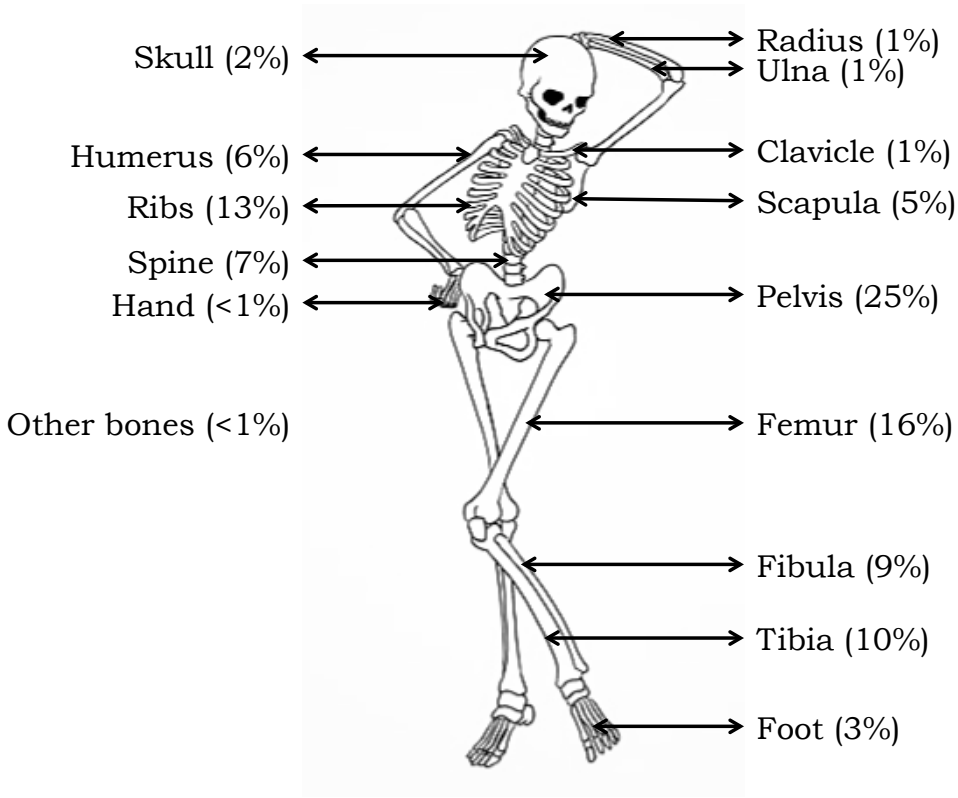

Figure 1.1
Representation of Ewing sarcoma distribution sites in human skeleton.

Potratz et al., 2012). Hence, a better understanding of the processes underlying Ewing sarcoma metastasis deserves additional attention.

1.2 Ewing sarcoma's origin

First Ewing sarcoma cell lines were established in 1970's. However, often cells put in culture were initially mistakenly described as neuroblastoma (Schlesinger et al., 1976), rhabdomyosarcoma (Giard et al., 1973), lymphoid cells or others. Only later characterized as Ewing sarcoma (Martinez-Ramirez et al., 2003; Whang-Peng et al., 1986), these cells raised a question of a common cell origin of Ewing sarcoma. There is evidence indicating that Ewing sarcoma derives from mesenchymal cells (Kovar, 2014; Pagani et al., 1995). Other studies show that Ewing sarcoma originates from pluripotent cells with blocked differentiation (Kovar, 2005). Lately an increasing number of reports of cellular studies

suggest a neuronal origin of: CADO (Kodama et al., 1991), SS-ES-1 (Hatori et al., 2006) and other cell lines (Cavazzana et al., 1987). However, poor differentiation and the stem cell like phenotype of Ewing sarcoma cells keep the cellular origin of Ewing sarcoma unresolved (Sand et al., 2015). A better understanding of Ewing sarcoma origin would, hence, potentially uncover mechanisms that control ES growth, progression and metastasis leading to novel therapeutic strategies.

1.3 EWS/FLI fusion protein

Histologically Ewing sarcoma is identified as a small round cell tumor. Over 90% of tumors are positive for the surface antigen MIC2 (CD99) (Potratz et al., 2012). Cytogenetically Ewing sarcoma is characterized by a specific chromosomal translocation t(11;22) (Aurias and Desmaze, 1992; Fraccaro et al., 1980; Iselius et al., 1983; Turc-Carel et al., 1988). In 80% of the cell lines and 90% of the primary Ewing tumors this translocation is detectable (Dockhorn-Dworniczak et al., 1994). Thus, presence of the t(11;22) translocation became the accepted hallmark in the differential diagnosis and prognosis of Ewing sarcoma (Dockhorn-Dworniczak et al., 1994; Turc-Carel et al., 1988). There is a slight variation in breaking points of this reciprocal translocation. The most common, occurring 85% of the time, involve band q12 and band q24 of chromosome 22 and chromosome 11, t(11;22)(q24;q12) (Zucman et al., 1992). Translocation results in the expression of the fusion protein EWS-FLI-1 (Delattre et al., 1994; Dockhorn-Dworniczak et al., 1994; Ludwig, 2008). Less common, occurring 5-8% of the time, is the fusion protein EWS-ERG and, occurring in less than 1% of the time, the fusion proteins EWS-ETV1, EWS-EIAF, or EWS-FEV (Delattre et al., 1994; Dockhorn-Dworniczak et al., 1994) . The fusion protein EWS/FLI-1 was shown to act as a strong transcriptional activator (May et al., 1993; Sand et al., 2015) that interferes with the expression of many genes. Key proteins of various pathways like IGF-1R, mTOR, MAPK, PI3K/Akt, EGFR, VEGF and others were found to be disregulated (Ludwig, 2008). For instance, influenced by EWS-FLI-1, the IGF-1R pathway appears to be constitutively activated in Ewing sarcoma and subsequently emerge as a key player in the malignant transformation (Ludwig, 2008). Moreover over-expressed *in vitro* or *in vivo*, EWS-FLI-1 promotes cell growth and facilitates susceptibility to chemotherapy (Ludwig, 2008). Hence, EWS/FLI potentially

plays a central role in Ewing sarcoma progression and metastasis.

Another evidence supporting the above conclusion is a high involvement of EWS/FLI in regulation of the chemokine receptor CXCR4. CXCR4 was shown to correlate with Ewing sarcoma metastasis (see below) and poor prognosis for patients (Bennani-Baiti et al., 2010; Kim et al., 2010).

1.4 CXCR4

In 1994 for the first time a leukocyte-derived seven-transmembrane domain receptor (LESTR) cDNA was isolated. The high expression of LESTR in white blood cells was suggested to play a role in inflammation. (Loetscher et al., 1994). In May 1996 using a cDNA cloning strategy an HIV-1 cofactor was isolated, which supposedly was identified as G-protein coupled receptor with seven-transmembrane domain structure. This cofactor was shown to promote HIV-1 fusion and virus entry to CD4+ cells. Therefore, the protein was designated as Fusin. (Feng et al., 1996). The discovery of Fusin was a real breakthrough in HIV-1 research (Broder and Dimitrov, 1996; Cohen, 1996). LESTR and Fusin happened to be the same receptor. In August 1996 the stromal-derived factor-1 (SDF1, later designated as CXL12) has been reported as specific chemoattractant ligand to LESTR/Fusin (Bleul et al., 1996; Oberlin et al., 1996). Since then the previously orphan chemokine receptor was designated as CXC chemokine receptor 4, short CXCR4 (Bleul et al., 1996). SDF-1 binding to CXCR4 was shown to be a strong inhibitor of infection by HIV-1 (Bleul et al., 1996), due to the role of the CXCR4 ligand-binding domain in HIV-1 entry (Picard et al., 1997). In 2001 the involvement of CXCR4 in breast cancer metastasis was suggested (Muller et al., 2001). This initial association was subsequently followed by reports, proving the role of CXCR4 in metastasis of a broad spectrum of cancer types. Up to date, the function of CXCR4 as co-receptor for HIV entry and its role as cancer metastasis promoter made it the best-studied human chemokine receptor (Furusato et al., 2010). Nevertheless, a lot of molecular details of CXCR4 function stayed yet undiscovered.

1.4.1 CXCR4 structure

The chemokine C-X-C motif receptor 4 (CXCR4) is one of ∼20 described human chemokine receptors. CXCR4 belong to the superfamily of G-

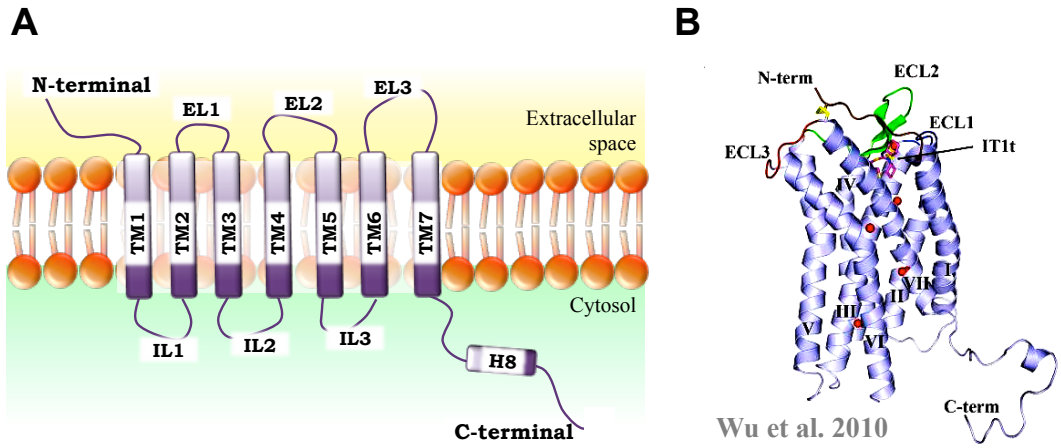

Figure 1.2
CXCR4 structure. ***A.*** *A schematic representation of the structure of any G-protein coupled receptor, consisting of an extracellular N-terminus, three extracellular loops (EL), seven transmembrane (TM) α-helixes, three intracellular loops (IL), an amphipathic helix H8 and an intracellular C-terminus.* ***B.*** *Crystal structure of chemokine receptor CXCR4 (from Wu et al., 2010).*

protein coupled receptors (GPCRs). Constituting about 800 genes of the human genome GPCRs share a common seven-transmembrane α-helix protein structure (Fig. 1.2). CXCR4 is one of the few GPCRs and the only chemokine receptor of which the structure was successfully resolved by X-ray crystallography (Wu et al., 2010; Fig. 1.2B). The structure showed a remarkable resemblance with the resolved structure of rhodopsin (Palczewski et al., 2000) and predicted earlier structures of other GPCRs (Costanzi et al., 2009). The common structure of G-protein coupled receptors consists of an extracellular N-terminus, three extracellular loops (EL1-EL3), seven transmembrane α-helixes (TM1-TM7), three intracellular loops (IL1-IL3), a small intracellular amphipathic helix (H8) and an intracellular C-terminus (Fig. 1.2A). Some GPCRs, e.g. CXCR4, are lacking the amphipathic helix. Each part of GPCR has its recognized role during receptor activation (Rajagopalan and Rajarathnam, 2006; Rosenkilde et al., 2000; Venkatakrishnan et al., 2013). The N-terminus and the EL are responsible for specific ligand recognition and modulation of the ligand access. The C-terminus and the IL are responsible for modulation of receptor activity and downstream signaling. The TM region is a communication link between extracellular and intracellular part of the receptor.

1.4.2 Activation mechanism

CXCR4 ligand, CXCL12, binding is a two step process. Initial interaction between the ligand and the N-terminus lead to conformational changes of the receptor by which a stable interaction of the ligand with the exposed binding pocket in CXCR4 occurs (Busillo and Benovic, 2006). Disulphide bridges in the extracellular region contribute to receptor stability (Venkatakrishnan et al., 2013). Agonist binding disrupts the existing intramolecular interactions within CXCR4 and promotes formation of interactions, which result in energetically favorable conformational rearrangements of the receptor (Wess et al., 2008). The conformational rearrangements mainly involve the transmembrane region of the receptor and can be summarized as: (1) small local structural changes in the TM5; (2) relocation of TM3 and TM7; (3) translation/rotation of TM5 and TM6 (Venkatakrishnan et al., 2013). TM7 together with TM6 are bending inwards towards TM3 (Hoffmann et al., 2008) resulting in the formation of cross-linking disulfide bonds between the cytoplasmic ends of TM3 and TM7 (Wess et al., 2008). TM helix 6 undergoes the largest movement (Hoffmann et al., 2008; Wess et al., 2008) resulting in reorientation of its cytoplasmic end. It was demonstrated that the rotational movement of the cytoplasmic end of TM6 (Hoffmann et al., 2008) causes a conformational change of the third intracellular loop (Hoffmann et al., 2008; Wess et al., 2008). The conformational change in IL3 subsequently induces activation of G-protein dependent signaling pathways (Roland et al., 2003) as the main signal transduction mechanism.

1.4.3 CXCR4 signaling

Activation of CXCR4 triggered by its specific agonist CXCL12 is a complex process. Binding of CXCL12 to CXCR4 initiates receptor signaling through four different G_α subunits (Rubin, 2008), resulting in PCLβ-, Cdc42-, Akt-, Erk-, and Rho- dependent biochemical cascade activation. Additionally, G-proteins independent pathways are activated, resulting in C-terminal phosphorylation and activation of the β-arrestin pathway leading to receptor internalization and β-arrestin signaling, respectively (for a review see: Busillo and Benovic, 2006; Rubin, 2008; Teicher and Fricker, 2010). The filigreed regulation and precise control over these various pathways finally result in a ligand-specific cellular reaction including gene expression, cell proliferation, cell growth and cell migration. The

latter is the key outcome on CXCL12-dependent chemotaxis. Chemotaxis, the directional cell migration in a gradient of a ligand, is refered to as the central process during angiogenesis, embryogenesis, stem cell homing, as well as inflammation and cancer metastasis (Kryczek et al., 2007; Teicher and Fricker, 2010). Hence, CXCR4 is recognized as a chemokine receptor actively promoting cell migration during cancer metastasis.

1.4.4 CXCR4 in cancer metastasis

Breast, lung, ovarian, renal, prostate and other cancer cells were shown to express high levels of CXCR4. In breast cancer (Muller et al., 2001), prostate cancer (Wang et al., 2005), lung cancer (Phillips et al., 2003) and others elevated CXCR4 expression has been associated with metastatic disease and poor prognosis. Cancer cells exhibit expedited proliferation in response to CXCL12 stimulation, while in their healthy counterparts CXCL12-induced apoptosis was detected (Rubin, 2008). Thus, a model was proposed, suggesting a different kinetics of the CXCR4 signaling in cancer cells. The changed kinetics would cause overlap in G-protein dependent and independent pathways in such a way, that it results in the altered cellular response (Rubin, 2008).

CXCR4 was suggested to promote tumor progression by increased cell growth, induction of angiogenesis towards the tumor tissue and formation of metastasis (Berghuis et al., 2012; Jin et al., 2012). The interruption of CXCL12/CXCR4 signaling was shown to inhibit the metastatic processes (Krook et al., 2014; Muller et al., 2001; Vandercappellen et al., 2008). It was suggested that the high level of CXCL12 expression in tissues such as lungs, liver, lymph nodes and bone marrow defines them as main target sites for cancer metastasis driven by CXCR4 chemotaxis (Kim et al., 2010; Raman et al., 2007; Vandercappellen et al., 2008). Hypoxia, which typically accompanies tumor formation, was further suggested to induce tumor-specific CXCL12 expression, which potentially initiate angiogenesis towards the tumor (Kryczek et al., 2007; Raman et al., 2007). At the same time the decreased oxygen concentration within the tumor was shown to up-regulate CXCR4 expression further promoting cell migration out of primary tumor and metastasis.

1.5 Ewing sarcoma metastasis

Ewing sarcoma metastases occur at early stage of the tumor development. The primary sites of metastasis are lungs, other bones and/or the bone marrow. Metastasis to other tissues occurs in less then 1% of all cases. (Potratz et al., 2012). Thus, Ewing sarcoma exhibits a very unique metastasis phenotype, which is by far not well understood.

1.5.1 CXCR4 in ES metastasis

Similar to other cancer types, hypoxia results in up-regulation of CXCR4 expression in Ewing sarcoma. Additionally EWS/FLI1 result in up-regulation of CXCR4 expression. In turn, cells overexpressing CXCR4 display an increased chemotactic migration and invasion (Krook et al., 2014). Cell lines derived from ES patients with metastasis at diagnosis exhibited significantly higher expression level of CXCR4, compared to cell lines derived from patients with solid tumor only (Bennani-Baiti et al., 2010). The same increase of CXCR4 expression in metastasis compared to solid tumors was shown when speciments from the patients were analyzed (Jin et al., 2012). Thus, CXCR4 expression is correlated with Ewing sarcoma progression (Berghuis et al., 2012; Jin et al., 2012). Expression of CXCR4 in Ewing sarcoma is highly dependent on EWS-FLI1 (Bennani-Baiti et al., 2010) and is rapidly and reversibly modulated (Krook et al., 2014). The only other chemokine receptor regulated by EWS-FLI1 is the orphan-receptor CXCR7. As CXCR4 it binds to CXCL12, however CXCR7 activation is not followed by activation of G-protein signaling. Therefore, CXCR7 is considered to be a regulatory protein for CXCR4 signaling. Evidences suggest that CXCR7 plays a role in CXCL12 scavenging (Sun et al., 2010). However, hight CXCR7 expression in addition to high expression of CXCR4 in Ewing sarcoma was shown to be correlated with worse patient survival prognosis (Bennani-Baiti et al., 2010; Krook et al., 2014).

1.5.2 Other modulators of ES metastasis

Many other pathways and molecules were shown to contribute to Ewing sarcoma metastasis regulation. Chemokine receptor CXCR6 expression in tumor cells correlated with metastasis formation, while its ligand, CXCL16, was associated with localization of the metastasis in lungs

(Na et al., 2014). The orphan G-protein coupled receptor GPR64 was shown to specifically over-express in Ewing sarcoma. GPR64 promoted invasiveness and metastatic spread of Ewing sarcoma, while inhibition of GPR64 resulted in a reduced colony formation in vitro, and suppressed growth and metastasis of the tumor in vivo (Richter et al., 2013).

High levels of interleukin 6 expression in the tumor stroma of primary ES suggest a biological relevance of this cytokine in ES pathogenesis and, thus, mediate formation of metastases (Lissat et al., 2015). Pretreatment of Ewing sarcoma cells with stem cell factor (SCF) prevented metastasis formation in lungs in mice model (Landuzzi et al., 2000).

Also metalloproteinase (MMP) 2 and 9 activity correlats with ES cell invasion (Odri et al., 2014; Sainz-Jaspeado et al., 2010). Caveolin 1 (CAV1) involved in regulation of MMP and SPARC expression plays a key role in ES metastasis and lung colonization (Sainz-Jaspeado et al., 2010). Inhibition of the MMP 2 and 9 with zoledronic acid resulted in the decrease of spontaneous lung metastases dissemination from primary ES but not in the decrease the growth of prior lung metastases (Odri et al., 2014).

1.5.3 Anchorage-independent growth

Hypoxia condition in the tumor tissue induces accumulation of the hypoxia inducible factor (HIF)-1α in a big fraction of primary ES (Aryee et al., 2010). Ewing sarcoma cells adapt to hypoxia condition by modulating EWS-FLI1-dependent transcriptional signature (Aryee et al., 2010; Krook et al., 2014). Together with other micro-environmental stresses hypoxia promotes CXCR4-mediated Ewing sarcoma cell migration (Krook et al., 2014), invasiveness and anchorage-independent growth (Aryee et al., 2010). In turn, an anchorage-independent growth phenotype was shown to predict a severe metastatic potential of primary breast and lung tumors (Mori et al., 2009).

The adhesion of Ewing sarcoma cells is largely modulated by EWS-FLI1 (Chaturvedi et al., 2012; Chaturvedi et al., 2014). EWS/FLI reduce expression of zyxin and α_5 integrin (Chaturvedi et al., 2014), which causes the loss of organized actin stress fibers and focal adhesions (Chaturvedi et al., 2012), thereby promoting the loss of the cell spreading and enhance their capacity to grow in anchorage-independent conditions. Ewing sarcoma cells growing in anchorage-independent conditions form multicellular spheroids (Kodama et al., 1991; Landuzzi et

al., 2000; Paszek et al., 2005). While growing in spheroids cells show a considerably different phenotype compared to their monolayer counterparts. Ewing sarcoma spheroids show reduced proliferation, highly developed cell-cell junctions and anoikis resistance. Such phenotypic change is a prerequisite for the successful development of metastases as well as pronounced resistance to chemotherapy. (Strauss et al., 2010).

1.6 Cancer mechanics

1.6.1 Cellular stiffness

Besides cellular adhesion, expression of EWS/FLI largely changes the cytoskeleton of Ewing sarcoma cells. EWS/FLI expression induces a loss of well-defined stress fibers leading to a significant change in the cyto-architecture on ES cells (Chaturvedi et al., 2014). A depleted actin network was shown to be associated with a more aggressive phenotype in colon cancer (Palmieri et al., 2015). Mechanically the weakening of the cytoskeleton network leads to lower cell stiffness, which in turn increase their deformability and migratory capacity (Agus et al., 2013; Katira et al., 2013; Palmieri et al., 2015). Atomic force microscopy studies indicate that cancer cells are softer than normal cells (Hayashi and Iwata, 2015). Moreover, different stages of cancer can result in different changes of the mechanical phenotype of the cells (Katira et al., 2013). Metastatic colon cancer cells appear more modified, in terms of cell stiffness and actin network organization, compared to the cells from the primary tumor (Pachenari et al., 2014; Palmieri et al., 2015). The more aggressive cancer cells exhibit a decreased viscosity (Pachenari et al., 2014) and an increase in the non-specific adhesion toward substrates (Palmieri et al., 2015). The adhesion capacity of the cells is primarily attained through integrins, as integrins physically connect the cellular cytoskeleton to the extracellular matrix (ECM). Thus, an altered expression of integrins is thought to modulate cancer cells' phenotype. (Jansen et al., 2015).

1.6.2 Role of the extracellular matrix

Malignant tissues dynamically remodel the extracellular matrix (ECM) around them (Gill and West, 2014; Janmey et al., 2013; Jansen et al., 2015; Katira et al., 2013; Tung et al., 2015). Unlike individual cells, the overall tumor stiffness is increased compared to the normal tissue

(Gill and West, 2014). This effect is reached through more dense cellular packing and an excessive production of ECM (Gill and West, 2014; Tung et al., 2015). Increased tissue stiffness contributes to further tumor progression and, potentially, metastasis (Janmey et al., 2013; Sapudom et al., 2015; Tung et al., 2015). Some models suggest that the invasive morphology of cells is promoted through an increase of the stiffness of the cellular microenvironment (Katira et al., 2013). Mechanical stresses regulate cellular metabolism (Tung et al., 2015) and have a pronounced effect on cell proliferation (Janmey et al., 2013; Taloni et al., 2014). The ECM stiffness-dependent miRNA expression is mediating malignancy of breast epithelium (Mouw et al., 2014). Taken together, the cellular microenvironment and in particular the ECM has a significant impact on the metastatic profile of cancer cells.

1.7 Thesis outline

In this thesis a report on experimental work aiming for a better understanding of the mechanisms underlying Ewing sarcoma metastasis is presented. Two distinct mechanisms are investigated: (1) a biochemical approach in which the initial steps in the CXCR4 signaling cascade are followed, and (2) a biophysical approach in which the guidance of EW metastasis by the stiffness of their microenvironment is demonstrated.

In **Chapter 2** the molecular mechanism of chemokine receptor CXCR4 signaling in a model Ewing sarcoma derived cell line A673 is studied using the single-molecule imaging technique. Effects of activation-dependent dimerization, internalization and G-protein interaction are tested. Measurements in resting cells and cells stimulated with CXCL12 revealed an activation-dependent mobility change of CXCR4. The mobility change is shown to be associated with G protein-dependent and independent pathways. Data indicated a functional cross-talk between different biochemical cascades.

In **Chapter 3** the regulation of CXCR4 signaling in Ewing sarcoma is further addressed by investigation of the receptor interaction with the respective G-proteins. Two different G_{α}-subunits exhibited a differential coupling mode to CXCR4. Thereby, data indicated that $G_{\alpha q}$ and $G_{\alpha i}$ interact with the receptor in a sequential manner. The sequential receptor/G-protein interaction was correlated with the timing of the following signaling cascades, which might reflect a potential mechanism for pathway-specific signal regulation.

In **Chapter 4** a newly emerging approach of optogenetics was exploited to develop an all optically-controlled chimeric receptor optoCXCR4. A detailed description of the design of a chimeric receptor is present together with various experiments to test for proper functionality. The developed construct represents a promising tool for further biophysical investigation of chemokine receptor CXCR4 signaling, that permits external cellular control at high temporal and spatial resolution.

In **Chapter 5** a hypothesis of the mechanical guidance of Ewing sarcoma metastasis was examined. The influence of the mechanical properties of the microenvironment on ES was tested in 2D and 3D assays. Various Ewing sarcoma derived cells exhibited an evident difference in mechanical phenotype depending on their metastatic niche. The softer microenvironment appeared more attractive for cells derived from patients with lungs metastasis localisation, while stiffer substrates resulted

in higher adhesion potential for cells derived from patients bone metastasis localization. Notably, activation of the CXCR4 receptor had no evident effect on the mechanical phenotype.

1.8 Appendix

The history of Ewing sarcoma starts in 1920's, when the pathologist J. Ewing published his first work on a new kind of bone cancer.

James Ewing, born in 1866, graduated from Columbia University College of Physicians and Surgeons in 1891. In 1899 Ewing became the first professor of pathology at Cornell University Medical College (Huvos, 1998). In 1913 Ewing became the first Director of Pathology at present-day Memorial Sloan-Kettering Cancer Center in New York City (then called New York Cancer Hospital) (Huvos, 1998; www.mskcc.org). In 1931, after his retirement from Cornell as Chairman of the Department of Pathology, Ewing became the Director of Memorial Hospital for Cancer and Allied Diseases (Huvos, 1998).

At the time Ewing was one of the central figures in many aspects of cancer-related research and owned to be named "Cancer Man" by the Times Magazine (Fig. A1) (www.time.com). His work was considered as an excellent starting point for any aspect of oncology (Shimkin, 1974). Under J. Ewing guidance the New York Cancer Hospital became worldwide recognized in the diagnosis and management of neoplastic diseases (www.mskcc.org). He was a 'father' of the American Society of the Cancer Control (A.S.C.C., 1913) (Triolo and Shimkin, 1969), and President of the American Association for Cancer Research (AACR) in 1907-09 (Triolo and Riegel, 1961). As member of the AACR Ewing was involved in the establishment of Journal of Cancer Research (Cancer Research at present-day) in 1916, and its reformation into the American Journal of Cancer in 1930 (Triolo and Riegel, 1961).

In 1919 the first edition of Ewing book 'Neoplastic Diseases: A Text-Book on Tumors' was published (Ewing, 1922). The book gave a comprehensive overview and classification of the available studies on neoplastic diseases (Ewing, 1922; Huvos, 1998) and provided a systematic basis for diagnosing human cancer, representing a keystone of modern oncology (www.mskcc.org). Already in 1922 the second edition of the book was published. It included studies collected over the past two years, new microphotographs and a major correction on 'Tumor of bone' chapter (Ewing, 1922). In his book (and lectures) Ewing described a special case of a 14-year-old girl patient with a large tumor of the ulna (Ewing, 1922; Huvos, 1998). The most abundant treatment at the time was amputation. However, given his personal history of facing a potential leg amputation at age of 14, Ewing was not in favor of such solution for

Figure A1
'Cancer man'

his patient. A treatment with only x-ray irradiation was used instead. The treatment resulted in disappearance of the tumor (Huvos, 1998). Together with multiple similar cases, this observation and collaborative work with Dr. Douglas lead to foundation of a radium department in the New York Cancer Hospital in 1915, and thus gave birth to radiation therapy in the United States (www.mskcc.org; Huvos, 1998).

Ewing noticed, that radiosensitivity was shared by a specific type of bone sarcoma, characterized by the typical microscopic appearance and known as round cell sarcoma. He described his observations and the 14-year-old girl case in his first publication on a new kind of malignant osteoma - 'diffuse endothelioma of bone' in 1921 (Choudhury et al., 2011; Ewing, 1972; Huvos, 1998). This is were the origin of the long history of Ewing sarcoma takes its start.

By 1927 there were more case reports with symptoms similar to the 'new' bone cancer. Representing 7% of the total bone cancer reports at the time, it was appointed the name 'Ewing sarcoma' (Pritchard, 1927). Extensive research and development in cytogenetics resulted in the establishment of the common chromosomal translocation which became characteristic to Ewing sarcoma in 1980's (Fraccaro et al., 1980; et al.,

1983; Turc-Carel et al., 1988). Around 1987 the break points of reciprocal translocation at 11q24 and 22q12 were confirmed to be uniform for Ewing sarcoma. In 1994 the resulting fusion-protein was identified (Delattre et al., 1994). From then on the presence of the fusion-proteins EWS/FLI or EWS/ERG became a defining criterion for Ewing sarcoma (Delattre et al., 1994).

Today Ewing sarcoma is the second most common bone cancer in children and young adults. The average patients age is 13 years with a range from 1 to 48 years. It is described as small-round cell tumor and identified by molecular genetic analysis for the t(11,22)q(24;12) translocation and the expression of EWS/FLI or EWS-ERG. (Delattre et al., 1994; Dockhorn-Dworniczak et al., 1994; Ludwig, 2008; Sand et al., 2015).

Ewing worked through his life to better understand and search ways to fight the disease of cancer. He made a huge impact, particularly on the cancer of bone. Through almost 100 years Ewing sarcoma still holds the name of a great pathologist and oncologist of early 20th century James Ewing. Tragically himself Ewing succumbed to bladder carcinoma in 1943 (Huvos, 1998).

1.9 References

Agus, D. B., Alexander, J. F., Arap, W., Ashili, S., Aslan, J. E., Austin, R. H., Backman, V., Bethel, K. J., Bonneau, R., Chen, W.-C. C., et al. (2013). A physical sciences network characterization of non-tumorigenic and metastatic cells. Sci Rep 3, 1449.

Aryee, D. N., Niedan, S., Kauer, M., Schwentner, R., Bennani-Baiti, I. M., Ban, J., Muehlbacher, K., Kreppel, M., Walker, R. L., Meltzer, P., et al. (2010). Hypoxia modulates EWS-FLI1 transcriptional signature and enhances the malignant properties of Ewing's sarcoma cells in vitro. Cancer Res. 70, 4015-23.

Aurias, A. and Desmaze, C. (1992). Cytogenetics of Ewing's sarcoma. Pathol. Biol. 39, 951.

Barker, L. M., Pendergrass, T. W., Sanders, J. E. and Hawkins, D. S. (2005). Survival after recurrence of Ewing's sarcoma family of tumors. J. Clin. Oncol. 23, 4354-62.

Bennani-Baiti, I. M., Cooper, A., Lawlor, E. R., Kauer, M., Ban, J., Aryee, D. N. and Kovar, H. (2010). Intercohort gene expression co-analysis reveals chemokine receptors as prognostic indicators in Ewing's sarcoma. Clin. Cancer Res. 16, 3769-78.

Berghuis, D., Schilham, M. W., Santos, S. J., Savola, S., Knowles, H. J., Dirksen, U., Schaefer, K.-L. L., Vakkila, J., Hogendoorn, P. C. and Lankester, A. C. (2012). The CXCR4-CXCL12 axis in Ewing sarcoma: promotion of tumor growth rather than metastatic disease. Clin Sarcoma Res 2, 24.

Bleul, C. C., Farzan, M., Choe, H., Parolin, C., Clark-Lewis, I., Sodroski, J. and Springer, T. A. (1996). The lymphocyte chemoattractant SDF-1 is a ligand for LESTR/fusin and blocks HIV-1 entry. Nature 382, 829-33.

Brasme, J.-F. F., Chalumeau, M., Oberlin, O., Valteau-Couanet, D. and Gaspar, N. (2014). Time to diagnosis of Ewing tumors in children and adolescents is not associated with metastasis or survival: a prospective multicenter study of 436 patients. J. Clin. Oncol. 32, 1935-40.

Broder, C. C. and Dimitrov, D. S. (1996). HIV and the 7-transmembrane domain receptors. Pathobiology 64, 171-9.

Busillo, J. and Benovic, J. (2006). Regulation of CXCR4 signaling. Biochimica et Biophysica Acta (BBA) - Biomembranes.

Cavazzana, A. O., Miser, J. S., Jefferson, J. and Triche, T. J. (1987). Experimental evidence for a neural origin of Ewing's sarcoma of bone.

Am. J. Pathol. 127, 507-8.

Chaturvedi, A., Hoffman, L. M., Welm, A. L., Lessnick, S. L. and Beckerle, M. C. (2012). The EWS/FLI Oncogene Drives Changes in Cellular Morphology, Adhesion, and Migration in Ewing Sarcoma. Genes Cancer 3, 102-16.

Chaturvedi, A., Hoffman, L. M., Jensen, C. C., Lin, Y.-C. C., Grossmann, A. H., Randall, R. L., Lessnick, S. L., Welm, A. L. and Beckerle, M. C. (2014). Molecular dissection of the mechanism by which EWS/FLI expression compromises actin cytoskeletal integrity and cell adhesion in Ewing sarcoma. Mol. Biol. Cell 25, 2695-709.

Choudhury, K. B., Sharma, S., Kothari, R. and Majumder, A. (2011). Primary extraosseous intracranial Ewing's sarcoma: Case report and literature review. Indian J Med Paediatr Oncol 32, 118-21.

Cohen, J. (1996). Likely HIV cofactor found. Science 272, 809-10.

Costanzi, S., Siegel, J., Tikhonova, I. G. and Jacobson, K. A. (2009). Rhodopsin and the others: a historical perspective on structural studies of G protein-coupled receptors. Curr. Pharm. Des. 15, 3994-4002.

Delattre, O., Zucman, J., Melot, T., Garau, X. S., Zucker, J. M., Lenoir, G. M., Ambros, P. F., Sheer, D., Turc-Carel, C. and Triche, T. J. (1994). The Ewing family of tumors–a subgroup of small-round-cell tumors defined by specific chimeric transcripts. N. Engl. J. Med. 331, 294-9.

Dockhorn-Dworniczak, B., Schafer, K. L., Dantcheva, R., Blasius, S., Winkelmann, W., Strehl, S., Burdach, S., Valen, F. van, Jurgens, H. and Bocker, W. (1994). Diagnostic value of the molecular genetic detection of the t(11;22) translocation in Ewing's tumours. Virchows Arch. 425, 107-12.

Ewing, J. (1922). Neoplastic diseases. A treatise on tumors. Second edition.

Ewing, J. (1972). Classics in oncology. Diffuse endothelioma of bone. James Ewing. Proceedings of the New York Pathological Society, 1921. CA Cancer J Clin 22, 95-8.

Feng, Y., Broder, C. C., Kennedy, P. E. and Berger, E. A. (1996). HIV-1 entry cofactor: functional cDNA cloning of a seven-transmembrane, G protein-coupled receptor. Science 272, 872-7.

Fraccaro, M., Lindsten, J., Ford, C. E. and Iselius, L. (1980). The 11q;22q translocation: a European collaborative analysis of 43 cases. Hum. Genet. 56, 21-51.

Furusato, B., Mohamed, A., Uhlen, M. and Rhim, J. (2010). CXCR4 and cancer. Pathology International.

Giard, D. J., Aaronson, S. A., Todaro, G. J., Arnstein, P., Kersey, J. H., Dosik, H. and Parks, W. P. (1973). In vitro cultivation of human tumors: establishment of cell lines derived from a series of solid tumors. J. Natl. Cancer Inst. 51, 1417-23.

Gill, B. J. and West, J. L. (2014). Modeling the tumor extracellular matrix: Tissue engineering tools repurposed towards new frontiers in cancer biology. J Biomech 47, 1969-78.

Hatori, M., Doi, H., Watanabe, M., Sasano, H., Hosaka, M., Kotajima, S., Urano, F., Hata, J. and Kokubun, S. (2006). Establishment and characterization of a clonal human extraskeletal Ewing's sarcoma cell line, EES1. Tohoku J. Exp. Med. 210, 221-30.

Hayashi, K. and Iwata, M. (2015). Stiffness of cancer cells measured with an AFM indentation method. J Mech Behav Biomed Mater 49, 105-11.

Hoffmann, C., Zurn, A., Bunemann, M. and Lohse, M. J. (2008). Conformational changes in G-protein-coupled receptors-the quest for functionally selective conformations is open. Br. J. Pharmacol. 153 Suppl 1, S358-66.

Huvos, A. G. (1998). James Ewing: cancer man. Ann Diagn Pathol 2, 146-8.

Iselius, L., Lindsten, J., Aurias, A., Fraccaro, M., Bastard, C., Bottelli, A. M., Bui, T. H., Caufin, D., DalprÃ , L. and Delendi, N. (1983). The 11q;22q translocation: a collaborative study of 20 new cases and analysis of 110 families. Hum. Genet. 64, 343-55.

Iwamoto, Y. (2007). Diagnosis and treatment of Ewing's sarcoma. Jpn. J. Clin. Oncol. 37, 79-89.

Janmey, P. A., Wells, R. G., Assoian, R. K. and McCulloch, C. A. (2013). From tissue mechanics to transcription factors. Differentiation 86, 112-20.

Jansen, K. A., Donato, D. M., Balcioglu, H. E., Schmidt, T., Danen, E. H. and Koenderink, G. H. (2015). A guide to mechanobiology: Where biology and physics meet. Biochim. Biophys. Acta.

Jin, Z., Zhao, C., Han, X. and Han, Y. (2012). Wnt5a promotes ewing sarcoma cell migration through upregulating CXCR4 expression. BMC Cancer 12, 480.

Karosas (2010). Ewing's sarcoma. American Journal of Health-

System Pharmacy.

Katira, P., Bonnecaze, R. T. and Zaman, M. H. (2013). Modeling the mechanics of cancer: effect of changes in cellular and extra-cellular mechanical properties. Front Oncol 3, 145.

Kim, R., Li, B. and Chu, Q. (2010). The Role of Chemokine Receptor CXCR4 in the Biologic Behavior of Human Soft Tissue Sarcoma. Sarcoma.

Kodama, K., Doi, O., Higashiyama, M., Mori, Y., Horai, T., Tateishi, R., Aoki, Y. and Misawa, S. (1991). Establishment and characterization of a new Ewing's sarcoma cell line. Cancer Genet. Cytogenet. 57, 19-30.

Kovar, H. (2005). Context matters: the hen or egg problem in Ewing's sarcoma. Semin. Cancer Biol. 15, 189-96.

Kovar, H. (2014). Blocking the road, stopping the engine or killing the driver? Advances in targeting EWS/FLI-1 fusion in Ewing sarcoma as novel therapy. Expert Opin. Ther. Targets 18, 1315-28.

Krook, M. A., Nicholls, L. A., Scannell, C. A., Chugh, R., Thomas, D. G. and Lawlor, E. R. (2014). Stress-induced CXCR4 promotes migration and invasion of ewing sarcoma. Mol. Cancer Res. 12, 953-64.

Kryczek, I., Wei, S., Keller, E., Liu, R. and Zou, W. (2007). Stroma-derived factor (SDF-1/CXCL12) and human tumor pathogenesis. AJP: Cell Physiology.

Lamhamedi-Cherradi, S.-E. E., Santoro, M., Ramammoorthy, V., Menegaz, B. A., Bartholomeusz, G., Iles, L. R., Amin, H. M., Livingston, J. A., Mikos, A. G. and Ludwig, J. A. (2014). 3D tissue-engineered model of Ewing's sarcoma. Adv. Drug Deliv. Rev. 79-80, 155-71.

Landuzzi, L., Giovanni, C. De, Nicoletti, G., Rossi, I., Ricci, C., Astolfi, A., Scopece, L., Scotlandi, K., Serra, M., Bagnara, G. P., et al. (2000). The metastatic ability of Ewing's sarcoma cells is modulated by stem cell factor and by its receptor c-kit. Am. J. Pathol. 157, 2123-31.

Liebner, D. A. (2015). The indications and efficacy of conventional chemotherapy in primary and recurrent sarcoma. J Surg Oncol 111, 622-31.

Lissat, A., Joerschke, M., Shinde, D. A., Braunschweig, T., Meier, A., Makowska, A., Bortnick, R., Henneke, P., Herget, G., Gorr, T. A., et al. (2015). IL6 secreted by Ewing sarcoma tumor microenvironment confers anti-apoptotic and cell-disseminating paracrine responses in Ewing sarcoma cells. BMC Cancer 15, 552.

Loetscher, M., Geiser, T., O'Reilly, T., Zwahlen, R., Baggiolini, M.

and Moser, B. (1994). Cloning of a human seven-transmembrane domain receptor, LESTR, that is highly expressed in leukocytes. J. Biol. Chem. 269, 232-7.

Ludwig, J. A. (2008). Ewing sarcoma: historical perspectives, current state-of-the-art, and opportunities for targeted therapy in the future. Curr Opin Oncol 20, 412-8.

Martinez-Ramirez, A., Rodriguez-Perales, S., Melendez, B., Martinez-Delgado, B., Urioste, M., Cigudosa, J. C. and Benitez, J. (2003). Characterization of the A673 cell line (Ewing tumor) by molecular cytogenetic techniques. Cancer Genet. Cytogenet. 141, 138-42.

May, W. A., Lessnick, S. L., Braun, B. S., Klemsz, M., Lewis, B. C., Lunsford, L. B., Hromas, R. and Denny, C. T. (1993). The Ewing's sarcoma EWS/FLI-1 fusion gene encodes a more potent transcriptional activator and is a more powerful transforming gene than FLI-1. Mol. Cell. Biol. 13, 7393-8.

Monument, M. J., Grossmann, A. H., Baker, C. C., Randall, R. L., Liu, T. and Albertson, D. J. (2015). Molecular Confirmation of Ewing Sarcoma in an 85-Year-Old Woman. Int. J. Surg. Pathol. 23, 500-4.

Mori, Chang, Andrechek, Matsumura, Baba, Yao, Kim, Gatza, Murphy and Nevins (2009). Anchorage-independent cell growth signature identifies tumors with metastatic potential. Oncogene.

Mouw, J. K., Yui, Y., Damiano, L., Bainer, R. O., Lakins, J. N., Acerbi, I., Ou, G., Wijekoon, A. C., Levental, K. R., Gilbert, P. M., et al. (2014). Tissue mechanics modulate microRNA-dependent PTEN expression to regulate malignant progression. Nat. Med. 20, 360-7.

Muller, A., Homey, B., Soto, H., Ge, N., Catron, D., Buchanan, M. E., McClanahan, T., Murphy, E., Yuan, W., Wagner, S. N., et al. (2001). Involvement of chemokine receptors in breast cancer metastasis. Nature 410, 50-6.

Na, K. Y., Kim, H.-S. S., Jung, W.-W. W., Sung, J.-Y. Y., Kalil, R. K., Kim, Y. W. and Park, Y.-K. K. (2014). CXCL16 and CXCR6 in Ewing sarcoma family tumor. Hum. Pathol. 45, 753-60.

Nedelcu, D., Andreescu, N., Boeriu, E., Stefanescu, R., Arghirescu, S. and Puiu, M. (2014). Retrospective study on osteosarcoma and ewing sarcoma - our experience. Maedica (Buchar) 9, 151-6.

Oberlin, E., Amara, A., Bachelerie, F., Bessia, C., Virelizier, J. L., Arenzana-Seisdedos, F., Schwartz, O., Heard, J. M., Clark-Lewis, I., Legler, D. F., et al. (1996). The CXC chemokine SDF-1 is-the ligand

for LESTR/fusin and prevents infection by T-cell-line-adapted HIV-1. Nature 382, 833-5.

Odri, G., Kim, P.-P. P., Lamoureux, F., Charrier, C., Battaglia, S., Amiaud, J., Heymann, D., Gouin, F. and Redini, F. (2014). Zoledronic acid inhibits pulmonary metastasis dissemination in a preclinical model of Ewing's sarcoma via inhibition of cell migration. BMC Cancer 14, 169.

Pachenari, M., Seyedpour, S. M., Janmaleki, M., Babazadeh Shayan, S., Taranejoo, S. and Hosseinkhani, H. (2014). Mechanical properties of cancer cytoskeleton depend on actin filaments to microtubules content: investigating different grades of colon cancer cell lines. J Biomech 47, 373-9.

Pagani, A., Fischer-Colbrie, R., Eder, U., Pellin, A., Llombart-Bosch, A. and Bussolati, G. (1995). Neural and mesenchymal differentiations in Ewing's sarcoma cell lines. Morphological, immunophenotypic, molecular biological and cytogenetic evidence. Int. J. Cancer 63, 738-43.

Palczewski, K., Kumasaka, T., Hori, T., Behnke, C., Motoshima, H., Fox, B., Trong, I., Teller, D., Okada, T., Stenkamp, R., et al. (2000). Crystal Structure of Rhodopsin: A G Protein-Coupled Receptor. Science.

Palmieri, V., Lucchetti, D., Maiorana, A., Papi, M., Maulucci, G., Calapa, F., Ciasca, G., Giordano, R., Sgambato, A. and Spirito, M. De (2015). Mechanical and structural comparison between primary tumor and lymph node metastasis cells in colorectal cancer. Soft Matter 11, 5719-26.

Paszek, M. J., Zahir, N., Johnson, K. R., Lakins, J. N., Rozenberg, G. I., Gefen, A., Reinhart-King, C. A., Margulies, S. S., Dembo, M., Boettiger, D., et al. (2005). Tensional homeostasis and the malignant phenotype. Cancer Cell 8, 241-54.

Phillips, R. J., Burdick, M. D., Lutz, M., Belperio, J. A., Keane, M. P. and Strieter, R. M. (2003). The stromal derived factor-1/CXCL12-CXC chemokine receptor 4 biological axis in non-small cell lung cancer metastases. Am. J. Respir. Crit. Care Med. 167, 1676-86.

Picard, L., Wilkinson, D. A., McKnight, A., Gray, P. W., Hoxie, J. A., Clapham, P. R. and Weiss, R. A. (1997). Role of the amino-terminal extracellular domain of CXCR-4 in human immunodeficiency virus type 1 entry. Virology 231, 105-11.

Potratz, J., Dirksen, U., Jurgens, H. and Craft, A. (2012). Ewing

sarcoma: clinical state-of-the-art. Pediatr Hematol Oncol 29, 1-11.

Pritchard, J. E. (1927). Ewing's sarcoma: A report of a case. Can Med Assoc J 17, 1164-7.

Rajagopalan, L. and Rajarathnam, K. (2006). Structural basis of chemokine receptor function–a model for binding affinity and ligand selectivity. Biosci. Rep. 26, 325-39.

Raman, D., Baugher, P. J., Thu, Y. M. and Richmond, A. (2007). Role of chemokines in tumor growth. Cancer Lett. 256, 137-65.

Richter, G. H. H., Fasan, A., Hauer, K., Grunewald, T. G., Berns, C., Rossler, S., Naumann, I., Staege, M. S., Fulda, S., Esposito, I., et al. (2013). G-Protein coupled receptor 64 promotes invasiveness and metastasis in Ewing sarcomas through PGF and MMP1. J. Pathol. 230, 70-81.

Roland, J., Murphy, B. J., Ahr, B., Robert-Hebmann, V., Delauzun, V., Nye, K. E., Devaux, C. and Biard-Piechaczyk, M. (2003). Role of the intracellular domains of CXCR4 in SDF-1-mediated signaling. Blood 101, 399-406.

Rosenkilde, M. M., Kledal, T. N., Holst, P. J. and Schwartz, T. W. (2000). Selective elimination of high constitutive activity or chemokine binding in the human herpesvirus 8 encoded seven transmembrane oncogene ORF74. J. Biol. Chem. 275, 26309-15.

Rubin, J. (2008). Chemokine signaling in cancer: one hump or two? Semin. Cancer Biol.

Sainz-Jaspeado, M., Lagares-Tena, L., Lasheras, J., Navid, F., Rodriguez-Galindo, C., Mateo-Lozano, S., Notario, V., Sanjuan, X., Garcia Del Muro, X., Fabra, A., et al. (2010). Caveolin-1 modulates the ability of Ewing's sarcoma to metastasize. Mol. Cancer Res. 8, 1489-500.

Sand, L. G., Szuhai, K. and Hogendoorn, P. C. (2015). Sequencing Overview of Ewing Sarcoma: A Journey across Genomic, Epigenomic and Transcriptomic Landscapes. Int J Mol Sci 16, 16176-215.

Sapudom, J., Rubner, S., Martin, S., Kurth, T., Riedel, S., Mierke, C. T. and Pompe, T. (2015). The phenotype of cancer cell invasion controlled by fibril diameter and pore size of 3D collagen networks. Biomaterials 52, 367-75.

Schlesinger, H. R., Gerson, J. M., Moorhead, P. S., Maguire, H. and Hummeler, K. (1976). Establishment and characterization of human neuroblastoma cell lines. Cancer Res. 36, 3094-100.

Shimkin, M. B. (1974). Letter: History of cancer research: a starter

reading list and guide. Cancer Res. 34, 1519-20.

Strauss, S. J., Ng, T., Mendoza-Naranjo, A., Whelan, J. and Sorensen, P. H. (2010). Understanding micrometastatic disease and Anoikis resistance in ewing family of tumors and osteosarcoma. Oncologist 15, 627-35.

Sun, X., Cheng, G., Hao, M., Zheng, J., Zhou, X., Zhang, J., Taichman, R. S., Pienta, K. J. and Wang, J. (2010). CXCL12 / CXCR4 / CXCR7 chemokine axis and cancer progression. Cancer Metastasis Rev. 29, 709-22.

Taloni, A., Alemi, A. A., Ciusani, E., Sethna, J. P., Zapperi, S. and Porta, C. A. La (2014). Mechanical properties of growing melanocytic nevi and the progression to melanoma. PLoS ONE 9, e94229.

Teicher and Fricker (2010). CXCL12 (SDF-1)/CXCR4 Pathway in Cancer. Clinical Cancer Research.

Triolo, V. A. and Riegel, I. L. (1961). The American Association for Cancer Research, 1907-1940. Historical review. Cancer Res. 21, 137-67.

Triolo, V. A. and Shimkin, M. B. (1969). The American Cancer Society and Cancer Research Origins and Organization: 1913-1943. Cancer Res. 29, 1615-40.

Tung, J. C., Barnes, J. M., Desai, S. R., Sistrunk, C., Conklin, M. W., Schedin, P., Eliceiri, K. W., Keely, P. J., Seewaldt, V. L. and Weaver, V. M. (2015). Tumor mechanics and metabolic dysfunction. Free Radic. Biol. Med. 79, 269-80.

Turc-Carel, C., Aurias, A., Mugneret, F., Lizard, S., Sidaner, I., Volk, C., Thiery, J. P., Olschwang, S., Philip, I. and Berger, M. P. (1988). Chromosomes in Ewing's sarcoma. I. An evaluation of 85 cases of remarkable consistency of t(11;22)(q24;q12). Cancer Genet. Cytogenet. 32, 229-38.

Vandercappellen, J., Damme, J. Van and Struyf, S. (2008). The role of CXC chemokines and their receptors in cancer. Cancer Lett. 267, 226-44.

Venkatakrishnan, A. J., Deupi, X., Lebon, G., Tate, C. G., Schertler, G. F. and Babu, M. M. (2013). Molecular signatures of G-protein-coupled receptors. Nature 494, 185-94.

Wang, J., Wang, J., Sun, Y., Song, W., Nor, J. E., Wang, C. Y. and Taichman, R. S. (2005). Diverse signaling pathways through the SDF-1/CXCR4 chemokine axis in prostate cancer cell lines leads to altered patterns of cytokine secretion and angiogenesis. Cell. Signal. 17, 1578-

92.

Wess, J., Han, S.-J. J., Kim, S.-K. K., Jacobson, K. A. and Li, J. H. (2008). Conformational changes involved in G-protein-coupled-receptor activation. Trends Pharmacol. Sci. 29, 616-25.

Whang-Peng, J., Triche, T. J., Knutsen, T., Miser, J., Kao-Shan, S., Tsai, S. and Israel, M. A. (1986). Cytogenetic characterization of selected small round cell tumors of childhood. Cancer Genet. Cytogenet. 21, 185-208.

Wu, B., Chien, E. Y., Mol, C. D., Fenalti, G., Liu, W., Katritch, V., Abagyan, R., Brooun, A., Wells, P., Bi, F. C., et al. (2010). Structures of the CXCR4 chemokine GPCR with small-molecule and cyclic peptide antagonists. Science 330, 1066-71.

Zucman, J., Delattre, O., Desmaze, C., Plougastel, B., Joubert, I., Melot, T., Peter, M., Jong, P. De, Rouleau, G. and Aurias, A. (1992). Cloning and characterization of the Ewing's sarcoma and peripheral neuroepithelioma t(11;22) translocation breakpoints. Genes Chromosomes Cancer 5, 271-7.

Chapter 2

CXCR4 signaling is controlled by immobilization at the plasma membrane[1]

[1]This chapter is based on: E. Beletkaia, S. F. Fenz, W. Pomp, E. Snaar-Jagalska, P. W. C. Hogendoorn, T. Schmidt, CXCR4 signaling is controlled by immobilization at the plasma membrane (*under review at BBA - Molecular cell research)*

Understanding of the regulation mechanisms of CXCR4 signaling is essential for revealing its role in physiological and pathological processes. Though biochemical pathways following CXCR4 activation by its ligand CXCL12 are well established, knowledge about the receptor dynamics on the plasma membrane remains limited. Here we used Ewing sarcoma-derived cells to unravel the processes that are involved in regulating CXCR4 dynamics on the plasma membrane during receptor signaling. Single-molecule epi-fluorescence microscopy showed that CXCR4 was present in monomeric state on the plasma membrane independent of receptor stimulation. However, upon activation freely diffusing receptors were immobilized in a ligand concentration-dependent manner. CXCR4 immobilization was strongly correlated with the ability for G-protein signaling and was a precursor of subsequent endocytotic events. We found that a balanced regulation of G-protein dependent and independent pathways was required for faithful receptor signal transduction.

2.1 Introduction

Ewing sarcoma is a high-grade aggressive tumor occurring predominantly in bones of young children and adolescent. About a quarter of Ewing sarcoma patients have developed metastasis present at first diagnosis (Kovar, 2014). The characteristic and most common chromosomal translocation fusing a portion of the EWSR1 gene to the FLI gene, t(11;22)(q24;q12), results in the chimeric protein, EWS/FLI. This translocation was shown to change the expression of many different genes (Kovar, 2014). Frequently over-expressed in Ewing sarcoma is the chemokine receptor/ligand CXCR4/CXCL12 axis was suggested to promote tumor progression and cell growth (Berghuis et al. 2012). Additionally, CXCR4 was shown to be associated with Ewing sarcoma metastasis and with a poor prognosis for patients (Kim et al., 2011; Bennani-Baiti et al., 2010). Thus, understanding of the molecular mechanisms of CXCR4 signaling regulation is essential.

The C-X-C chemokine receptor type 4 (CXCR4) belongs to the class of G-protein coupled receptor (GPCRs). CXCR4 selectively binds to the C-X-C chemokine CXCL12. The CXCR4/CXCL12 pathway is biochemically well studied (Teicher and Fricker, 2010). Binding of CXCL12 causes conformational changes of the receptor and promotes activation of the G-protein hetero-trimer. Dissociation of the trimer into G_{α}- and $G_{\beta\gamma}$-subunits leads to initiation of the respective pathways downstream of CXCR4. CXCR4 activates four different G_{α} subunits (Rubin, 2009) with predominant coupling to $G_{\alpha q}$ and $G_{\alpha i}$ (Teicher and Fricker, 2010). Activation of $G_{\alpha q}$ regulates protein kinase C (PKC) signaling that leads to Ca^{2+} release. The $G_{\alpha i}$-pathway involves activation of Akt, Erk1/2 and Cdc42 cascades. Dissociated $G_{\beta\gamma}$ activates phospholipase-C (PLC) and phosphoinositide-3 kinase (PI3K). The ultimate outcome of CXCR4 signaling leads to gene transcription, cell adhesion and cell migration (Busillo and Benovic, 2007; Otsuka and Bebb, 2008; Teicher and Fricker, 2010) and hence can be involved in tumor, e.g. Ewing sarcoma, progression and metastasis.

Frequently GPCR signaling is controlled via receptor dimerization. There is evidence that CXCL12-induced activation of CXCR4 leads to the formation of heterodimers with CCR2 and CXCR7 (Springael et al., 2005; Levoye et al.,2009; Luker et al., 2009; Decaillot et al., 2011). It was shown that CXCR7 can regulate CXCR4-dependent pathways by promoting or inhibiting G-protein activation (Levoye et al.,2009; Decaillot et

al., 2011), or act as a CXCL12 scavenger (Naumann et al., 2010). However, some Ewing sarcoma cells, including cell line A673, do not express CXCR7 nor CCR2 (Bennani-Baiti et al., 2010),thus, heterodimerization of CXCR4 with these receptors is likely unimportant.

Many GPCRs are in a dynamic equilibrium between monomers and homo-dimers on the plasma membrane (Kasai and Kusumi, 2014). BRET experiments imply that a small portion of CXCR4 forms homodimers even in the absence of CXCL12 (Hamatake et al., 2009). Additionally, the CXCR4 crystal structure suggests homodimeric state of CXCR4 (Wu et al., 2010). Some studies report that stimulation with CXCL12 is required for CXCR4 homodimerization (Springael et al., 2005), while others report no dimerization of CXCR4 upon activation (Hamatake et al., 2009).

Alongside with receptor dimerization, internalization of GPCRs is considered a regulatory process. Upon activation CXCR4 promotes β-arrestin recruitment that subsequently leads to receptor internalization. Internalized receptors in turn can be recycled to the plasma membrane or follow the lysosomal path towards breakdown (Busillo and Benovic, 2007). This process is recognized as receptor desensitization. In Ewing sarcoma endocytosis was identified to have a strong impact on receptor signaling (Martins et al., 2011).

Thus, CXCR4 conduct on the plasma membrane is very dynamic and has great impact on the receptor signaling. However, knowledge about CXCR4 dynamics on the plasma membrane is controversial. Hence, we decided to use the high spatial and temporal resolution that is combined in single-molecule microscopy to obtain novel understanding of CXCR4 signaling. In the last decade a number of single-molecule studies were undertaken to study receptor dynamics on the plasma membrane and relate the findings to the signaling outcome (de Keijzer et al., 2008; Ueda et al. 2001; Jacquier et al., 2006; Calebiro et al., 2013; Lill et al., 2005; Ye et al., 2013). Here we investigated the membrane dynamics of CXCR4-eYFP in the Ewing sarcoma derived cell line A673. We observed a correlation between receptor stimulation and mobility. Immobilization of the activated receptor was facilitated via $G_{\alpha i}$ mediated pathway and clathrin-dependent endocytosis. Thus, we found indications that receptor signaling was controlled via a regulatory cross-talk between G-protein dependent and independent pathways.

2.2 Materials and Methods

2.2.1 Cell culture and transfection

A673 cells were maintained in IMDM cell culture medium (Gibco, USA) supplemented with 10% fetal bovine serum (FBS, Gibco, USA) at 37°C and 5% CO_2. To study the CXCR4 receptor, A673 wild type (A673 wt) cells were stably transfected using a retroviral construct encoding for CXCR4-eYFP (kindly provided by Prof. Dr. Nikolaus Heveker, University of Montreal). Viral transfection was performed as follows. 5×10^4 cells/well were seeded in a 24-well plate; the next day, 1 MOI of viral particles and 5 μg/mL polybreen was added for 24 hours, followed by medium refreshment. For experiments A673 cells stably transfected with CXCR4-eYFP (further referred to as A673-CXCR4 cells) were used after three passages.

2.2.2 Sample preparation

For imaging $1x10^5$ of A673-CXCR4 cells were placed in 0.35 mm culture dishes (Ibidi, Germany) in 2 mL of complete IMDM medium (with 10% FBS) and left to attach overnight. Before imaging the medium in the samples was replaced with fresh IMDM without serum to minimize autofluorescence. During imaging the CO_2 level was maintained at 5% and temperature at 37°C using the INUBG2E-ZILCS (TokaiHit, Japan).

2.2.3 Global CXCL12 stimulation assay

Activation of the CXCR4 receptor with its specific ligand, CXCL12 (Gibco, USA) was done as global stimulation before imaging: CXCL12 was added to the medium to a final concentration of 6-200 nM. Single-molecule or confocal imaging was performed within 1 hour after addition of CXCL12.

2.2.4 Calcium assay

The change of the cytoplasmic Ca^{2+} concentration was measured using cell-permeant Fluo4-AM (Invitrogen, USA). Cells were supplemented with 10 μM Fluo4-AM for 30 minutes; prior to imaging the medium in the samples was replaced with fresh IMDM without serum to remove Fluo4-AM from the cells environment. Using time-lapse confocal microscopy

(see below) the Fluo4-AM fluorescence was detected in individual cells with 50 ms laser pulses at 488 nm. Time-lapse imaging of the cells was done with a 100× objective at 5 Hz for 5 minutes. Where indicated, imaging was done with a 10× objective and the fluorescence change was determined for the whole field of view. At a specified time point 100 nM CXCL12 was added and the change in fluorescence intensity inside individual cells was registered.

2.2.5 Actin depolymerization

To induce cytoskeletal actin depolymerization cells were pre-incubated with 500 nM latrunculin B (LatB; Sigma, USA) for 30 minutes, which was sufficient for temporal actin cytoskeleton depletion. Subsequently cells were washed with fresh medium and imaged in serum free IMDM with or without global stimulation. Imaging was performed in a 30 minutes time window after medium change. The actin cytoskeleton was repolymerized within that time (Fig. S1).

2.2.6 Endocytosis inhibition

Endocytosis inhibition was achieved by addition of 25 μM chlorpromazine (CHZ; Sigma, USA), to the cells for 30 min prior to imaging. For imaging the medium was replaced by serum free IMDM and single-molecule or confocal imaging was done in absence or presence of CXCL12.

2.2.7 $G_{\alpha i}$ inhibition

Pertussis toxin (PTX; Sigma, USA) was used to detach $G_{\alpha i}$ from CXCR4. A673-CXCR4 cells were pre-incubated with 200 ng/mL PTX for 5 hours and then single-molecule imaging was done in presence of PTX in the serum free IMDM medium with or without global stimulation.

2.2.8 Single-molecule imaging

For single-molecule imaging we combined wide-field microscopy with high-sensitivity fluorescence microscopy as described in detail earlier (Schmidt et al., 1996). In brief, the sample was mounted onto an inverted microscope (Zeiss, Germany) equipped with a 100× objective

(NA=1.4, Zeiss) and a liquid nitrogen-cooled back-illuminated CCD-camera (Princeton Instruments, USA). A region of interest was set to 40×40 pixels with an apparent pixel size of 202±2 nm. Measurements were done by illumination of the sample with a 514 nm laser beam (Coherent, Germany) for 5 ms at the intensity of 2 kW/cm^2. 1500 images were recorded at 20 Hz. Use of the appropriate filter combination: dichroic: z405/514/647/1064rpc and emission filter: z514/647m (Chroma, USA) permitted the signal detection by the CCD-camera. The x/y positions of individual molecules was determined with a localization precision of $\sigma_{p.a.}$ =35±7 nm (Fig. S2).

Image analysis was done using programs written in MatLab (Mathworks Inc., USA) as described before (Schmidt et al., 1996). Briefly, the signal acquired from individual eYFP molecules was fitted with a 2D-Gaussian and filtered with respect to peak intensity, peak width and detection error thresholds. Subsequently, particle image-correlation spectroscopy analysis, PICS, (Semrau and Schmidt, 2007) was used to calculate the cumulative probability (*cdf*) of squared displacements. The *cdf* revealed that CXCR4 diffusion was not homogeneous and was best described with a model accounting for two or three fractions:

$$cdf_{2fr}(r^2,t) = 1 - \left(\alpha \cdot exp(\frac{-r^2}{MSD_1}) + (1-\alpha) \cdot exp(\frac{-r^2}{MSD_2})\right) \quad (2.1)$$

$$cdf_{3fr}(r^2,t) = 1 - \left(\alpha_1 \cdot exp(\frac{-r^2}{MSD_1}) + \alpha_2 \cdot exp(\frac{-r^2}{MSD_2}) + (1-\alpha_1-\alpha_2) \cdot exp(\frac{-r^2}{MSD_3})\right)$$

where α is the fraction size of the receptors with corresponding characteristic mean square displacement, MSD. The MSD was calculated for different time lags up to 300 ms. Subsequently the MSD was analyzed at different time lags to extract the diffusion coefficient (D):

$$MSD = 4 \cdot D \cdot t_{lag} \quad (2.2)$$

where the offset s_0 is a measure for the localization precision ($s_0 = 4\sigma^2$). For each experimental condition the MSD and α was calculated separately. There was no difference in MSD values between resting and

stimulated cells. Thus the data was re-analyzed jointly, with α as a free parameter. In indicated cases the radius of the confinement, r_{conf}, was calculated as in (Saxton, 1993):

$$MSD(t = \infty) = r_{conf}^2 + s_0 \tag{2.3}$$

2.2.9 Time-lapse microscopy

Time-lapse microscopy was performed using a spinning disk (Yokogawa, Japan) microscope (Zeiss, Germany) equipped with a motorized stage (Maerzhauser, Germany) and a home-built autofocus system facilitating time-lapse imaging at multiple positions. Imaging was done with a 10× or 100× objective (Zeiss, Germany) using brightfield, 488 nm or 514 nm laser illumination at a specified time lag. Image analysis was done using algorithms in MatLab (Mathworks Inc., USA).

2.2.10 Simulation of diffusion on a vesicle

We modeled free diffusion of the receptors with a diffusion coefficient $D_{CXCR4(vesicle)} = 0.2\ \mu m^2/s$ on the surface of a sphere with a diameter $d_{vesicle} = 150$ nm. Molecules on the sphere were initialised at the positions $p_i = (x_i, y_i, z_i)$ representing a random distribution on the sphere surface. At each time-lag ($\Delta t = 10^{-5}s$) each molecule was displaced to a temporary position $p_i^{,} = (x_i^{,} = x_i + \Delta x_i, y_i^{,} = yi + \Delta y_i, z_i^{,} = z_i + \Delta z_i)$. The displacement in each dimension, i.e.$\Delta x_i, \Delta y_i$ and Δz_i, were assigned an arbitrary length randomly selected from a normal distribution with a width of $\sqrt{MSD} = \sqrt{(2Dt)}$. On this scale the surface of the sphere was considered flat and the displacement of the molecule was taken as a projection of $p_i^{,}$ on the sphere surface by transformation into spherical coordinates, while the r-coordinate was set as equal to the radius of the sphere. Subsequently the new (x_i, y_i, z_i) positions of the molecules were determined as a transformation into cartesian coordinates. Thus, the (x_i, y_i, z_i) positions determined after each Δt represent the displacement of a molecule on the sphere surface. Using the (x_i, y_i) coordinates we calculated the mean square displacement of the molecules in a projection to a plane to mimic the image of moving molecules in a microcope image; $MSD_{sphere-2D}$. Our simulations revealed, that at t = 50 ms $MSD_{sphere-2D}$ was reaching a plateau and the value of the plateau was

determined to be:

$$\lim_{(t\to\infty)} MSD_{sphere-2D}(t) = \frac{4}{3} \cdot R^2_{sphere}$$

2.3 Results

2.3.1 CXCR4-eYFP is functional in A673-CXCR4 cells

We used the Ewing sarcoma-derived cell line A673 (Martinez-Ramirez et al., 2003). For fluorescence imaging of CXCR4 we stably transfected A673 wt cells with DNA encoding for CXCR4-eYFP (further referred to as A673-CXCR4 cells). By visual inspection we estimated the transfection efficiency to be ∼50%. The expression level of CXCR4-eYFP was estimated as described in (de Keijzer et al., 2008). Briefly, the cell's membrane surface was approximated as a spheroid with a short axis of 20 μm and long axis of 50 μm yielding a cell surface area of $\sim 1.1 \times 10^3 \mu m^2$. The fluorescence of CXCR4-eYFP at the apical membrane was detected when illuminated at 2 kW/cm^2 of 514 nm laser beam. The measured signal (35×10^3 cnts/pxl) was divided by the signal predicted for individual eYFP molecules under the same conditions, 220 cnts (Harms et al., 2001; van Hemert et al., 2010). This calculation yielded an average expression level of $(4\pm1)\times10^4$ CXCR4-eYFP molecules per cell, which is within the range of endogenous GPCR expression in mammalian cells (Massotte, 2003). Confocal microscopy showed that CXCR4-eYFP was primarily localized at the plasma membrane (Fig. 2.1A). CXCR4-eYFP was uniformly distributed and did not form any macroscopic domains (Fig. 2.1A, left).

To show that the CXCR4-eYFP was functional and that the fluorescent tag (eYFP) did not alter CXCR4 signaling, we performed functionality assays on the A673-CXCR4 cells. First, we measured intracellular calcium release upon receptor stimulation using the Ca^{2+} reporter Fluo4-AM. Cells were pre-incubated with Fluo4-AM, and subsequently the change in fluorescence signal on global stimulation of the receptors with 100 nM CXCL12 was monitored for individual cells. The increase of the fluorescence intensity of Fluo4-AM corresponds to the increase of cytoplasmic Ca^{2+}. Figure 2.1B shows a representative measurement of the change of fluorescence signal. The shown data were normalized to the signal before cell stimulation. Similar to the results reported (Mueller et al., 2013; Busillo et al., 2010; Venkatesan et al., 2003), stimulation with

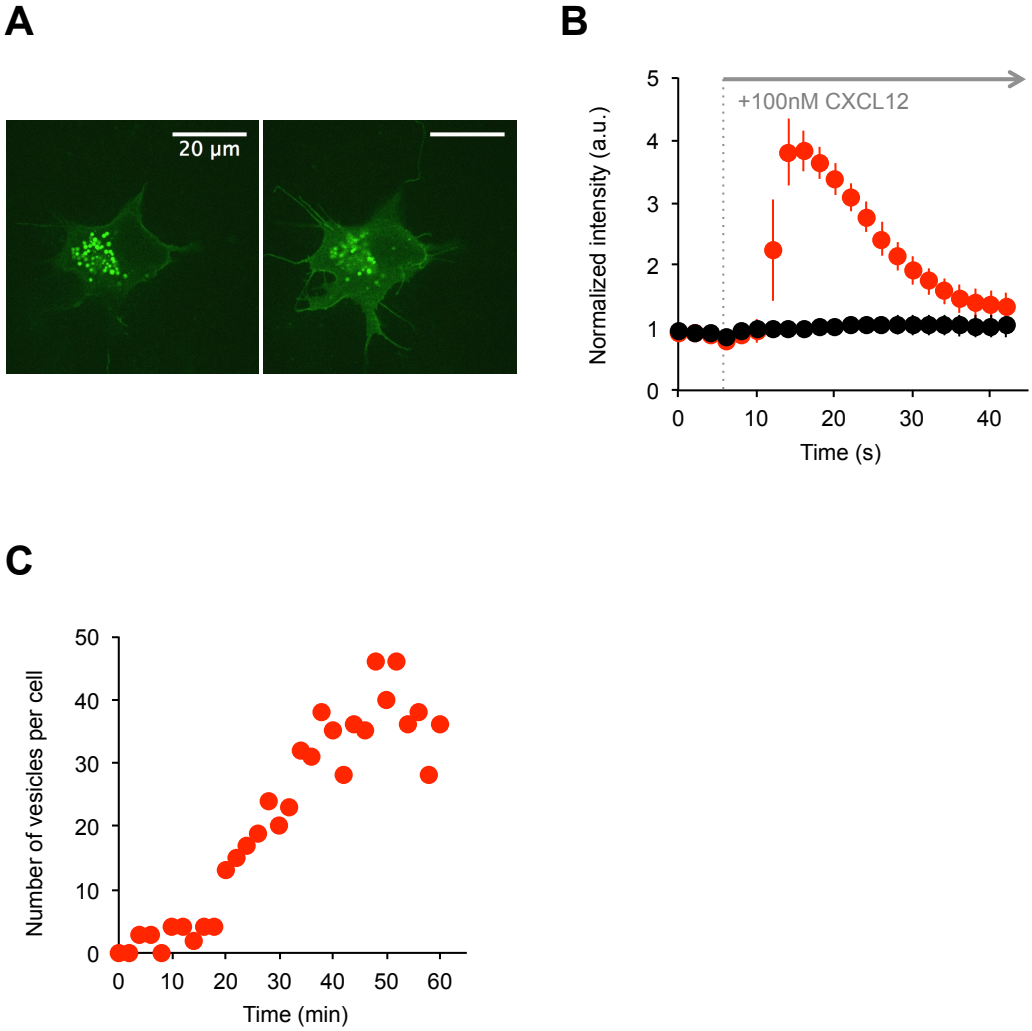

Figure 2.1
Characterization of the A673-CXCR4 cell line. ***A.*** *Confocal images of A673 cells stably transfected with CXCR4-eYFP. The images were acquired by focusing on the basal membrane (left) and in cytoplasmic cross-section of the cell (right).* ***B.*** *Examplary* Ca^{2+} *assay measurement. The curves represent the change in fluorescence intensity of the* Ca^{2+} *indicator - Fluo4-AM - detected in non-transfected cells (black, n=5) or cells transfected with CXCR4-eYFP (red, n=3), after uniform stimulation with 100 nM CXCL12. The error bars represent the standard deviation.* ***C.*** *Appearance of the endocytotic vesicles containing CXCR4-eYFP detected within 60 minutes after cell stimulation with 100 nM CXCL12.*

CXCL12 caused a calcium release, within 20 seconds. Cells expressing CXCR4-eYFP showed a 3.8±0.3 fold intensity increase after receptor stimulation. This result indicates that CXCR4-eYFP were functional and capable of inducing Ca^{2+} release through the respective, $G_{\alpha q}$ pathway.

Another pathway activated shortly after receptor stimulation induces receptor endocytosis. Many GPCRs show internalization via clathrin-dependent endocytosis. Some studies revealed, that upon stimulation CXCR4 internalizes 2 minutes after activation (Venkatesan et al., 2003) and reach a maximum internalization level after ∼30 minutes (Venkatesan et al., 2003; Rey et al., 2007). Therefore, we confirmed that CXCR4-eYFP behaved similarly using 2 minutes time-lapse confocal imaging after CXCL12 addition (Fig. 2.1C). Endocytotic vesicles that contained the fluorescent receptor were manually counted in each frame. Figure 2.1C shows, that after 20 minutes the number of vesicles increased significantly and reached a maximum after 40 minutes. The lack of internalization at an earlier time could be explained (1) by the fact that with confocal imaging only vesicles containing multiple copies of CXCR4-eYFP could be detected; (2) only at a later time the newly formed vesicle detached from the plasma membrane had travelled far enough (∼600 nm) to be distinguishable as entities inside the cell (Serge et al., 2011; Kirchhausen, 2010). This result confirmed that activation with CXCL12 leads to internalization of CXCR4-eYFP, and, hence, the receptor was activating to the β-arrestin pathway.

In summary, we showed that CXCR4-eYFP was properly localized, functional and did not alter the physiological response of the cells. Therefore, we concluded that the A673-CXCR4 cell line was suitable for the study of CXCR4 dynamics and to derive physiological effects.

2.3.2 CXCR4 do not homodimerize upon activation in A673 cells

The biochemical responses of CXCR4 upon stimulation are well established (Teicher and Fricker, 2010). CXCL12 binding to CXCR4 facilitates conformational changes of the receptor leading to the activation of multiple pathways (Teicher and Fricker, 2010). However, knowledge about a possible role of CXCR4 dimerization upon activation is still limited. Earlier reports showed that in 293T cells CXCR4 can be observed in a homodimeric configuration in resting cells and undergos further ho-

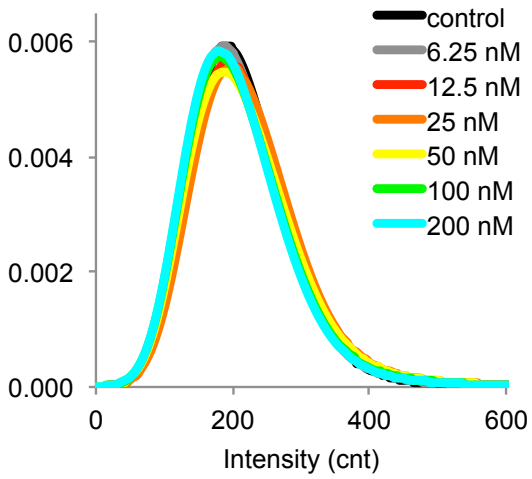

Figure 2.2
Normalized probability density of the intensity of eYFP molecules collected during measurements with or without stimulation. Different colors represent different concentrations of CXCL12.

modimerization upon stimulation with CXCL12 (Springael et al., 2005; Hamatake et al., 2009; Vila-Coro et al., 1999). To test for the presence of homodimers/multimers of CXCR4-eYFP in A673, we analyzed the signal intensity of $>10^5$ YFP signals that were detected on the plasma membrane of transfected cells with and without stimulation by CXCL12 (Fig. 2.2). For individual eYFP molecules at an illumination intensity of 2 kW/cm^2 at 514 nm and an illumination time of 5 ms we expected a signal of ∼220 cnts for individual YPF-molecules (Harms et al., 2001; van Hemert et al., 2010). The appearance of larger signals (>400 cnts) would indicate, that two or more eYFP molecules were detected within the same diffraction limited signal, therefore pointing to receptor dimers or multimers, respectively (Schmidt et al., 1996; Meckel et al., 2011). For resting cells (0 nM) the signal distribution showed only one peak with the maximum at ∼200 cnts (Fig. 2.2, black), corresponding to CXCR4-eYFP monomers. The monomeric distribution did not change upon stimulation with various concentrations of CXCL12 up to 200 nM (Fig 2.2), indicating that CXCR4 stayed monomeric even after activation.

In summary, CXCR4 is a monomeric protein on the plasma membrane of A673 cells independent of its activation state by CXCL12.

2.3.3 Activation of CXCR4 causes immobilization of the receptors

To get deeper insights into the behavior of CXCR4 on the plasma membrane and how it is regulated upon stimulation we applied single-molecule fluorescence microscopy and studied the diffusion dynamics of individual CXCR4-eYFP receptors on the millisecond time-scale at a position accuracy of $\sigma_{p.a.}$=35±7 nm (Fig. S2). A 514 nm laser beam at 2 kW/cm^2 was used in the triggered mode (5 ms illumination) to acquire movies with 1500 frames at a frame-rate of 20 Hz. Each detected fluorescent signal was fit to a 2D-Gaussian (Fig. 2.3A) and filtered with respect to the previously determined eYFP footprint (van Hemert et al., 2010). Subsequently, analysis by particle image correlation spectroscopy, PICS, (Semrau and Schmidt, 2007) was applied to construct the cumulative probability density functions (*cdf*) of square displacement for various time lags. Our results revealed that in resting cells the *cdf* were best described with a model accounting for two fractions, a mobile receptor fraction and an immobile receptor fraction (Fig. S3A, green line). The fraction size (α) and mean square displacements (MSD_1 and MSD_2) were calculated according to eq.(2.1) for various time lags from 50 ms up to 300 ms. The change of MSD_1 and MSD_2 varied with the time lag as shown in Figure 2.3B. MSD_2 did not change over time and was equal to 0.013±0.001 μm^2. It is important to note that the value of MSD_2 was significantly larger than that predicted for an immobile receptor of $4\sigma^2_{p.a.}$= 0.005±0.001 μm^2. This indicates that processes at a shorter time scale (<50 ms), which we could not detect with our imaging settings were responsible for this initial increase. Nonetheless, for brevity, we further refer to the receptor fraction with MSD_2 as immobile.

MSD_1 showed a linear dependence on the time lag as predicted for free diffusion (Fig. 2.3B). Fitting according to eq.(2.3) yielded D_{CXCR4}= 0.18±0.01 μm^2/s. This value is in good agreement with the diffusion coefficient determined, e.g. for the cAMP-receptor in Dictyostelium (0.17±0.02 μm^2/s) (de Keijzer et al., 2008) or other GPCRs in mammalian cells (Calebiro et al., 2013; Lill et al., 2005). The fraction of mobile receptors comprised α=81±3% of the receptors (Fig. 2.3, black)

To study how the activation of CXCR4 influences the behavior of the receptor on the plasma membrane, we applied global stimulation of the cells with CXCL12. CXCL12 was added to the cells right before imaging and single-molecule data were collected within the following hour. Up to

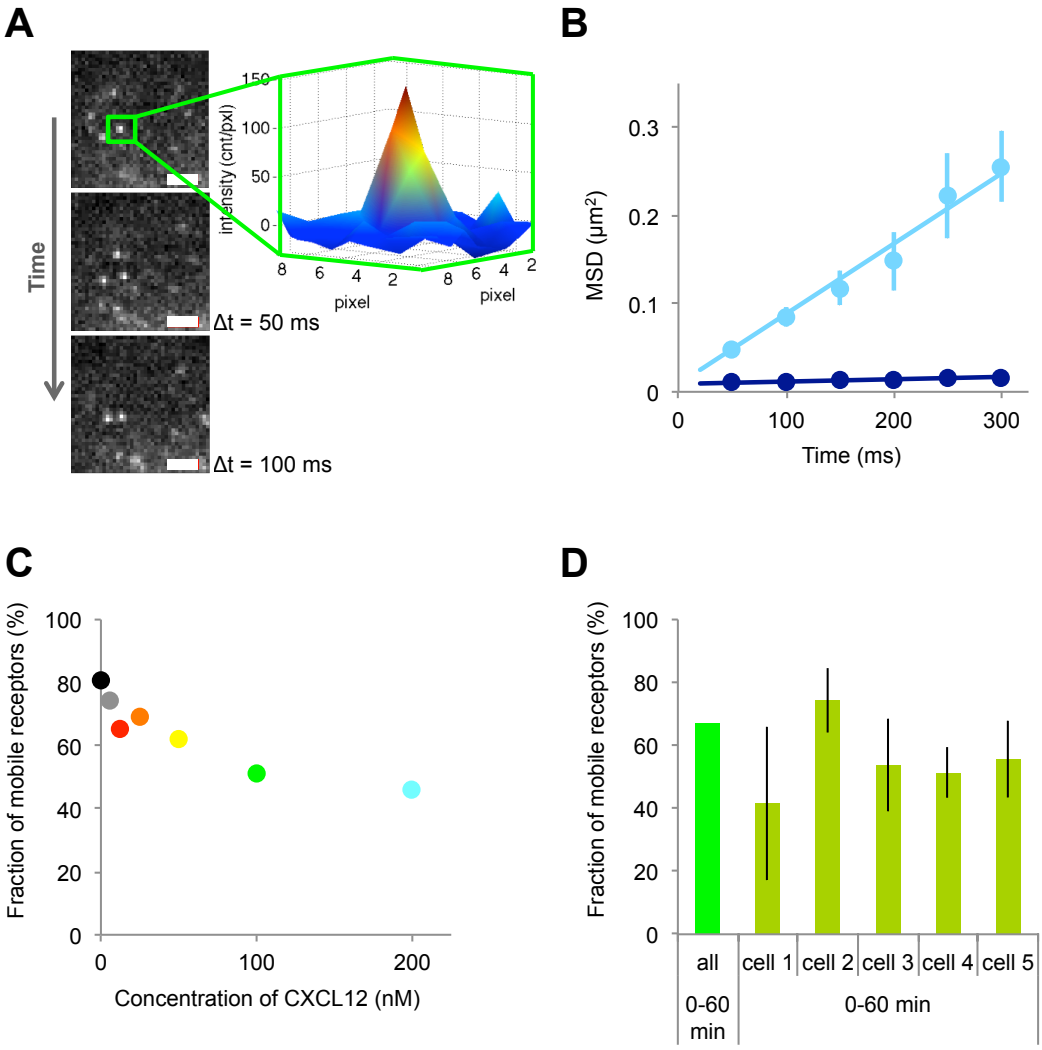

Figure 2.3

Single-molecule characterization of CXCR4 diffusion in resting cells and upon global stimulation with CXCL12. ***A.*** *Single-molecule imaging scheme. Scale-bar: 2 μm.* ***B.*** *Mean square displacement (MSD) vs time plot. MSD of mobile (blue) and immobile (purple) receptors as resulting from a simultaneous fit of the resting and CXCL12 stimulated cells' data sets.* ***C.*** *Dependence of the mobile receptor fraction on the CXCL12 concentration. The color-code correspond to the one used in Figure 2.2.* ***D.*** *The mobile receptor fraction detected at different time points after addition of 100 nM CXCL12 within one experiment. Cell1-cell5 represents five individual cells imaged subsequently within one experiment (0-60 min). 'All' represent the mobile receptor fraction detected by simultaneous analysis of all cells imaged within one experiment.*

five cells were imaged sequentially during one experiment. Each cell was taken as a representative of a 10-15 minutes time window after CXCL12 addition. At least 20 cells were imaged per condition. As shown in Figure 2.3D the mobile receptor fraction size (α) detected for every individual cell during activation exhibited a similar value as for the following cells. The mobile receptor fraction determined from simultaneous analysis of all cells within the experiment (Fig. 2.3D, All) exhibited the same value as that of an individual cells. This result suggests that receptor stimulation had a long-lasting effect on the receptor mobility and did not change over time within 60 min.

Our results showed a strong correlation between receptor stimulation and receptor mobility in a concentration-dependent manner. Addition of increasing concentrations of CXCL12 systematically shifted the cumulative probability distribution of square displacements to lower values (Fig. S1B). The shift in the *cdf* was attributed to a redistribution of the receptor fractions. As shown in Figure 2.3C, the mobile receptor fraction decreased from ∼80% (no CXCL12) to ∼45% (200 nM CXCL12) in a CXCL12 concentrations-dependent manner. This finding was in agreement with earlier findings for other GPCRs (Lill et al., 2005; Jacquier et al., 2006). It is noteworthy that an increase in receptor mobility has been found for cAMP-receptor in Dictyostelium (de Keijzer et al., 2008) and for GABAB in HEK293 cells (Calebiro et al., 2013).

In summary, our results showed that CXCR4 on the plasma membrane is either freely diffusing or immobile. CXCR4 is immobilized upon stimulation with CXCL12 in a concentration-dependent manner.

2.3.4 Actin cytoskeleton is not responsible for CXCR4 immobilization

Many studies agree that GPCR dynamics is actin-cytoskeleton regulated (Andrews et al., 2008; Luo et al., 2006; Tsao et al., 2001; Papadopoulou et al., 2009). Thus, we decided to test whether the actin cytoskeleton underlining the plasma membrane could be involved in modulation of CXCR4 mobility. For this purpose, we induced actin depolymerization by Latrunculin B (LatB). Pre-incubation with LatB for 30 minutes was sufficient to effectively deplete actin (Fig. S1). LatB induces only temporal actin-cytoskeleton depolymerization. Thus, we analyzed the data acquired within the first 30 minutes after medium exchange, while the data collected at 30-60 minutes after which the membrane-skeleton was

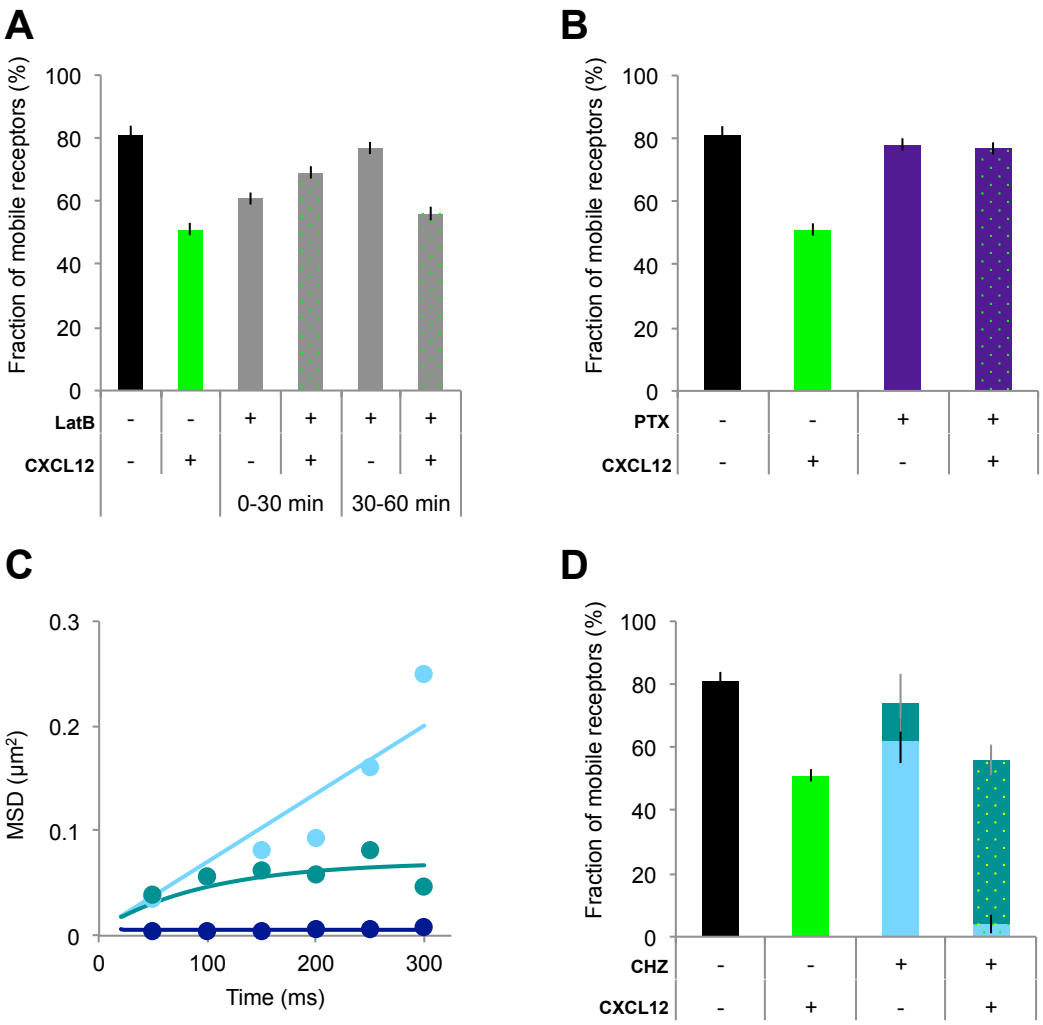

Figure 2.4

Effect of different drug treatments. ***A.*** *The fraction of mobile CXCR4-eYFP in cells pre-treated with LatB (grey) without or with (green punctate pattern) global stimulation by 100 nM CXCL12, compared to the mobile receptor fraction measured in control cells without (black) and with (green) stimulation. LatB provided temporal actin depletion, therefore the acquired data was split accordingly: 0-30 min and 30-60 min.* ***B.*** *Fraction of mobile CXCR4-eYFP measured in PTX pre-treated (purple) cells without and with (green punctate pattern) activation, compared to control cells without (black) and with (green) uniform stimulation with 100 nM CXCL12.* ***C.*** *The MSD vs time plot of the immobile (purple), confined (green) and freely mobile (blue) receptors measured in CHZ pre-treated cells. Solid lines represent the respective fit of the data. The size of the confinement zone was estimated from the linear fit to the plateau and yielded* $r_{conf} = 236 \pm 6$ *nm.* ***D.*** *The mobile receptor fraction in CHZ treated cells presented by two sub-fractions of mobile receptors: freely diffusing (light blue) and confined (dark green). Uniform admission of 100 nM CXCL12 (green punctate pattern) caused a drastic change in the ratio of mobile subpopulations. The total size of the mobile fraction in CHZ pre-treated cells was comparable to the one in the control cells without (black) or with (green) CXCL12 admission.*

re-established served as a control.

To our surprise actin depolymerization did not lead to an increase of the mobile receptor fraction but rather to a decrease to ∼61% (Fig. 2.4A, 0-30 min) in non-stimulated cells. Receptor activation with 100 nM CXCL12 slightly changed the mobile receptor fraction to 69% (Fig. 2.4A, 0-30 min). Data collected after actin repolymerization (30 min after medium exchange) replicated the results acquired for cells with intact actin cytoskeleton (Fig. 2.4A, 30-60 min). In resting cells, the fraction of the mobile receptors reached 77±2% and in the cells stimulated with CXCL12, it dropped to 56±2%.

In summary, our results suggest that in resting cells with intact actin skeleton, the immobile CXCR4 receptors were not anchored to the actin cytoskeleton. Activation by CXCL12 induced an actin-dependent process promoting CXCR4 immobilization. Thus, our result suggests that actin might have an indirect effect on CXCR4 regulation which will be discussed later.

2.3.5 CXCR4 in endocytotic vesicles contribute to the immobile receptor fraction

Upon stimulation many GPCRs proceed to internalization (Tsao et al., 2001; Schwartz et al., 2012; Teicher and Fricker, 2010). Activated GPCRs are known to bind to β-arrestin, which in turn links them to the AP2 adapter complex (Vassilieva and Nusrat, 2008) and facilitates their clathrin-dependent endocytosis. Given that CXCR4 is known to internalize via clathrin-dependent endocytosis upon stimulation and, at the same time, to undergo constitutive internalization without stimulation (Bhandari et al., 2007), we further hypothesized that receptor internalization could possibly explain the drop of the mobile CXCR4 receptor fraction upon stimulation. For the experiments we used chlorpromazine (CHZ), an inhibitor of clathrin-dependent endocytosis. CHZ causes loss of clathrin from the cell surface in the coated pits and, therefore, prevents formation of new clathrin-coated vesicles (CCVs) (Wang et al., 1993; Stuart et al., 2006). Effect of CHZ is very cell-type dependent (Vercauteren et al., 2010). For A673-CXCR4 cells 30 min incubation with 25 μM CHZ was sufficient to inhibit clathrin-dependent endocytosis of CXCR4 effectively, while not causing dramatic cytotoxicity (data not shown).

Single-molecule imaging revealed that CHZ pre-treated cells exhib-

ited the same mobile CXCR4 receptor fraction (α = 74±9%) as control cells (α = 81±3%). However, in the CHZ pre-treated cells the mobile receptor fraction was composed of two sub-fractions, a freely diffusing fraction (62±7%) and a receptor fraction that exhibited confined diffusion (12±9%) as reflected by a sub-linear increase of MSD with timelag (Fig. 2.4C,D). Both sub-fractions of mobile receptors showed similar diffusion coefficients as the fraction of mobile receptors in resting cells, DCXCR4 (CHZ) = 0.16±0.02 $\mu m^2/s$. The size of the confinement zone was estimated from a fit to the plateau in the MSD vs time plot (Fig. 2.4C) according to eq.(2.3) in Materials and Methods and yielded r_{conf} = 236±6 nm.

Given the typical radius of a clathrin-coated vesicle of ∼75-100 nm (McMahon and Boucrot, 2011), which contains a surface area of 0.07-0.13 μm^2 equal to the area covered by the confinement zone in our experiments, we suggest that receptors exhibiting confined diffusion correspond to the receptors trapped in a pre-cursor structure of clathrin-coated pits. Thus, in CHZ pre-treated cells mobile receptors undergoing constitutive internalization accumulate in a precursor structure of clathrin-coated pits and stay locked there since endocytosis cannot proceed.

When CHZ pre-treated cells were stimulated with 100 nM CXCL12, the fraction of mobile receptors decreased (α = 56± 6%) and the distribution of receptors between freely diffusing and confined fractions changed dramatically (Fig. 2.4D). Nearly all receptors showed confined diffusion, while only a small fraction showed free diffusion (52±5% and 4±3%, respectively), suggesting that activated receptors proceed to internalization. This is in good agreement with our internalization experiment (Fig. 2.1C) and with data from other groups (Venkatesan et al., 2003; Rey et al., 2007), showing that upon stimulation the rate of CXCR4 internalization increases.

In summary, CHZ prevents the formation of clathrin-coated vesicles and, hence, receptors proceeding to internalization get trapped in confined areas reminiscent of precursor structures of coated pits. Thus, our results suggest, that the immobile fraction of receptors upon stimulation was caused by CXCR4 trapped in clathrin-coated vesicles, in which the diffusion could not be resolved (see below).

2.3.6 G-proteins control CXCR4 immobilization

Up to date, internalization of GPCR's is considered as a way of receptor desensitization. Our results, suggest that internalizing receptors appear as immobile. However, the ratio of mobile and immobile fractions in stimulated CHZ pre-treated cells resembled such of the control cells. At the same time we find that immobilization of CXCR4 correlated with activation of receptors. Therefore, having established a correlation between receptor mobility and signaling, we were interested in how receptor mobility is affected when the signaling chain is disrupted at the level of G-proteins. Previous reports showed a change in G-protein mobility while the cAR1 receptor was stimulated (van Hemert et al., 2010). Stimulation of CXCR4 mainly results in activation of two isoforms of the G_{α} subunit: $G_{\alpha q}$ and $G_{\alpha i}$ (Teicher and Fricker, 2010). Kleemann et al. showed elevated coupling of $G_{\alpha i}$ to CXCR4 upon receptor stimulation (Kleemann et al., 2008). This coupling of the $G_{\alpha i}$ on the cytosolic side should not per se influence the receptor dynamics. However, hypothesizing that the $G_{\alpha i}$ pathway activation might result in formation of a supramolecular scaffold (Ritter et al., 2009) for further signalling, we probed how the interaction of CXCR4 with the $G_{\alpha i}$ subunit could modulate the mobile receptor fraction.

In our experiments we used pertussis toxin (PTX) as an agent resulting in loss of coupling of $G_{\alpha i}$ and the receptor (Moss et al., 1984; Mangmool and Kurose, 2011). We pre-incubated A673-CXCR4 cells with PTX for 5 hours. During the experiments PXT was also present in the medium. As predicted, in resting cells, single-molecule imaging of CXCR4-eYFP did not show any change in the diffusion coefficient of the receptors. Moreover, the mobile receptor fraction did not change compared to the control without PXT (Fig. 2.4B), suggesting that if $G_{\alpha i}$ was coupled to CXCR4 it had no measurable impact on the receptor dynamics. However, when 100 nM CXCL12 was added to the cells, no significant drop in the mobile receptor fraction was observed (Fig. 2.4B). This behavior was in contrast to the decrease in the mobile receptor fraction detected for CXCR4 receptors upon stimulation in control cells (Fig. 2.4B, green bar). This result supports our earlier conclusion that a bigger fraction of immobile receptors is strongly correlated to receptor signalling.

In summary, our results imply that the decrease in the mobile receptor fraction upon stimulation must be interpreted as an outcome of the

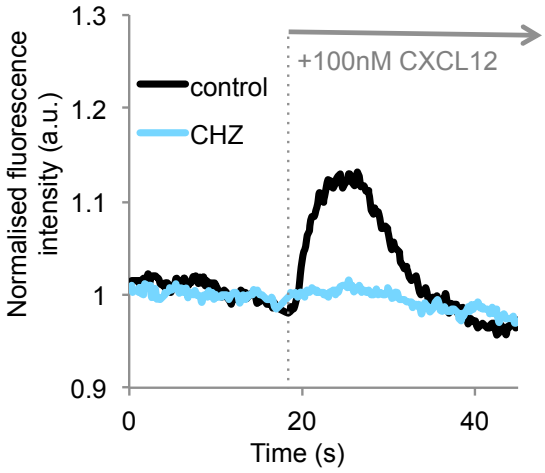

Figure 2.5
Ca^{2+} assay. The curves represent the change in fluorescence intensity of the Ca^{2+} indicator - Fluo4-AM - detected in cells pre-treated with CHZ (light blue) or in control (black) cells after uniform stimulation with 100 nM CXCL12.

of the subsequent $G_{\alpha i}$-pathway activation potentially resulting in formation of a supramolecular scaffold (signalosome, see Fig. 2.6), while blocking the receptor interaction with $G_{\alpha i}$ lead to receptor mobility that did not change upon stimulation.

2.3.7 Cross-talk between G-protein dependent and independent pathways

Our results showed, that immobilization of CXCR4 upon stimulation is facilitated via receptor endocytosis. At the same time the $G_{\alpha i}$-dependent pathway also lead to CXCR4 immobilization. Taken together, these results suggest that G-protein dependent and independent pathways are cross-regulated. Thus, we checked whether a G-protein dependent pathway would be affected by inhibition of CXCR4 endocytosis. We performed a Ca^{2+} assay in the cells under different conditions. Cells with inhibited clathrin-dependent endocytosis (pre-treated with CHZ) showed no Ca^{2+} release upon CXCR4 activation (Fig 2.5). This result implies, that the G-protein independent pathway of receptor internalization was interfering with the early stages of a G_{α}-dependent pathway.

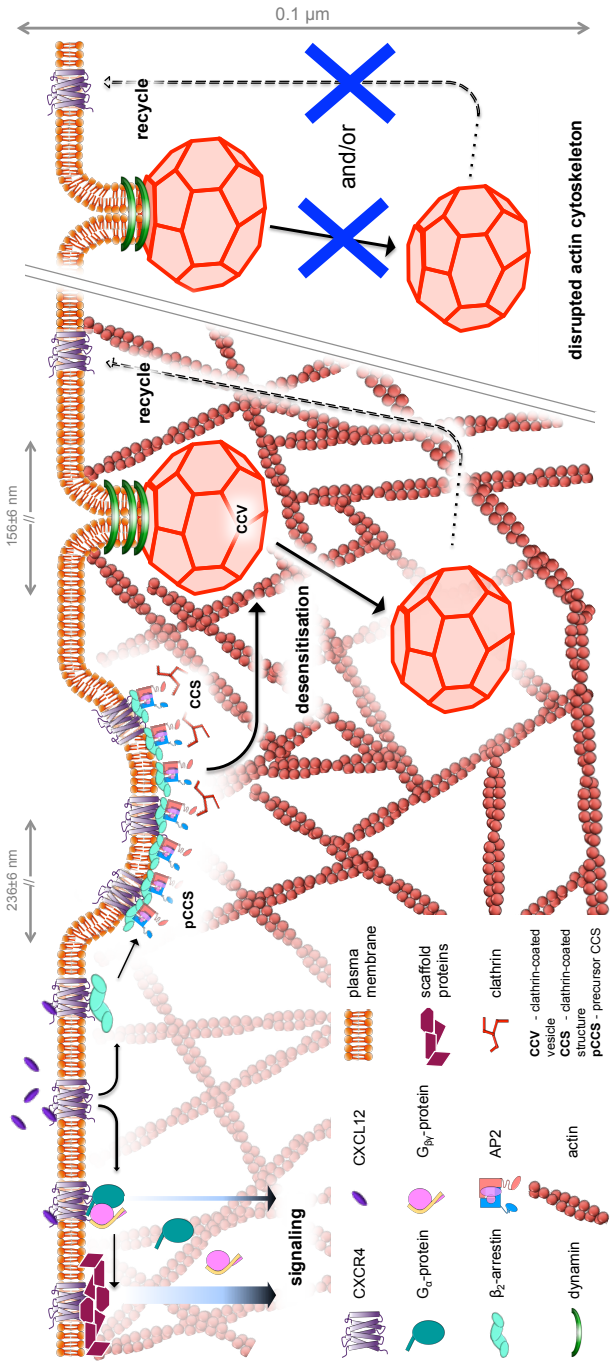

Figure 2.6
Current model. Binding with CXCL12 CXCR4 is activating G-protein dependent (left) and independent (right) pathways. Activation of the biochemical pathways result in CXCR4 immobilization either in super-molecular signalosome, causing enhanced signalling, or in the clathrin-coated vesicles, resulting in receptor internalization, imply a cross-talk between these signalling cascades.

In summary, we suggest that two processes together regulate CXCR4 mobility and thus activation/signalling. Endocytosis driven immobilization leads to desensitization while G-protein driven local signalosome formation might result in signal enhancement (Fig. 2.6). Together, both processes regulate the overall cellular response.

2.4 Discussion

GPCR signalling is a complex process in which only parts have been unraveled. Activation of CXCR4 promotes signalling through G-proteins resulting in expression of certain genes, cells survival/proliferation, chemotaxis, etc. Simultaneously G-protein independent pathways, e.g. β-arrestin, are activated and result in receptor desensitization (Teicher and Fricker, 2010). All the biochemical pathways are studied in detail, but the role of the receptor dynamics on the plasma membrane remains poorly understood.

To elucidate the molecular mechanism of CXCR4 signal transduction, we studied CXCR4 during activation using the receptor mobility as a marker. Our results revealed that already in the resting cells receptor diffusion was not homogeneous. We detected two receptor species, one mobile and one immobile. Activation of CXCR4 with CXCL12 caused a concentration-dependent decrease of the mobile receptor fraction, indicating a correlation between receptor signalling and diffusion on the plasma membrane. Our data gives information on receptor diffusion at millisecond time scales, while, most biochemical or other receptor-signalling processes require longer time, e.g. endocytosis of a receptor takes $\sim$1 minute (Cocucci et al., 2012; Boulant et al., 2011). In this respect, our results depict a snapshot. However, we did not observe a time dependent change in the mobile receptor fraction (Fig. 2.3D), meaning that there was a constitute fraction of immobile receptors.

Many studies of GPCRs agree that receptors dynamics/signalling strongly depends on the actin cytoskeleton. Actin remodelling was reported to have a key role in the pro-apoptotic responses upon mAR activation (Papadopoulou et al., 2009). Luo et al. showed that a big portion of CXCR4 is pre-coupled with the cortical actin binding protein - cortactin (Luo et al., 2006). Stimulation with CXCL12 induced further translocation of cortactin from endosomal compartments and colocalization with CXCR4. However, our results did not show actin-dependent

changes in the diffusion coefficient of CXCR4, and actin depletion did not cause the predicted increase in receptor mobility. In contrast, in the actin depleted cells the fraction of mobile receptors was decreased compared to control. These results imply that there is no direct physical interaction between receptors and actin. However, the change in the CXCR4 mobile fraction indicated, that there was actin-dependent regulation of receptor mobility.

Actin is known to play an important role in sorting of GPCRs to diverse membrane pathways after endocytosis (Tsao et al., 2001; Samaj et al., 2004). For instance, linking of the β2-adrenoreceptor to actin inhibits trafficking of endocytosed receptors to lysosomes and promotes their recycling to the plasma membrane (Tsao et al., 2001). Therefore, during actin cytoskeleton depletion one could expect that most of the receptors, which are endocytosed, follow the lysosomal route instead of being recycled to the plasma membrane (Fig. 2.6, right side). Such a process could lead to a change in the balance of different fractions of receptors present on the plasma membrane. Moreover, there are indications that actin is involved in all forms of endocytosis (Samaj et al., 2004). Though, actin was reported to function as a late component of clathrin-dependent endocytosis (McMahon and Boucrot, 2011) it is responsible for a range of processes (Kichhausen, 2009). EM imaging and life-cell imaging showed that depletion of the actin cytoskeleton caused an increased fraction of shallow and curved clathrin-coated structures on the plasma membrane in comparison to invaginated structures and formed vesicles (Yarar et al., 2005; Boulant et al., 2011). Furthermore, it was shown that actin polymerization at the plasma membrane controls both the alignment and mobility of clathrin-coated vesicles, facilitates the internalization step, and drives rapid transport of early endosomes away from the plasma membrane in the cytosol (Samaj et al., 2004). Hence, actin depletion can be considered as one form of indirect clathrin-dependent endocytosis inhibition at a later stage. Accordingly, in actin-depleted resting cells, CXCR4 undergoing constitutive internalization stall in vesicles, which cannot be removed from the plasma membrane (Fig.2.6, right side). These receptors contribute to the observed immobile fraction (see below). During receptor activation, disturbed vesicle formation and/or vesicle scission could result in CXCR4 failing to proceed with endocytosis and to show the accompanying decrease in the mobile receptor fraction.

In our experiments we used CHZ to directly address the question of

how endocytosis interferes with the mobility of CXCR4 on plasma membrane. CHZ causes loss of clathrin from the cell surface in the coated pits and, therefore, prevents formation of new clathrin-coated vesicles (CCVs) (Wang et al., 1993; Stuart et al., 2006). However, loss of clathrin from the cell surface would not affect the early stages of clathrin-coated structure (CCS) formation. Clathrin-coated vesicle formation consists of five steps: (1) nucleation, (2) cargo selection, (3) coat assembly, (4) scission and (5) uncoating (McMahon and Boucrot, 2011). The first two steps are promoted by a number of initiation proteins, e.g. FCHO 1,2, Epsin and adaptor proteins, e.g. β-arrestin. These proteins result in initiation of the membrane curvature and receptor recruitment (Fig.2.6 middle). Further, the AP2 adaptor protein and clathrin are recruited during clathrin-coated pit maturation and coat assembly. Thus, a membrane invagination appears and progresses before recruitment of clathrin (McMahon and Boucrot, 2011). Therefore, CHZ pre-treated cells could still form precursor structures of clathrin-coated pits (pCCS), while further internalization was blocked. This mechanisms of the endocytosis inhibition is favorable when addressing the endocytosis-mediated regulation of the receptor dynamics on the plasma membrane. Our data showed, that inhibition of a clathrin-dependent endocytosis with CHZ caused appearance of a receptor fraction undergoing confined diffusion. During CXCR4 activation in CHZ pre-treated cells all mobile receptors were diffusing in a confinement zone. The radius of the confinement zone (236±6 nm) suggested that the confinement corresponded to precursor CCS (pCCS). Upon stimulation CXCR4 was driven to CCVs, but due to the CHZ pre-treatment, the receptors were confined to pCCS.

Thus, in untreated cells CXCR4 would be trapped in CCVs after stimulation. As the typical size of a CCV equals 100-200 nm which is within the axial resolution of our microscope (∼1 μm) (Fig.2.6), diffusion of the receptors on the vesicle surface will be detected as a 2D projection . To elucidate the effect hereof, we modeled free diffusion of the receptor on a vesicle with a diffusion coefficient $D_{CXCR4(vesicle)}$=0.2 $\mu m^2/s$ on the surface of a vesicle with a diameter $d_{vesicle}$= 150 nm and subsequently analyzed the 2D-projection of the data. Our simulations revealed, that the $MSD_{sphere-2D}$ linearly increased with timelag and reached a plateau at a time lag of t = 50 ms (Fig. S4), which corresponds to the time lag of our single-molecule measurements. The simulations further revealed that the plateau value is given by $MSD_{(sphere-2D)}(t = \infty) = \frac{4}{3}R^2$,

where R is the vesicle radius. Further, taking into account the positional accuracy of $\sigma_{p.a.}$ = 35±7 nm, and the value we found for MSD_2, σ_{MSD2} = 57±2 nm, the vesicle radius is then given by $\frac{4}{3}R^2_{MSD2} = 4\sigma^2_{MSD2} - 4\sigma^2_{(p.a.)}$. Using our experimental findings we calculated a value R_{MSD2} = 78±3 nm which was very similar to the size of a clathrin-coated vesicle. Together these findings showed that the immobile receptors we found can be attributed to receptors diffusing in a CCV. Thus, CXCR4 undergoing constitutive internalization (Bhandari et al., 2007) would contribute to the immobile receptor fraction in resting cells and the increase of the immobile fraction during activation would be related to an elevated level of clathrin-dependent endocytosis of CXCR4. Hence, clathrin-dependent endocytosis is involved in regulation of CXCR4 mobility on the plasma membrane.

Stimulation experiments showed a concentration-dependent decrease of the mobile receptor fraction, indicating that receptor immobilization was correlated with CXCR4 activation. This was further confirmed by experiments in cells treated with PTX. Detachment of $G_{\alpha i}$ from CXCR4 altered the ratio of mobile to immobile receptors in response to CXCL12 stimulation, compared to non-treated cells. There was no decrease in the mobile receptor fraction, supporting our hypothesis of correlated CXCR4 mobility on the plasma membrane and signalling. As clathrin-dependent endocytosis is G-protein independent and the majority of biochemical signalling of CXCR4 is mediated through activation of the $G_{\alpha i}$-subunit, PTX is a tool to separate G-protein dependent and independent pathways. In contrast to neuroblastoma cells, where $G_{\alpha i}$ detachment with PTX failed to inhibit internalization of CXCR4 upon CXCL12 addition (Clift et al., 2014), our experiments suggest that in Ewing sarcoma cells, disrupted receptor signalling prevented receptor internalization. This idea is supported by the number of reports claiming an important role of caveolin (main component of caveolin-dependent endocytosis; Pelkmans and Helenius, 2002) in signalling of various molecules in Ewing sarcoma (Martins et al., 2011; Sainz-Jaspeado et al., 2010; Tirado et al., 2006; Sainz-Jaspeado et al., 2013). For instance, it was shown that in Ewing sarcoma cells blockade of IGF1R endocytosis inhibits the receptor's signalling (Martins et al., 2011). Furthermore, in our experiments, CHZ pre-treatment disturbed $G_{\alpha q}$-dependent Ca^{2+} release upon CXCL12 stimulation.

In conclusion, here we showed that in Ewing sarcoma derived A673

cells the CXCR4 receptor mobility on the plasma membrane is strongly correlated with receptor signalling. Activated receptors are immobilized in a concentration-dependent manner. Immobilization of the receptor is facilitated via clathrin-dependent endocytosis structures, e.g. vesicles, or via $G_{\alpha i}$ - initiated supramolecular scaffolding. Inasmuch as these processes lead to opposite results (desensitization or signal enhancement in signalosomes, respectively) balanced regulation of G-protein dependent and independent pathways is required for proper receptor signal transduction.

2.5 Supplemental figures

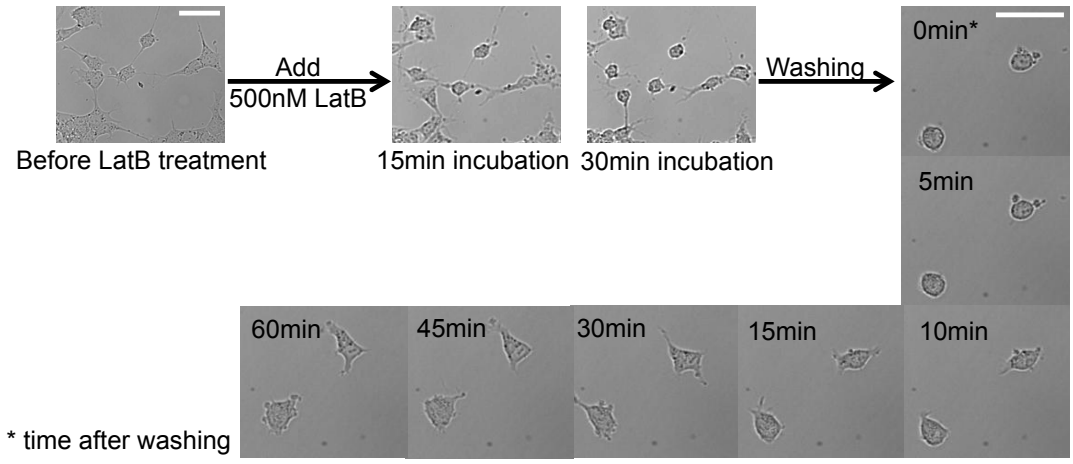

Figure S1
LatB treatment. Cells pre-treated with 500 nM LatB for 30 min loose their shape and show round morphology. After media change actin stays depleted for up to 30 min, subsequently actin was repolymerized. Scale bar: 50 μm.

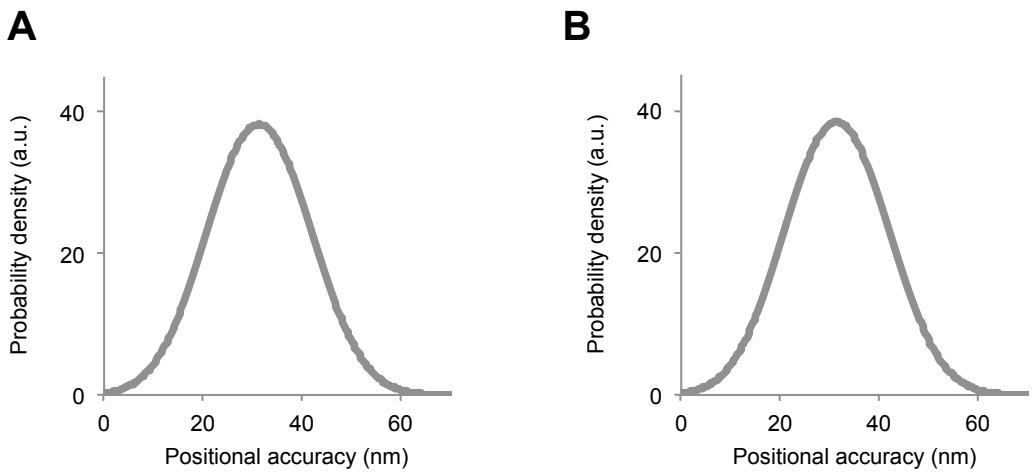

Figure S2
*Positional accuracy of single molecules in x (**A**) and y (**B**). The data was collected for over 10^5 molecules and thresholded with respect to the signal width and intensity.*

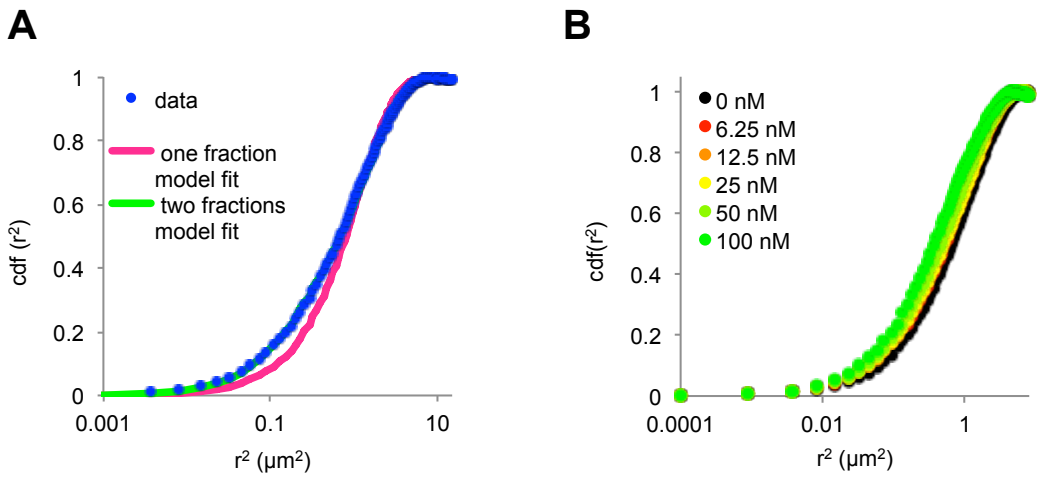

Figure S3

A. *Cumulative distribution of square displacements in resting (control) cells. Data points (blue dots) were best fit with a two fraction model (green curve), while a one fraction model (pink curve) failed.* ***B.*** *Cumulative distribution of square displacements of CXCR4-eYFP constructed for the cells with uniform admission of different concentrations of CXCL12 - from ∼6 nM (red) to 100 nM (green) - are shifted compared to the cdf without stimulation (black).*

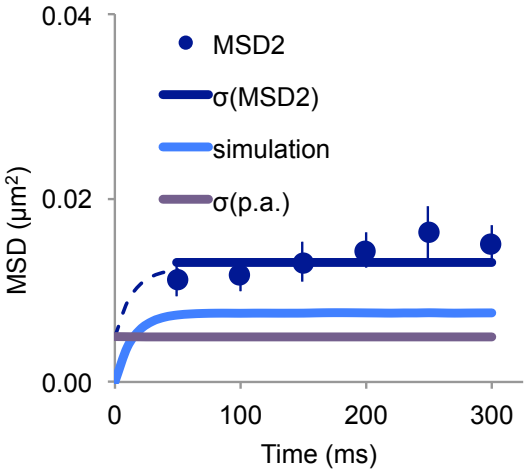

Figure S4

Simulation of the free diffusion on the vesicle compared to MSD_2 data and positional accuracy. Dashed line is a result of summation of simulation and positional accuracy for 50 ms.

2.6 Acknowlegement

We thank S. Coppola for help with the data analysis, Karoly Szuhai and Laurens Sand for the valuable comments on data interpretation.

2.7 References

Andrews, N. L., Lidke, K. A., Pfeiffer, J. R., Burns, A. R., Wilson, B. S., Oliver, J. M. and Lidke, D. S. (2008). Actin restricts FcepsilonRI diffusion and facilitates antigen-induced receptor immobilization. Nat Cell Biol. 10, 955-963.

Bennani-Baiti, I. M., Cooper, A., Lawlor, E. R., Kauer, M., Ban, J., Aryee, D.N. and Kovar, H. (2010). Intercohort gene expression co-analysis reveals chemokine receptors as prognostic indicators in Ewing's sarcoma. Clin Cancer Res. 16, 3769-3778.

Berghuis, D., Schilham, M. W., Santos, S. J., Savola, S., Knowles, H. J., Dirksen, U., Schaefer, K. L., Vakkila, J., Hogendoorn, P. C. and Lankester, A. C. (2012). The CXCR4-CXCL12 axis in Ewing sarcoma: promotion of tumor growth rather than metastatic disease. Clin Sarcoma Res. 2, 24.

Bhandari, D., Trejo, J., Benovic, J. L. and Marchese, A. (2007). Arrestin-2 interacts with the ubiquitin-protein isopeptide ligase atrophin-interacting protein 4 and mediates endosomal sorting of the chemokine receptor CXCR4. J Biol Chem. 282, 36971-36979.

Boulant, S., Kural, C., Zeeh, J. C., Ubelmann, F. and Kirchhausen, T. (2011). Actin dynamics counteract membrane tension during clathrin-mediated endocytosis. Nat Cell Biol. 13, 1124-1131.

Busillo, J. M. and Benovic, J. L. (2007). Regulation of CXCR4 signaling. Biochim Biophys Acta. 1768, 952-963.

Calebiro D., Rieken, F., Wagner, J., Sungkaworn, T., Zabel, U., Borzi, A., Cocucci, E., Zurn, A. and Lohse, M. J. (2013). Single-molecule analysis of fluorescently labeled G-protein-coupled receptors reveals complexes with distinct dynamics and organization. Proc Natl Acad Sci U S A. 110, 743-748.

Clift, I. C., Bamidele, A.O., Rodriguez-Ramirez, C., Kremer, K. N. and Hedin, K. E. (2014). β-Arrestin1 and distinct CXCR4 structures are required for stromal derived factor-1 to downregulate CXCR4 cell-surface levels in neuroblastoma. Mol Pharmacol. 85, 542-552.

Cocucci, E., Aguet, F., Boulant, S. and Kirchhausen, T. (2012). The first five seconds in the life of a clathrin-coated pit. Cell. 150, 495-507.

de Keijzer, S., Serge, A., van Hemert, F., Lommerse, P. H., Lamers, G. E., Spaink, H. P., Schmidt, T. and Snaar-Jagalska, B. E.. (2008). A spatially restricted increase in receptor mobility is involved in directional sensing during Dictyostelium discoideum chemotaxis. J Cell Sci. 121,

1750-1757.

Decaillot, F. M., Kazmi, M. A., Lin, Y., Ray-Saha, S., Sakmar, T. P. and Sachdev, P. (2011). CXCR7/CXCR4 heterodimer constitutively recruits beta-arrestin to enhance cell migration. J Biol Chem. 286, 32188-32197.

Hamatake, M., Aoki, T., Futahashi, Y., Urano, E., Yamamoto, N. and Komano, J. (2009). Ligand-independent higher-order multimerization of CXCR4, a G-protein-coupled chemokine receptor involved in targeted metastasis. Cancer Sci. 100, 95-102.

Harms, G. S., Cognet, L., Lommerse, P. H. M., Blab, G. A., Kahr, H., Gamsjager, R., Spaink, H. P., Soldatov, N. M., Romanin, C. and Schmidt, T. (2001). Single-Molecule Imaging of L-Type Ca2+ Channels in Live Cells. Biophysical J. 81, 2639-2646.

Harms, G. S., Cognet, L., Lommerse, P. H. M., Blab, G.A. and Schmidt, T. (2001). Autofluorescent Proteins in Single-Molecule Research: Applications to Live Cell Imaging Microscopy. Biophysical J. 80, 2396-2408

Jacquier, V., Prummer, M., Segura, J.-M., Pick, H. and Vogel, H. (2006). Visualizing odorant receptor trafficking in living cells down to the single-molecule level. Proc Natl Acad Sci U S A. 103, 14325-12330.

Kasai, R. S. and Kusumi, A. (2014). Single-molecule imaging revealed dynamic GPCR dimerization. Curr Opin Cell Biol. 27, 78-86.

Kim, R. H., Li, B.D. and Chu, Q.D. (2011). The role of chemokine receptor CXCR4 in the biologic behavior of human soft tissue sarcoma. Sarcoma. 2011, 593708.

Kirchhausen, T. (2009). Imaging endocytic clathrin structures in living cells. Trends Cell Biol. 19, 596-605.

Kleemann, P., Papa, D., Vigil-Cruz, S. and Seifert, R. (2008). Functional reconstitution of the human chemokine receptor CXCR4 with G(i)/G (o)-proteins in Sf9 insect cells. Naunyn Schmiedebergs Arch Pharmacol. 378, 261-274.

Kovar, H. (2014). Blocking the road, stopping the engine or killing the driver? Advances in targeting EWS/FLI-1 fusion in Ewing sarcoma as novel therapy. Expert Opin Ther Targets. 18, 1315-1328.

Levoye, A., Balabanian, K., Baleux, F., Bachelerie, F. and Lagane, B. (2009). CXCR7 heterodimerizes with CXCR4 and regulates CXCL12-mediated G protein signaling. Blood. 113, 6085-6093.

Lill, Y., Martinez, K. L., Lill, M. A., Meyer, B. H., Vogel, H. and

Hecht, B. (2005). Kinetics of the initial steps of G protein-coupled receptor-mediated cellular signaling revealed by single-molecule imaging. Chemphyschem. 6, 1633-1640.

Luker, K. E., Gupta, M. and Luker, G. D. (2009). Imaging chemokine receptor dimerization with firefly luciferase complementation. FASEB J. 23, 823-834.

Luo, C., Pan, H., Mines, M., Watson, K., Zhang, J. and Fan, G. H. (2006). CXCL12 induces tyrosine phosphorylation of cortactin, which plays a role in CXC chemokine receptor 4-mediated extracellular signal-regulated kinase activation and chemotaxis. J Biol Chem. 281, 30081-30093.

Mangmool, S. and Kurose, H. (2011). G(i/o) protein-dependent and -independent actions of Pertussis Toxin (PTX). Toxins (Basel). 3, 884-899.

Martinez-Ramirez, A., Rodriguez-Perales, S., Melendez, B., Martinez-Delgado, B., Urioste, M., Cigudosa, J. C. and Benitez, J. (2003). Characterization of the A673 cell line (Ewing tumor) by molecular cytogenetic techniques. Cancer Genet Cytogenet. 141, 138-142.

Martins, A. S., Ordonez, J. L., Amaral, A. T., Prins, F., Floris, G., Debiec-Rychter, M., Hogendoorn, P. C. and de Alava, E. (2011). IGF1R signaling in Ewing sarcoma is shaped by clathrin-/caveolin-dependent endocytosis. PLoS One. 6, e19846.

Massotte, D. (2003). G protein-coupled receptor overexpression with baculovirus-insect cell system: a tool for structural and functional studies. Biochem Biophys Acta. 1610, 77-89.

McMahon, H. T. and Boucrot, E. (2011). Molecular mechanism and physiological functions of clathrin-mediated endocytosis. Nat Rev Mol Cell Biol. 12, 517-533.

Meckel, T., Semrau, S., Schaaf, M. J. M. and Schmidt, T. (2011). Robust assessment of protein complex formation in vivo via single-molecule intensity distributions of autofluorescent proteins. J Biomed Opt. 16, 076016

Moss, J., Bruni, P., Hsia, J. A., Tsai, S. C., Watkins, P. A., Halpern, J. L., Burns, D. L., Kanaho, Y., Chang, P. P. and Hewlett, E. L. (1984). Pertussis toxin-catalyzed ADP-ribosylation: effects on the coupling of inhibitory receptors to the adenylate cyclase system. J Recept Res. 4, 459-474.

Mueller W, Schutz D, Nagel F, Schulz S and Stumm R. (2013). Hi-

erarchical organization of multi-site phosphorylation at the CXCR4 C terminus. PLoS One. 8, e64975.

Naumann, U., Cameroni, E., Pruenster, M., Mahabaleshwar, H., Raz, E., Zerwes, H. G., Rot, A. and Thelen, M. (2010). CXCR7 functions as a scavenger for CXCL12 and CXCL11. PLoS One. 5, e9175.

Otsuka, S. and Bebb, G. (2008). The CXCR4/SDF-1 chemokine receptor axis: a new target therapeutic for non-small cell lung cancer. J Thorac Oncol. 3, 1379-1383.

Pelkmans, L. and Helenius, A. (2002). Endocytosis via caveolae. Traffic. 3, 311-320.

Papadopoulou, N., Papakonstanti, E. A., Kallergi, G., Alevizopoulos, K. and Stournaras, C. (2009). Membrane Androgen Receptor Activation in Prostate and Breast Tumor Cells: Molecular Signaling and Clinical Impact. IUBMB Life 61, 56-61.

Rey, M., Valenzuela-Fernandez, A., Urzainqui, A., Yanez-Mo, M., Perez-Martinez, M., Penela, P., Mayor, F. Jr. and SÃ¡nchez-Madrid, F. (2007). Myosin IIA is involved in the endocytosis of CXCR4 induced by SDF-1alpha. J Cell Sci. 120, 1126-1133.

Ritter, S. L. and Hall, R.A. (2009). Fine-tuning of GPCR activity by receptor-interacting protein. Nature Reviews Molecular Cell Biology 10: 819-830.

Rubin, J. B. (2009). Chemokine signaling in cancer: one hump or two? Semin Cancer Biol. 19, 116-122.

Sainz-Jaspeado, M., Lagares-Tena, L., Lasheras, J., Navid, F., Rodriguez-Galindo, C., Mateo-Lozano, S., Notario, V., Sanjuan, X., Garcia Del Muro, X., Fabra, A. and Tirado, O. M. (2010). Caveolin-1 modulates the ability of Ewing's sarcoma to metastasize. Mol Cancer Res. 8, 1489-1500.

Sainz-Jaspeado, M., Huertas-Martinez, J., Lagares-Tena, L., Martin Liberal, J., Mateo-Lozano, S., de Alava, E., de Torres, C., Mora, J., Del Muro, X. G. and Tirado, O. M. (2013). EphA2-induced angiogenesis in ewing sarcoma cells works through bFGF production and is dependent on caveolin-1. PLoS One. 8, e71449.

Samaj, J., Baluska, F., Voigt, B., Schlicht, M., Volkmann, D. and Menzel, D. (2004). Endocytosis, actin cytoskeleton, and signaling. Plant Physiol. 135, 1150-1161.

Saxton, M. J. (1993). Lateral diffusion in an archipelago Single-particle diffusion. Biophys J. 64, 1766-1780.

Schmidt, T., Schutz, G. J., Baumgartner, W., Gruber, H. J. and Schindler, H. (1996). Imaging of single molecule diffusion. Proc Natl Acad Sci U S A. 93, 2926-2929.

Schwartz, V., Kruttgen, A., Weis, J., Weber, C., Ostendorf, T., Lue, H. and Bernhagen, J. (2012). Role for CD74 and CXCR4 in clathrin-dependent endocytosis of the cytokine MIF. Eur J Cell Biol. 91, 435-449.

Semrau, S. and Schmidt, T. (2007). Particle image correlation spectroscopy (PICS): retrieving nanometer-scale correlations from high-density single-molecule position data. Biophys J. 92, 613-621.

Serge A., de Keijzer, S., Van Hemert, F., Hickman, M. R., Hereld, D., Spaink, H. P., Schmidt, T. and Snaar-Jagalska, B. E. (2011). Quantification of GPCR internalization by single-molecule microscopy in living cells. Integr. Biol. 3, 675-683.

Springael, J. Y., Urizar, E. and Parmentier, M. (2005). Dimerization of chemokine receptors and its functional consequences. Cytokine Growth Factor Rev. 16: 611-623.

Stuart, A. D. and Brown, T. D. (2006). Entry of feline calicivirus is dependent on clathrin-mediated endocytosis and acidification in endosomes. J Virol. 80, 7500-7509.

Teicher, B. A. and Fricker, S. P. (2010). CXCL12 (SDF-1)/CXCR4 pathway in cancer. Clin Cancer Res. 16, 2927-2931.

Tirado, O. M., Mateo-Lozano, S., Villar, J., Dettin, L. E., Llort, A., Gallego, S., Ban, J., Kovar, H. and Notario, V. (2006). Caveolin-1 (CAV1) is a target of EWS/FLI-1 and a key determinant of the oncogenic phenotype and tumorigenicity of Ewing's sarcoma cells. Cancer Res. 66, 9937-9947.

Tsao, P., Cao, T. and von Zastrow, M. (2001). Role of endocytosis in mediating downregulation of G-protein-coupled receptors. Trends Pharmacol Sci. 22, 91-96.

Ueda, M., Sako, Y., Tanaka, T., Devreotes, P. and Yanagida, T. (2001). Single-molecule analysis of chemotactic signaling in Dictyostelium cells. Science 294, 864-867.

van Hemert, F., Lazova, M. D., Snaar-Jagaska, B. E. and Schmidt, T. (2010). Mobility of G proteins is heterogeneous and polarized during chemotaxis. J Cell Sci. 123, 2922-2930.

Vassilieva, E. V. and Nusrat, A. (2008). Vesicular trafficking: molecular tools and targets. Methods Mol Biol. 440, 3-14.

Venkatesan, S., Rose, J. J., Lodge, R., Murphy, P. M. and Foley, J. F.

(2003). Distinct mechanisms of agonist-induced endocytosis for human chemokine receptors CCR5 and CXCR4. Mol Biol Cell. 14, 3305-3324.

Vercauteren, D., Vandenbroucke, R. E., Jones, A. T., Rejman, J., Demeester, J., De Smedt, S. C., Sanders, N. N. and Braeckmans, K. (2010). The use of inhibitors to study endocytic pathways of gene carriers: optimization and Pitfalls. Molecular Therapy. 18, 561-569.

Vila-Coro, A. J., Rodriguez-Frade, J. M., Martin De Ana, A., Moreno-Ortiz, M. C., Martinez-A, C. and Mellado, M. (1999). The chemokine SDF-1alpha triggers CXCR4 receptor dimerization and activates the JAK/STAT pathway. FASEB J. 13, 1699-1710.

Wang, L. H., Rothberg, K. G. and Anderson, R. G. (1993). Misassembly of clathrin lattices on endosomes reveals a regulatory switch for coated pit formation. J Cell Biol. 123, 1107-1117.

Wu, B., Chien, E. Y., Mol, C. D., Fenalti, G., Liu, W., Katritch, V., Abagyan, R., Brooun, A., Wells, P., Bi, F. C., Hamel, D. J., Kuhn, P., Handel, T. M., Cherezov, V. and Stevens, R. C. (2010). Structures of the CXCR4 chemokine GPCR with small-molecule and cyclic peptide antagonists. Science. 330, 1066-1071.

Yarar, D., Waterman-Storer, C. M. and Schmid, S. L. (2005). A dynamic actin cytoskeleton functions at multiple stages of clathrin-mediated endocytosis. Mol Biol Cell. 16, 964-975.

Ye, F., Breslow, D. K., Koslover, E. F., Spakowitz, A. J., Nelson, W. J. and Nachury, M. V. (2013). Single molecule imaging reveals a major role for diffusion in the exploration of ciliary space by signaling receptors. eLife 2, e00654.

Chapter 3

Differential activation modes of G_α-subunits in chemokine receptor signaling[1]

[1]Elena Beletkaia and Thomas Schmidt

G-proteins are the front-line signal transducing partners of the G-protein coupled receptors (GPCRs). A single GPCR can be activating various G-proteins. It is believed that a specific combination of various G-proteins together with a tight temporal control of their activation is required to ensure faithful and specific signalling through downstream biochemical cascades. Presumably this level of control is facilitated by different modes of coupling of the G-protein to the receptor. Here we investigated the interaction of the chemokine receptor CXCR4 with its corresponding G-proteins. We showed that indeed $G_{\alpha i}$ *and* $G_{\alpha q}$ *exhibit different coupling modes. Variation in the receptor/G-protein interaction was aligned with the subsequent pathways activation and potentially play an important role in regulating CXCR4 specific signalling in cells.*

3.1 Introduction

G protein-coupled receptors (GPCRs) are a unique family of membrane receptors that control a wide variety of physiological functions from embryogenesis to immune response. Counting to ∼800 members (Fredriksson et al., 2003), GPCRs do not only share a common seven transmembrane-helix structure, but they also share their front-line signal transduction partners, the G-proteins. The heterotrimeric guanine nucleotide-binding proteins (G-proteins) are encoded by 35 genes in the human genome (Milligan and Kostenis, 2006). The 45 kDa heterotrimers includes the 35 kDa α-subunit and two 8-10 kDa polypeptides defined as the β- and γ-subunits (Milligan and Kostenis, 2006). There are 16 different α-, 5 β-, and 14 γ-subunits (G_α, G_β and G_γ, respectively). The G_α subunits are sub-divided into 4 groups: G_αs which regulates an increase in intracellular cyclic adenosine mono-phosphate (cAMP) concentration, $G_{\alpha i/o}$ which regulates a decrease in cAMP concentration, $G_{\alpha q/11}$ which activates phospholipase C (PLC) subsequently leading to increased cytoplasmic Ca^{2+} levels, and $G_{\alpha 12/13}$ which regulates signalling by the small GTPase Rho. The G_β and G_γ subunits occur presumably as stable heterodimers ($G_{\beta\gamma}$) and are shown to activate multiple pathways, which are partially overlapping with those of the G_α subunits. The precise signal translation from multiple ligands to the specific GPCR is enabled by a peculiar combination of the G-protein subunits activating corresponding specific downstream biochemical response.

The mechanisms by which specificity in receptor/G-protein interaction is controlled are not yet well understood. Knowledge about these mechanisms is highly required for the development of novel drugs leading to more precise targeting, and thus avoiding undesired pharmacological side effects. Extensive research of the past years resulted in the development of two models for this initial receptor/G-proteins interaction (Hein and Bunemann, 2008; Hein et al., 2005). The first, so called 'collision coupling' model, assumes that G-proteins and receptors exist as independent entities in the plasma membrane which, by diffusion, are able to collide initiating the interaction and subsequent activation of the G-protein. The second, so called 'pre-coupling' model, assumes that the receptor/G-protein form a stable complex prior to activation, which on activation is disrupted and the G-protein activated. Activation of the G-protein heterotrimer subsequently leads to the loss of $G_\alpha/G_{\beta\gamma}$ interaction and a split of the trimer into a G_α monomer and a $G_{\beta\gamma}$ heterodimer.

The mode of GPCR and G-protein interaction has been addressed for various systems using fluorescence-based methods. Experiments using fluorescence recovery after photobleaching (FRAP) showed that the α_2A-adrenergic receptor did not form stable complexes with its respective $G_{\alpha i}$ (Qin et al., 2008), while for the μ-opioid receptor such interaction with $G_{\alpha o}$ has been found for resting cells (Qin et al., 2008). Further bioluminescence resonant energy transfer (BRET) and fluorescence resonant energy transfer (FRET) approaches showed that interaction of GPCR and G-proteins is a fast, transient process on a time scale of 30-50 ms, suggesting their plausible pre-coupled state (Lohse et al., 2008). Upon activation the FRET signal decreased rapidly, which would be predicted for the dissociation of a pre-complex (Lohse et al., 2008). However, FRET also revealed that only a small fraction of $G_{\alpha i}$ was pre-coupled to the α_2-adrenoceptor (Hein et al., 2005). Single-molecule fluorescence imaging showed that the G-proteins were pre-coupled to the chemokine cAMP-receptor 1 (cAR1) in Dictyostelium discoideum (van Hemert et al., 2010). Hence, different studies provide support for both models, suggesting that the coupling mode of GPCRs and G proteins might be not universal. It seems tempting to speculate that the differential mode of operation for GPCR/G-protein coupling could be an additional mechanism for spatial and temporal signal propagation control in cells.

An interesting GPCR to study with respect to its coupling mode is the chemokine receptor CXCR4. CXCR4 activates four different G_α subunits (Rubin, 2008), with a major role for $G_{\alpha i}$ and $G_{\alpha q}$ (Teicher and Fricker, 2010). We have shown in a prior study that the mobility of CXCR4 in the plasma membrane reflected its interaction with the respective G-protein. The interaction with $G_{\alpha i}$ was essential for receptor immobilization, while the $G_{\alpha q}$ signalling was interfering with CXCR4 internalization after stimulation by its specific ligand CXCL12 (Chapter 2 of this thesis). In the current study, we further addressed the question of the mechanism of CXCR4/G-protein interaction and its involvement in receptor signalling in the Ewing sarcoma-derived cell line A673. Our results revealed that receptor coupling to $G_{\alpha i}$ and $G_{\alpha q}$ followed different coupling models. While the $G_{\alpha i}$-subunit obeyed the 'collision coupling' model, the $G_{\alpha q}$-subunit appeared as pre-coupled with the receptor. Our findings suggest that G-protein activation by CXCR4 occurs in a sequential manner: an early response by the pre-coupled $G_{\alpha q}$, followed by a later response by $G_{\alpha i}$. Whether and how this time-dependent dif-

ferentiation in G-proteins activation might lead to further specificity in CXCR4 signalling will have to be explored in the future.

3.2 Materials and Methods

3.2.1 Cell culture and transfection

Ewing sarcoma A673 wt cells and A673 cells stably transfected with the chemokine receptor CXCR4 (A673-CXCR4) were cultured in IMDM cell culture medium (Gibco, USA) supplemented with 10% fetal bovine serum (200 μg/mL; FBS, Gibco, USA) at 37°C and 5% CO_2. For transient transfection with CXCR4, $G_{\alpha i}$-YFP, $G_{\alpha q}$-YFP or YFP-G_β/G_γ 0.5×10^5 A673 cells were plated on 0.35 mm diameter culture dishes (Ibidi, Germany) and allowed to adhere overnight. For the transfection mix 1 μg of respective plasmid DNA was diluted in 93 μL serum-free medium and mixed with 4 μL Turbofect. The mix was vortexed and incubated for 20 minutes. Cells were incubated with 100 μL of the transfection mix for 2 hours, followed by medium change and overnight incubation to allow for protein synthesis. For co-transfection an equal amount of respective DNA was pre-mixed to a final concentration of 1 μg/μL and total weight of 1 μg plasmid DNA and was used in the transfection mixture.

3.2.2 Confocal microscopy

Confocal microscopy was performed using an Axiovert200 microscope (Zeiss, Germany) combined with a spinning disk unit (CSU-X1, Yokogawa, Japan) and an emCCD camera (iXon 897, Andor, UK) (van Hoorn et al., 2014). Imaging was performed using a 100×/NA1.4 objective (Zeiss) at 514 nm (Cobolt) laser illumination. Time-lapse imaging was performed at 1 second time lag. Where indicated, CXCL12 was added to the media to a final concentration of 100 nM present in the media during the time of the entire experiment.

3.2.3 Single-molecule imaging

Single-molecule fluorescent imaging was carried out using a combination of wide-field microscopy with highly-sensitivity CCD (Princeton Instruments, USA) or high-sensitivity CMOS (Orca flash 4.0v2, Hamamatsu,

Japan) camera detection as described in detailed elsewhere (Schmidt et al., 1996). To excite individual YFP molecules illumination with a 514 nm laser set to 2 kW/cm^2 intensity and illumination time of 5 ms was applied. The signal was subsequently detected on the camera for 1000-1500 frames at a frame-rate of 20-40 Hz. Each fluorescence signal was fit to a 2D-Gaussian intensity distribution yielding the G-protein position to $\sigma = 40$ nm accuracy. Subsequently all results were filtered with respect to a previously determined YFP-footprint signal (van Hemert et al., 2010). For those data particle image correlation spectroscopy (PICS) was used to construct the cumulative distribution of square displacement (*cdf*) characterizing the protein's mobility (Semrau and Schmidt, 2007). Data were subsequently fit to an n = 2 or n = 3 fraction model:

$$cdf(r^2, t, n) = 1 - \left(\Sigma_{i=1}^{n} \alpha_i \cdot exp(\frac{-r^2}{MSD_i(t)})\right) \tag{3.1}$$

where r^2 is the squared displacement, α_i are the respective normalized fraction sizes ($\Sigma\alpha_i = 1$) of proteins with characteristic mean square displacement MSD$_i$(t) and lag-time t. For free diffusion the MSD is related to the diffusion constant D as

$$MSD_i = 4 \cdot D_i \cdot t + s_0 \tag{3.2}$$

and for confined diffusion at characteristic domain size L as

$$MSD(t) = \frac{L^2}{3} \cdot \left(1 - exp(\frac{-12 \cdot D \cdot t}{L^2})\right) + s_0 \tag{3.3}$$

In eq.(3.2) and eq.(3.3) s_0 is an offset in MSD due to the localization precision of individual proteins ($s_0 = 4\sigma^2$). Generally the MSD and α were calculated separately for each experiment. In some indicated experiments data were fit globally, with α as a free parameter and common MSDs.

3.3 Results

3.3.1 Receptor interaction is required for G-protein localization to the plasma membrane

Here we used an Ewing sarcoma-derived cells line, A673, to follow the G-protein activation upon cell-stimulation through the chemokine receptor

CXCR4. Cells were transiently transfected with either of the G-proteins, $G_{\alpha i}$-YFP, $G_{\alpha q}$-YFP including co-transfection with YFP-$G_{\beta 2}$ and $G_{\gamma 1}$ (further referred to as $G_{\beta\gamma}$-YFP) as described in Materials and Methods. It should be noted that transfection was additional to the endogenous G-protein levels present in A673 cells. Confocal imaging revealed that the expressed YFP-labeled G-proteins did not show prominent plasma membrane localization (Fig. 3.1A). The YFP-signal was predominantly found in the cytoplasm. Taken that $G_{\alpha i}$, $G_{\alpha q}$ and $G_{\beta\gamma}$ do have a membrane anchor, this suggests that the lipid anchor was not sufficient for plasma membrane localization and that specific interactions of the G-proteins with their respective GPCR-receptor was required for proper targeting. Presumably, the overexpression of G-proteins led to saturation of the endogenously expressed receptors, and, hence, affected their localization.

We tested the latter hypothesis by co-expressing G-proteins and the chemokine receptor CXCR4 such as to achieve a balanced expression of the $G_{\alpha i}$-YFP, $G_{\alpha q}$-YFP, $G_{\beta\gamma}$-YFP and the CXCR4, respectively. Since A673 cells exhibit only a low expression of endogenous CXCR4 (Sand et al., in press), co-expression led to a massive increase of CXCR4 in the cells. Since all constructs used the same promoter sequence and because we transfected with identical amounts of DNA, we assumed that similar amounts of the respective proteins were synthesized.

Confocal imaging confirmed our earlier hypothesis. Co-expression of the receptor with the G-proteins resulted in a pronounced plasma membrane localization of a fraction of both, $G_{\alpha i}$ and $G_{\alpha q}$ subunits (Fig. 3.1B). A large fraction of $G_{\alpha i}$ and $G_{\alpha q}$ stayed cytosolic (Fig. 1B). This finding corroborates earlier reports in which G_{α} subunits were shown to appear as both membrane-bound and cytosolic fractions (Bunemann et al., 2003). The increase in plasma membrane localization with overexpression of the receptor further suggests that a fraction of G-proteins was pre-coupled to their receptor. It is interesting to note that the localization of $G_{\beta\gamma}$ was unaltered on co-expression with CXCR4 (Fig. 3.1B). The latter finding was predicted, given that receptor/G-protein interaction is mediated by G_{α} but not by $G_{\beta\gamma}$ (Hamm, 2001).

Subsequently, we examined how activation of CXCR4 would affect localization of the G-proteins. We applied a continuous global stimulation with 100 nM of its specific ligand CXCL12 during time-lapse confocal imaging. At the cell perimeter no obvious change in $G_{\alpha i}$ lo-

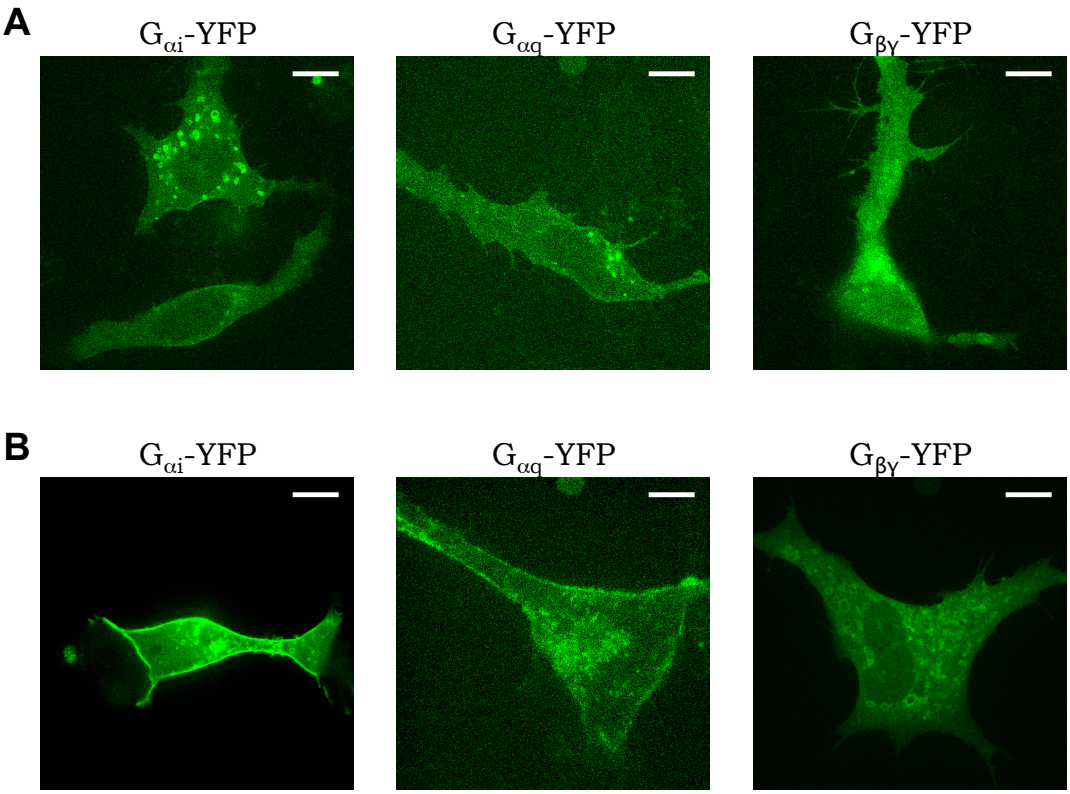

Figure 3.1
A. *A673 cells transfected with $G_{\alpha i}$-YFP, $G_{\alpha q}$-YFP or $G_{\beta\gamma}$-YFP.* ***B.*** *Co-expression of $G_{\alpha i}$-YFP, $G_{\alpha q}$-YFP or $G_{\beta\gamma}$-YFP with CXCR4. Images were acquired 24 hours after transfection. Scale bar - 10 μm.*

calization was observed. It should be noted that imaging of a specific response on a short time-scale would require a low cellular background signal, which is in contradiction with the level of $G_{\alpha i}$-YFP expression present in transfection experiments. Hence, we concentrated our further analysis to the thin membrane protrusions, which extended from the cell body (Fig. 3.2). At those locations addition of CXCL12 resulted in a prompt response of $G_{\alpha i}$ subunits. After ~5 s of CXCL12 stimulation, $G_{\alpha i}$ exhibited a strong accumulation in small cluster-like structures seen as localized increased YFP signals (Fig. 3.2A). The clustering lasted for 20-25 s. The $G_{\alpha q}$ subunit showed a similar accumulation in cluster-like structures with the same dynamic behavior (Fig. 3.2B). Both for $G_{\alpha i}$ and $G_{\alpha q}$ clustering did not re-occur for at least the following 30 minutes (length of the experiment; data not shown). Thus, $G_{\alpha i}$ and $G_{\alpha q}$

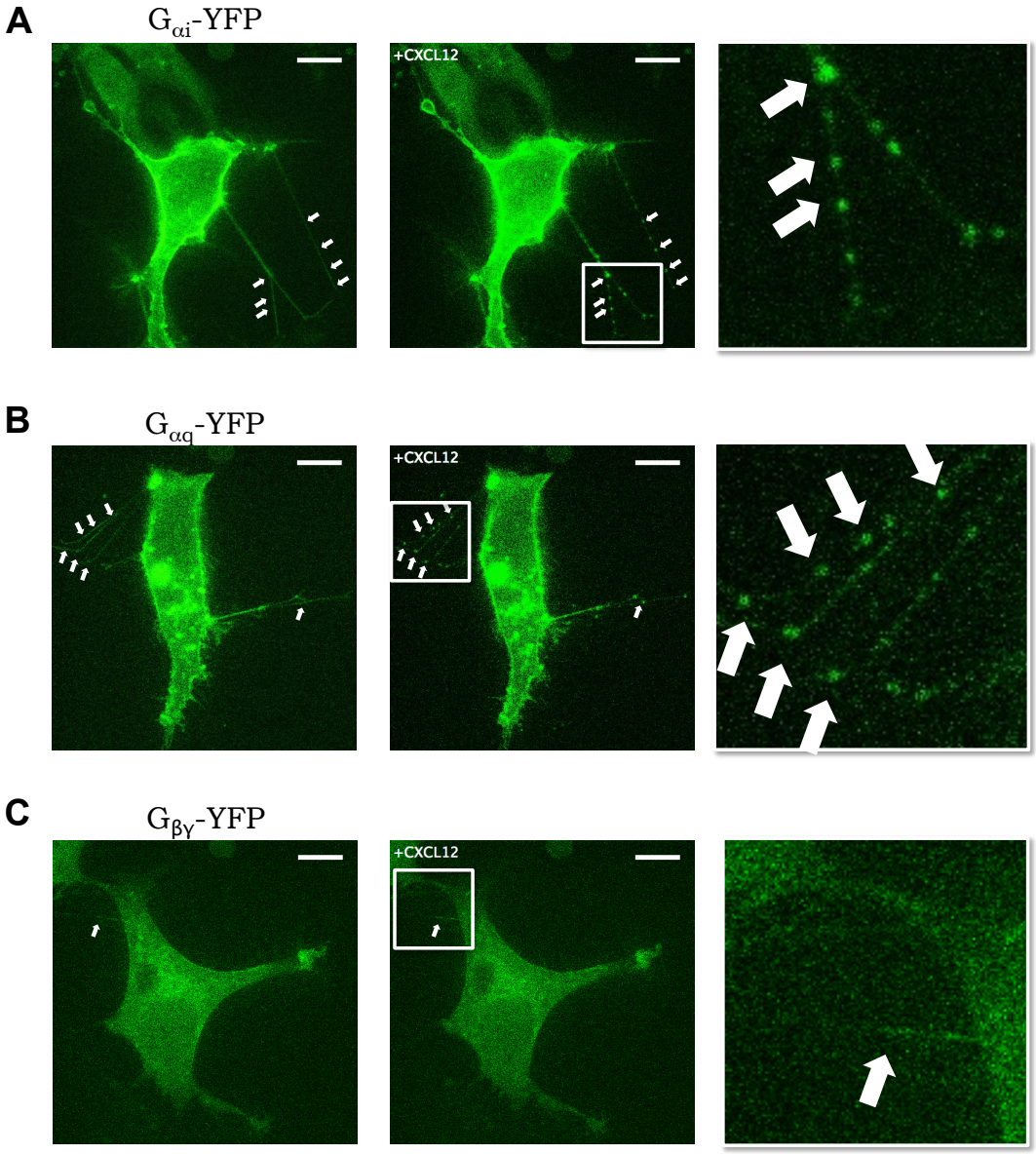

Figure 3.2
*A673 cells co-expressing of $G_{\alpha i}$-YFP **(A)**, $G_{\alpha q}$-YFP **(B)** or $G_{\beta\gamma}$-YFP **(C)** with CXCR4 before (left) and during (middle and right) global stimulation of CXCR4 with 100 nM of CXCL12. Scale bar - 10 μm.*

subunits exhibit a fast short-term response upon CXCR4 receptor activation. CXCL12 stimulation did not display a similar effect on the $G_{\beta\gamma}$ subunits during the first seconds of incubation with the ligand (Fig. 3.2C).

In summary, the results showed that activation of CXCR4 is followed by a re-localization of the plasma membrane-bound fraction of G-proteins. Given that the response was fast, on the timescale of seconds, we in turn hypothesized that a fraction of the G proteins potentially was pre-coupled to the receptor in order to allow for the fast response observed.

3.3.2 Mobility of membrane proteins is unaltered on cell-substrate adhesion

To obtain a deeper insight into the behavior of the membrane-anchored fraction of G-proteins and learn about the dynamic behavior after cell stimulation we applied single-molecule fluorescence microscopy. Inasmuch as G-proteins were present in two fractions, a cytoplasmic and a membrane-anchored fraction, single-molecule experiments required restriction of our analysis to the thin (least cytoplasm-containing) parts of the cell. In this configuration it is experimentally difficult to distinguish top and bottom membrane of a cell during the single-molecule imaging. Thus, we used a well-studied control system, CXCR4-YFP in A673 cells (Chapter 2 of this thesis), to elicit whether membrane interaction with the surface of the dish would affect the motility of membrane-associated molecules.

Similar to our previous study (Chapter 2 of this thesis), we accessed the diffusion dynamics of individual CXCR4-YFP on the millisecond time-scale as described in Materials and Methods. We detected individual CXCR4-YFP with ∼40 nm localization precision and determined their mobility on the proximal (bottom) and the distal (top) plasma membrane.

As reported earlier two fractions of different mobility were observed, in which one was mobile and the other immobile. The fraction size α, and mean square displacements (MSD) were determined subsequently. Our results showed that the MSD was indistinguishable between the top (filled black and red circles) and the bottom (open black and red circles) membrane when observed for time-lags between 50 and 250 ms (Fig. 3.3A).

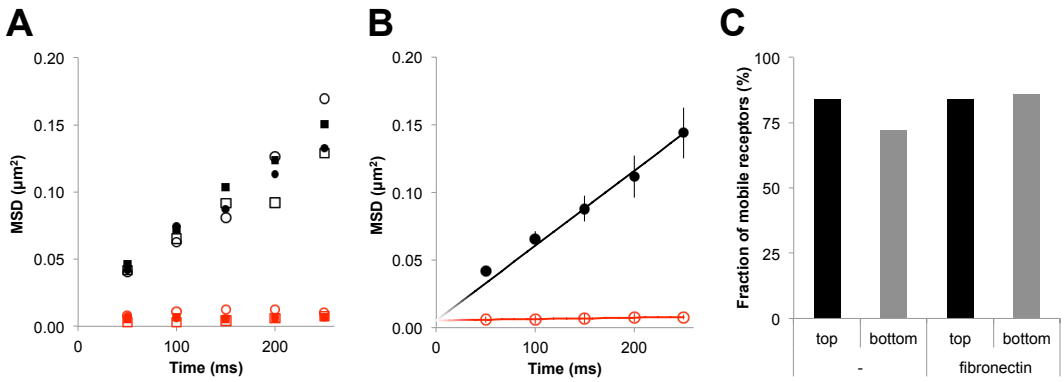

Figure 3.3
Comparison of CXCR4 mobility at top and bottom part of the plasma membrane. ***A.*** *Mean square displacement of mobile (black) and immobile (red) receptors determined at the top (filled symbols) and bottom (open symbols) membrane of cells placed on plastic dishes (circles) or on dishes pre-coated with fibronectin (squares).* ***B.*** *Change of mean square displacement (MSD) with time for mobile (black circles) and immobile (red open circles) receptors. Data were fit to a free diffusion model (black and red lines).* ***C.*** *Comparison of the fractions of mobile receptors detected at the top (black) and bottom (grey) membrane for cells placed on non-treated or fibronectin pre-coated dishes.*

The linear dependence of the mean squared displacement with time lag confirmed that the mobility for the mobile fraction was described by free diffusion, characterized by a diffusion coefficient of D_{CXCR4} = 0.14±0.01 $\mu m^2/s$ (Fig. 3.3B). The fraction size of the mobile receptors on top and bottom membranes was identical within error and yielded ∼80% (Fig. 3.3C). All values were in excellent agreement with the values reported earlier by us for the distal membrane (Chapter 2 of this thesis).

We further examined whether enhanced cell adhesion would affect diffusion of the receptors. A673-CXCR4 cells were placed on dishes that were pre-coated with fibronectin. Interaction of the cells with fibronectin did not alter the mobility of CXCR4 (Fig. 3.3). Both the diffusion coefficient (Fig. 3.3A,B) and the size of the mobile fraction (Fig. 3.3C) resembled those of the control.

Our results demonstrate that membrane interaction with the surface of the dish did not alter the diffusion dynamics of the trans-membrane chemokine receptor CXCR4. Hence, it is conceivable that the mobility of G-proteins, which are only membrane-bound to the inner plasma membrane leaflet, would be likewise undisturbed. This finding largely

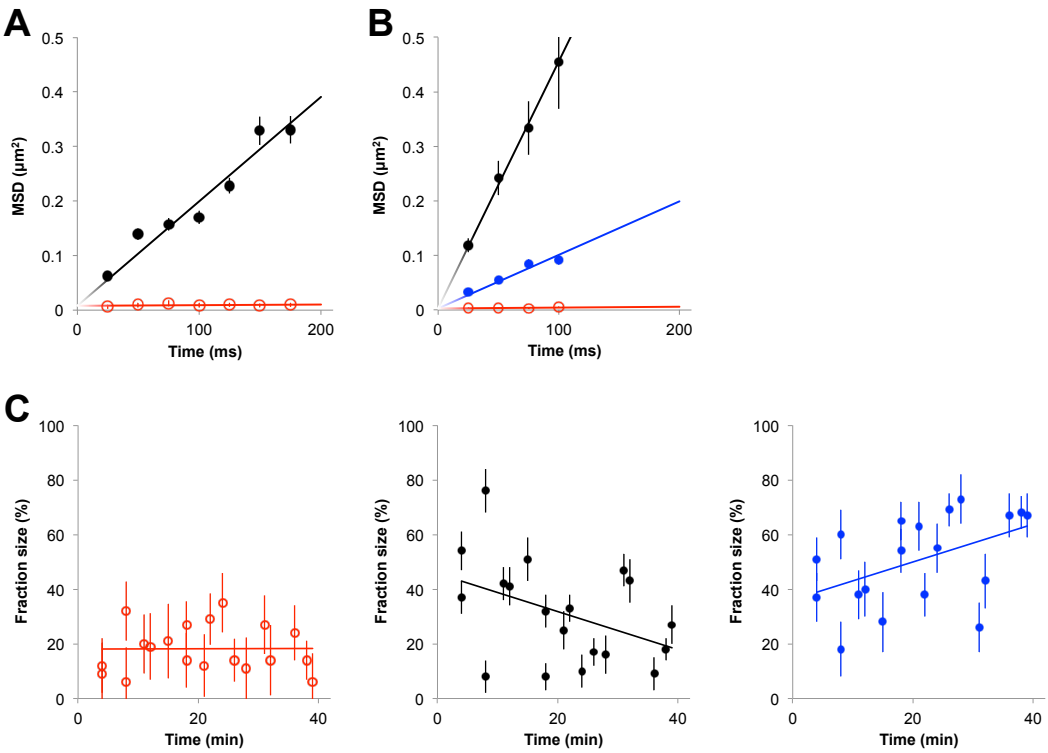

Figure 3.4
Mobility of $G_{\alpha i}$. ***A.*** *MSD vs. time determined for fast diffusing (black) and immobile (red) $G_{\alpha i}$ molecules in resting A673 cells.* ***B.*** *MSD of fast diffusing (black), slow diffusing (blue) and immobile (red) molecules for cells stimulated by 100 nM of CXCL12. The data were globally fitted to a 3-fraction diffusion model. Solid lines represent the respective fit of the data.* ***C.*** *Time-dependent change of the fraction sizes of immobile (open red) and fast (black) and slow (blue) diffusing $G_{\alpha i}$ molecules during continuous stimulation of CXCR4 with 100 nM CXCL12.*

simplified further experiments since it did not require the distinction of the top and bottom membrane in the analysis.

3.3.3 Binding of $G_{\alpha i}$ to CXCR4 requires receptor activation

Single-molecule imaging was used to study the mobility of individual membrane-bound G-protein subunits. As anchoring of G-proteins to the plasma membrane is facilitated through a membrane-binding lipid moiety, which is much smaller compared to the size of the CXCR4 receptor, one can predict that receptor-decoupled G-proteins were characterized

by a significantly increased diffusion constant in relation to GPCR-bound G-proteins.

In resting cells the $G_{\alpha i}$-subunits existed in two fractions, a mobile and an immobile fraction (Fig. 3.4A). The mobile fraction of 76±2%, followed free diffusion characterized by a diffusion coefficient of $D_{G\alpha i}$ = 0.48±0.02 $\mu m^2/s$. This value was significantly higher than that of the CXCR4 receptor (D_{CXCR4} = 0.14 ± 0.01 $\mu m^2/s$). Thus, our results confirmed the prediction made above. For resting cells there was no detectable fraction of $G_{\alpha i}$ that would exhibit a diffusion behavior similar to the mobile fraction of the CXCR4. This observation leads to the conjecture that the mobile fractions of $G_{\alpha i}$ and CXCR4 were not coupled prior to CXCL12 stimulation.

Next we applied 100 nM of CXCL12 to specifically activate CXCR4 and subsequently monitored changes in the mobility of $G_{\alpha i}$. Our results revealed, that there was no significant change in the size of the immobile fraction of $G_{\alpha i}$, compared to that before stimulation (18±9 % and 24±2 %, respectively). Taken our earlier finding that the fraction of immobile CXCR4 increased upon activation, this result suggested that the immobile fraction of the $G_{\alpha i}$ was also independent and not coupled to the immobile receptors (Chapter 2 of this thesis). Further we found that the mobile fraction of the $G_{\alpha i}$-subunits was split into two diffusive fractions, a fast and a slow fraction (Fig. 3.4B) with diffusion coefficients $D_{G\alpha i(fast)}$ = 1.13±0.02 $\mu m^2/s$ and $D_{G\alpha i(slow)}$ = 0.25±0.01 $\mu m^2/s$, respectively. The diffusion coefficient of the slow fraction was comparable to that of the mobile CXCR4 receptor. This finding implies that CXCL12 stimulation lead to a physical interaction of $G_{\alpha i}$ and CXCR4, which lasted at least for 150 ms, the longest time-lag we investigated.

We next followed the value of the mobile fractions of $G_{\alpha i}$ after continued stimulation with CXCL12 for 30 minutes. On this time scale the size of the fast fraction (Fig. 3.4C, middle) exhibited a tendency to decrease at a rate of $\sim$1%min^{-1}. Interestingly, we observed the appearance of the slow fraction of $G_{\alpha i}$ within the first minutes after CXCL12 addition exhibiting a tendency to increase at the same rate. This result is in excellent agreement with earlier findings by FRET that showed the onset of $G_{\alpha i}$/receptor coupling on time scale of seconds (Bunemann et al., 2003).

Thus, our data showed that interaction of $G_{\alpha i}$ with CXCR4 is dependent on and occurs after receptor stimulation, suggesting that $G_{\alpha i}$/

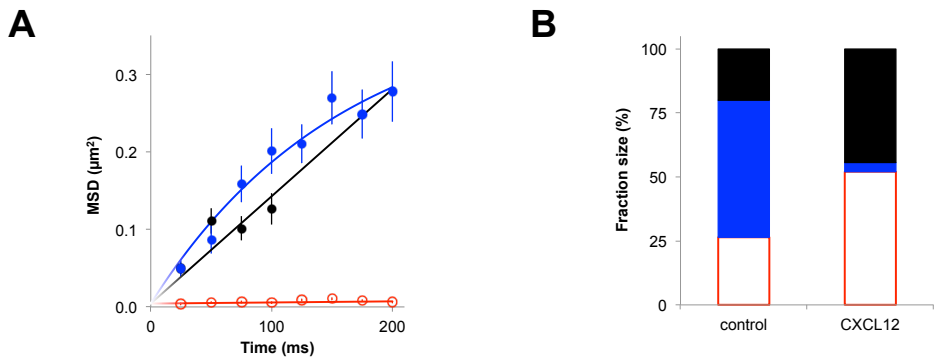

Figure 3.5
Mobility of $G_{\alpha q}$. ***A.*** *Mean square displacement (MSD) of fast diffusing (black), confined (blue) and immobile (red) molecules as resulting from a global fit of the resting and CXCL12 stimulated cells. Solid lines represent the respective fit of the data. The linear size of the confinement zone yielded $L = 1.1 \pm 0.1$ µm.* ***B.*** *Comparison of fraction sizes of fast diffusing (black), confined (blue) and immobile (open red) $G_{\alpha q}$ molecules in resting cells or upon CXCR4 activation with 100 nM CXCL12.*

CXCR4 follows a 'collision coupling' model described earlier (Hein and Bunemann, 2008).

3.3.4 $G_{\alpha q}$ is pre-coupled to an inactive CXCR4 receptor

Next we addressed the mobility of individual $G_{\alpha q}$ subunits. Similar to the $G_{\alpha i}$ subunits, $G_{\alpha q}$ existed in mobile and immobile states in resting cells. However, already before activation of the receptor, the mobile fraction of the $G_{\alpha q}$-subunits was split into 2 populations (Fig. 3.5), a fast fraction characterized by $D_{G\alpha q(fast)} = 0.35 \pm 0.04$ $\mu m^2/s$ and a slow fraction characterized by $D_{G\alpha q(slow)} = 0.15 \pm 0.02$ $\mu m^2/s$. To our surprise, the fraction of slow $G_{\alpha q}$ molecules (54±11%) was the dominant fraction (Fig. 3.5B). Activation of CXCR4 by 100 nM CXCL12 resulted in a drastic change in $G_{\alpha q}$ fraction sizes (Fig. 3.5B). The fast fraction increased to 44±5% compared to resting cells (20±14%), while the slow fraction dropped to 4±3% when compared to the resting state (54±11%). Moreover, the fraction of immobile $G_{\alpha q}$-subunits increased from 26±18% in resting cells to 52±6% in cells with activated CXCR4 receptors (Fig. 3.5B).

These results suggest that, in contrast to the $G_{\alpha i}$ subunit, $G_{\alpha q}$ ap-

peared to be pre-coupled to the CXCR4 receptor in resting cells. Upon receptor activation $G_{\alpha q}$ subunits either uncouple from CXCR4, as reflected in an increase of the fast fraction, or are immobilized. Earlier we reported a likewise immobilization of CXCR4 upon stimulation that was related to receptor internalization (Chapter 2 of this thesis), suggesting that the immobilized $G_{\alpha q}$ fraction might be associated to a receptor/G-protein complex destined to internalization.

3.4 Discussion

Signalling by the chemokine receptor CXCR4 is a complex process which includes activation of G-protein dependent and independent pathways ultimately regulating gene expression, cell proliferation, survival, and chemotaxis (Teicher and Fricker, 2010). The ensemble of G-protein dependent pathways activated by CXCR4 involves signalling through four various G_{α} subunits (Rubin, 2008). Thus, the orchestration of all the signalling cascades in time and space has to be tightly controlled. Here we investigated the mechanism of CXCR4 interaction with G-proteins and its relation to the receptor signalling. Our data suggested a sequential receptor binding of $G_{\alpha q}$ and $G_{\alpha i}$, which would result in a temporal ordering of the signalling (Fig. 3.6).

In the inactive state CXCR4 appeared to be coupled to the $G_{\alpha q}$ subunit. This conclusion followed from the detected fraction of $G_{\alpha q}$ that displayed an identical mobility when compared to the mobility of the inactive CXCR4. Furthermore, the respective fraction was lost after receptor activation by CXCL12, implying uncoupling of $G_{\alpha q}$ from the receptor after activation. It is known that $G_{\alpha q}$ activation leads to a Ca^{2+} influx through the phospholipase-Cβ (PLCβ) pathway (Rubin, 2008). The Ca^{2+} influx is fast, observable from the first moments after receptor activation (Fig. 3.6), indicating immediate triggering of the PLCβ cascade, thus, further supporting our assumption of pre-coupling of $G_{\alpha q}$ to CXCR4.

The release of $G_{\alpha q}$-subunit from the stimulated receptor subsequently allows coupling of the $G_{\alpha i}$-subunit to CXCR4 with concomitant activation of $G_{\alpha i}$. This conclusion followed from our mobility analysis, which suggested that in the inactive state CXCR4 was not coupled with $G_{\alpha i}$. Upon CXCR4 stimulation with CXCL12 a receptor-bound fraction of $G_{\alpha i}$ was observed. This receptor-bound fraction of $G_{\alpha i}$ increased with

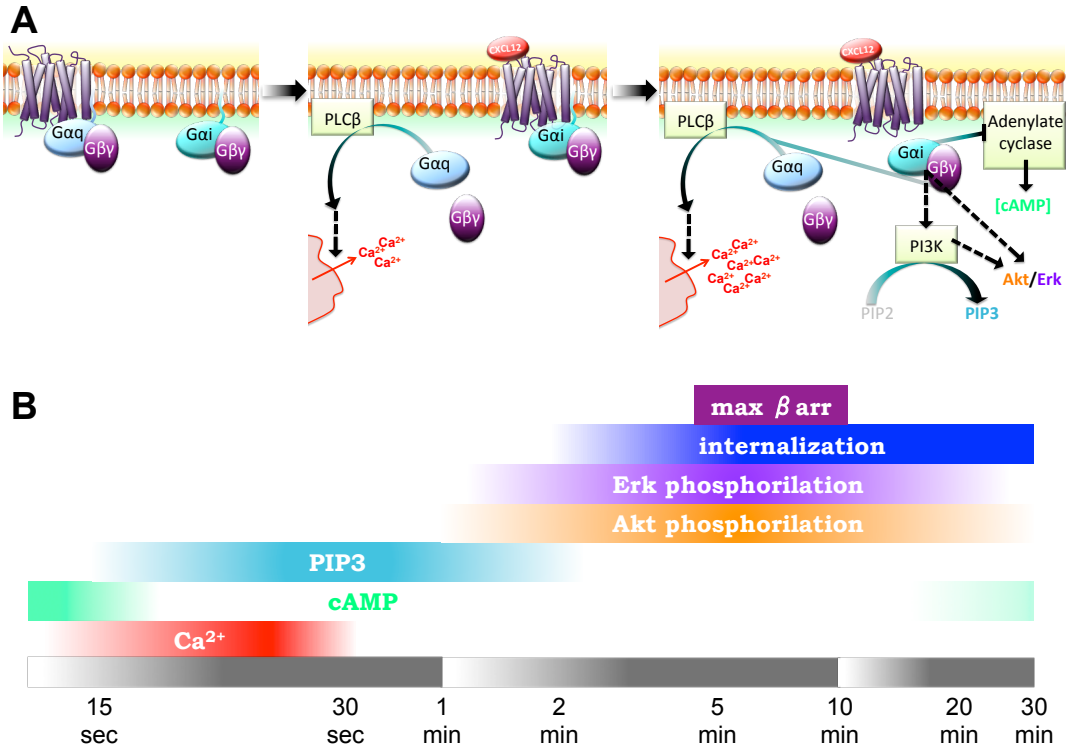

Figure 3.6

Schematic representation of the CXCR4 signalling sequence. ***A.*** *Model of sequential activation of the G-proteins and respective pathways.* ***B.*** *The time-line (in log scale) of CXCR4 signalling after CXCL12 stimulation. The slow increase and fast decrease of* Ca^{2+} *flux is detected from the first moments and lasts for ∼20-30 seconds (Arnolds et al., 2013; Busillo et al., 2010; Mueller et al., 2013; Sotsios et al., 1999; Tripathi et al., 2014). A decrease of cAMP concentration is delayed and has a prolongated effect of ∼30 minutes (Yang et al., 2007). Between ∼15 seconds and 2 minutes after receptor activation, an elevated concentration of PIP3 is detected (Sotsios et al., 1999). A maximum of Akt and Erk phosphorylation is attained 5-10 minutes after stimulation (Brennecke et al., 2014; Kawaguchi et al., 2009; Sotsios et al., 1999; Torossian et al., 2014; Wojcechowskyj et al., 2011; Zhao et al., 2006). G-protein independent receptor internalization is detected as soon as 2 minutes after addition of the ligand (Busillo et al., 2010; Mueller et al., 2013; Tripathi et al., 2014; Venkatesan, 2003). A maximum of β-arrestin recruitment appears at 5-10 minutes (Busillo et al., 2010).*

time, suggesting a prolonged activation of $G_{\alpha i}$. It is known that $G_{\alpha i}$ activation results in a decrease of intracellular cyclic AMP (cAMP) concentration through the adenylate cyclase inhibition (Fig. 3.6). This decrease has been observed with a delay after receptor activation and has been reported as long lasting (Fig. 3.6) (Yang et al., 2007). Those earlier biochemical findings were corroborated by our findings based on protein mobility showing a delayed and prolonged $G_{\alpha i}$/CXCR4 coupling.

It is interesting to note that $G_{\alpha q}$ and $G_{\alpha i}$ subunits were shown cross-activate intracellular signalling pathways. Activation of $G_{\alpha q/11}$-coupled receptors was shown to be crucial for signalling by various $G_{\alpha i/o}$-coupled receptors (Bakker et al., 2004). For instance, $G_{\alpha q}$-stimulated PLCβ-activity was increased by $G_{\alpha i}$-linked receptors (Chan et al., 2000). Hence, the sequential activation of $G_{\alpha q}$ and $G_{\alpha i}$ by CXCR4 could be a mechanism to control the activation of specific pathways. One potential scenario would be that receptor activation causes an immediate activation of the pre-coupled $G_{\alpha q}$ and, thus, of PLCβ followed by $G_{\alpha q}$ uncoupling. The sequential and prolonged interaction of CXCR4 with $G_{\alpha i}$, in turn would further promote PLCβ signalling. Inasmuch as the PLCβ-pathway is associated with the chemotactic response (Teicher and Fricker, 2010) such a signalling control and amplification mechanism might be involved in the initial steps of the gradient sensing.

In summary, our results showed that the chemokine receptor CXCR4 has a differential coupling with various G_{α}-subunits. The coupling with $G_{\alpha q}$ corresponds to 'pre-coupled' model, while coupling with $G_{\alpha i}$ follows 'collision coupling' model. Such difference in the coupling appears to be a mechanism of controlling the subsequent activation of respective pathways and, thus, an important mechanism to specific CXCR4 signal transduction.

3.5 Acknowlegement

We would like to thank the Bunemann Lab, who generously shared the G-protein containing plasmids. We would like to thank Sylvie Olthuis for preparation of the described clones of the plasmids.

3.6 References

Arnolds, K., Lares, A., and Spencer, J. (2013). The US27 gene product of human cytomegalovirus enhances signalling of host chemokine receptor CXCR4. Virology.

Bakker, R., Casarosa, P., Timmerman, H., Smit, M., and Leurs, R. (2004). Constitutively active Gq/11-coupled Receptors Enable Signaling by Co-expressed Gi/o-coupled Receptors. Journal of Biological Chemistry.

Brennecke, P., Arlt, M., Campanile, C., Husmann, K., Gvozdenovic, A., Apuzzo, T., Thelen, M., Born, W., and Fuchs, B. (2014). CXCR4 antibody treatment suppresses metastatic spread to the lung of intratibial human osteosarcoma xenografts in mice. Clin Exp Metastasis.

Bunemann, M., Frank, M., and Lohse, M.J. (2003). Gi protein activation in intact cells involves subunit rearrangement rather than dissociation. Proc. Natl. Acad. Sci. U.S.A. 100, 16077-16082.

Busillo, JM, Armando, S, Sengupta, R, and Meucci, O (2010). Site-specific phosphorylation of CXCR4 is dynamically regulated by multiple kinases and results in differential modulation of CXCR4 signaling. Journal of Biological

Chan, J.S., Lee, J.W., Ho, M.K., and Wong, Y.H. (2000). Preactivation permits subsequent stimulation of phospholipase C by G(i)-coupled receptors. Mol. Pharmacol. 57, 700-708.

Fredriksson, R., Lagerstrom, M.C., Lundin, L.-G.G., and Schioth, H.B. (2003). The G-protein-coupled receptors in the human genome form five main families. Phylogenetic analysis, paralogon groups, and fingerprints. Mol. Pharmacol. 63, 1256-1272.

Hamm, H. (2001). How activated receptors couple to G proteins. Proceedings of the National Academy of Sciences.

Hein, P., and Bunemann, M. (2008). Coupling mode of receptors and G proteins. Naunyn-Schmied Arch Pharmacol.

Hein, P., Frank, M., Hoffmann, C., Lohse, M.J., and Bunemann, M. (2005). Dynamics of receptor/G protein coupling in living cells. EMBO J. 24, 4106-4114.

Van Hemert, F., Lazova, M.D., Snaar-Jagaska, B.E., and Schmidt, T. (2010). Mobility of G proteins is heterogeneous and polarized during chemotaxis. J. Cell. Sci. 123, 2922-2930.

Van Hoorn, H., Harkes, R., Spiesz, E.M., Storm, C., van Noort, D., Ladoux, B., and Schmidt, T. (2014). The nanoscale architecture of

force-bearing focal adhesions. Nano Lett. 14, 4257-4262.

Kawaguchi, A., Orba, Y., Kimura, T., Iha, H., Ogata, M., Tsuji, T., Ainai, A., Sata, T., Okamoto, T., Hall, W.W., et al. (2009). Inhibition of the SDF-1alpha-CXCR4 axis by the CXCR4 antagonist AMD3100 suppresses the migration of cultured cells from ATL patients and murine lymphoblastoid cells from HTLV-I Tax transgenic mice. Blood 114, 2961-2968.

Lohse, M.J., Hein, P., Hoffmann, C., Nikolaev, V.O., Vilardaga, J.-P.P., and Bunemann, M. (2008). Kinetics of G-protein-coupled receptor signals in intact cells. Br. J. Pharmacol. 153 Suppl 1, S125-32.

Milligan, G., and Kostenis, E. (2006). Heterotrimeric G-proteins: a short history. British Journal of Pharmacology.

Mueller, W, Schutz, D, Nagel, F, Schulz, S, and Stumm, R (2013). Hierarchical organization of multi-site phosphorylation at the CXCR4 C terminus.

Qin, K., Sethi, P.R., and Lambert, N.A. (2008). Abundance and stability of complexes containing inactive G protein-coupled receptors and G proteins. FASEB J. 22, 2920-2927.

Rubin, J. (2008). Chemokine signaling in cancer: one hump or two? Semin. Cancer Biol.

Schmidt, T, Schutz, GJ, and Baumgartner, W (1996). Imaging of single molecule diffusion. Proceedings of the

Semrau, S, and Schmidt, T (2007). Particle image correlation spectroscopy (PICS): retrieving nanometer-scale correlations from high-density single-molecule position data. Biophysical Journal.

Sotsios, Y., Whittaker, G.C., Westwick, J., and Ward, S.G. (1999). The CXC chemokine stromal cell-derived factor activates a Gi-coupled phosphoinositide 3-kinase in T lymphocytes. The Journal of Immunology 163, 5954-5963.

Teicher, and Fricker (2010). CXCL12 (SDF-1)/CXCR4 Pathway in Cancer. Clinical Cancer Research.

Torossian, F., Anginot, A., Chabanon, A., Clay, D., Guerton, B., Desterke, C., Boutin, L., Marullo, S., Scott, M.G., Lataillade, J.-J.J., et al. (2014). CXCR7 participates in CXCL12-induced CD34+ cell cycling through β-arrestin-dependent Akt activation. Blood 123, 191-202.

Tripathi, A., Davis, J.D., Staren, D.M., Volkman, B.F., and Majetschak, M. (2014). CXC chemokine receptor 4 signaling upon co-activation with stromal cell-derived factor-1α and ubiquitin. Cytokine

65, 121-125.

Venkatesan (2003). Distinct Mechanisms of Agonist-induced Endocytosis for Human Chemokine Receptors CCR5 and CXCR4. Molecular Biology of the Cell.

Wojcechowskyj, J.A., Lee, J.Y., Seeholzer, S.H., and Doms, R.W. (2011). Quantitative phosphoproteomics of CXCL12 (SDF-1) signaling. PLoS ONE 6, e24918.

Yang, L., Jackson, E., Woerner, M., Perry, A., Piwnica-Worms, D., and Rubin, J. (2007). Blocking CXCR4-Mediated Cyclic AMP Suppression Inhibits Brain Tumor Growth In vivo. Cancer Research.

Zhao, M, DiScipio, RG, and Wimmer, AG (2006). Regulation of CXCR4-mediated nuclear translocation of extracellular signal-related kinases 1 and 2. Molecular Pharmacology.

Chapter 4

Construction of an All-Optical Controlled G-Protein Coupled Chemokine Receptor[1]

[1]Elena Beletkaia, Sylvie Olthuis-Meunier and Thomas Schmidt

G-protein coupled receptors (GPCR) occupy ∼3% of the human genome and represent a key target of the pharmaceutical market. Despite extensive development of biochemical and biophysical assays devoted to GPCR research, the development of new tools allowing achievement of a precise temporal and spatial control on the experimental system is required. Here we describe the application of the emergent high-potential research tool of optogenetics as a tool to study GPCRs. Optogenetics is based on a combination of genetic targeting and optical stimulation. We describe in detail the steps for the design and the cloning of a chimeric protein consisting of a light-activated GPCR, rhodopsin, and a chemokine receptor, CXCR4. We show that the chimeric receptor optoCXCR4 exhibits plasma membrane localization under appropriate conditions. Here we made the first steps in the development of a chimeric receptor, which could be used for further detailed investigation of CXCR4 signalling with high temporal and spatial resolution. Further developments are required to optimize optoCXCR4 application to more extended biophysical studies on GPCR signalling.

4.1 Introduction

More than 800 genes in the human genome are encoding for transmembrane G-protein coupled receptors (GPCRs) (Fredriksson et al., 2003). With this number, GPCRs represent the largest family of membrane proteins. Members of this family induce a wide variety of cellular functions, among which neurotransmission, blood pressure regulation, heart-rate regulation, and immune response, making this protein family the largest target of modern drugs. Almost half of all prescribed drugs today target GPCRs (Wess et al., 2008).

Phylogenetic analysis revealed that the GPCR family is divided into 5 sub-families as to their main physiological outcome: the adhesion family regulating tissue integrity; the secretin family controlling hormone response; the glutamate family important in neurotransmission; the frizzeled family important for embryo development; and the rhodopsin family which includes receptors for vision (Fredriksson et al., 2003). The rhodopsin family, which encompasses a wide variety of functionality, constitutes by far the largest sub-family (701 receptor) forming 4 groups: α, β, γ, δ. The δ-group of rhodopsin receptors includes the chemokine receptor cluster (Fredriksson et al., 2003). Chemokine receptors are receptors to small peptide molecules, chemokines, which are released in the body to pass information on long length scales. Activation of chemokine receptors is a key to directional cell migration called chemotaxis. Chemotaxis is essential for multiple physiological and pathological processes like embryogenesis, immune response, angiogenesis, inflammation, and metastasis.

Given their central role in inflammation and metastasis, chemokine receptors acquired quite some scientific interest. Activation of the chemokine receptors propagates biochemical reactions causing membrane protrusion formation towards higher concentrations (gradient) of the ligand. Subsequent cellular movement ultimately results in directional cell migration toward the source of ligand expression. Several models of gradient sensing were proposed. However, the direction recognition mechanism by chemokine receptors is still a topic of debate. One of the experimental challenges in the study of chemokine receptor functionality in a life cell setting is the application of precisely timed, well controlled (in terms of concentration, steepness, direction, and location) and stable chemical gradients.

Initially such chemical gradients were produced by micropipettes

filled with the chemoattractant. Although well-defined gradients could be obtained in such a way, gradients were stable only for a limited time and could be modulated only at limited frequencies. Moreover, experiments required a significant amount of material, which frequently rendered such experiments unreasonable. The development of microfluidic devices allowed the creation of long-time stable gradients which, depending on design, made high-frequency chemical modulation possible. Further, the microfluidic approach required only a minimum of material. However, compared to the earlier micropipette experiments, the microfluidics approach comprised a major disadvantage. The direction of the chemical gradient is predefined by design prior to the experiment and a gradual change in gradient direction with time is essentially impossible.

Both techniques generate gradients that extend at least on the size of a cell. Although this might reflect the situation in vivo, for some experimental designs it would be advantageous to apply a very localized chemical signal to cells, which in turn would yield a better understanding of the cytosolic signal-propagation characteristics. One approach for local cell stimulation is based on the use of chemokine-carrying beads that locally release signals when brought into contact with the cell. The position of the beads is controlled by electric or magnetic fields or by optical beams resulting in a high precision and high frequency possibility to challenge cellular response. Although this approach has been successfully applied and has become widely accessible, it adds a substantial complication to the experimental procedure.

In this current report we describe yet another approach which is based on an all-optical control of the receptor activity. We followed an optogenetic approach that has attracted much attention since the first demonstration of optical-switchable ion channels in 2003 (Nagel et al., 2003). Optogenetics is now used for targeted control of whole animals (Arenkiel et al., 2006). Through a combination of genetic targeting and optical stimulation the optogenetic approach provides a precise temporal and spatial control on the experimental system (Mattis et al., 2012). Optogenetics is currently emerging as a new, high-potential research field (Rein and Deussing, 2012; Tye and Deisseroth, 2012).

Here we developed a chimeric receptor, optoCXCR4, which was light-activated and allowed us to stimulate cellular response at high spatial and temporal resolution. Base to our chimeric receptor design is the

high structural similarity of the chemokine receptors with the comprehensively studied rhodopsin receptor. The basic concept for the design of our optoCXCR4 construct was the replacement of all intracellular parts of the rhodopsin receptor with those of the chemokine receptor CXCR4. This approach has been shown feasible earlier for the α_1- and β_2-adregeneric receptors (Airan et al., 2009). In this way receptor activation is analogous to that of rhodopsin, hence by light, whereas the intracellular signalling is controlled by the inner loops originating from the chemokine receptor of interest. The sequence design of various chimeric proteins is described in detail, followed by experiments for the characterization of their localization targeting properties and functionality. One of the chimeric receptors produced in the current study was shown to translocate successfully to the plasma membrane and display some functionality. Hence, we successfully applied an optogenetics approach to create a novel all-optical controlled chemokine receptor suitable for further biophysical studies. Whether the well-defined spatial and temporal activation of chemokine receptors in the studies of health and disease can be tackled by such optogenetic approach still has to be explored.

4.2 Materials and Methods

4.2.1 Cell culture

HEK (human embryonic kidney) 293 cells were cultivated in Dulbecco's Modified Eagle Medium (DMEM) (Sigma Life Science, USA) supplemented with 10% HyClone ™Fetal Bovine Serum (FBS, Thermo Scientific, USA), 1 mL penicillin/streptomycin (10 μg/mL antibiotics and 5 mL Glutamax™(Gibco, USA). Cells were cultured on 60 mm dishes. SH-SY5Y (human neuroblastoma) cells were cultivated in DMEM with Nutrient Mixture F-12 (DMEM/F12) supplemented with 10% FBS. Cells were cultured on T25 mattresses.

4.2.2 Sequences alignments

The protein sequence for bovine rhodopsin and CXCR4 were obtained using the Entrez databases of the National Center for Biotechnology Information (NCBI, USA). The sequence for opto-β_2AR was obtained from (Airan et al., 2009). Sequence alignments were performed using the BLAST algorithm (NCBI) or aligned manually.

4.2.3 Whole-plasmid cloning

The base-construct optoCXCR4 was modified at N- and C-terminus using a whole-plasmid cloning strategy. 20 ng of the base-construct DNA was mixed with 10 μM of forward and 10 μM of reverse primers, dNTPs, polymerase buffer, 20% DMSO and supplemented with MiliQ-water to a volume of 50 μL. Subsequently 0.25 μL of PfuX polymerase was added to run the PCR reaction. The entire plasmid was amplified in 25 cycles at a pace of 1.5 min/kB. The mixture was then incubated with 1 μL of DpnI for 1.5 hours to digest the base-construct DNA, followed by digestion with the relevant restriction enzyme (Supplemental Fig. S1 and S2) for 2 hours and ligation for 3 hours. Competent bacteria cells were transformed with the plasmid or its non-ligated analogue as control. Successful colonies were collected for amplification. DNA was purified using the DNA-purification kit following the manufacturers protocol and subsequently sequenced to check for correct sequence and/or point mutations (LGC Genomics or BaseClear).

4.2.4 Cell transfection

For experimental procedures $\sim 10^5$ cells were seeded in full medium on 35 mm dishes coated with ibiTreat (Ibidi, Germany) and incubated overnight prior to transfection. HEK 293 cells were transfected using specific ratios of FuGene HD (Promega Corporation, USA) or TurboFect (Thermo Scientific, USA) and the plasmid DNA, mixed in DMEM or OptiMEM (Life Technologies, USA). Before transfection, the medium was changed to 1 mL of corresponding serum-free medium. Then 100 μL transfection mixture was added. After the specified incubation time with the transfection mixture the medium was changed back to full medium. The cells were incubated overnight to allow for the protein expression. SH-SY5Y cells were transfected as described above, with the following modifications: the cell medium was changed to full medium approximately 6 hours before transfection, then transfection mixture was added. The cells were incubated overnight with the transfection mixtures. After incubation, the medium was changed to fresh DMEM/F12.

4.2.5 Microscopy

Imaging was performed on an Axiovert200 microscope (Zeiss, Germany) combined with a spinning disk unit (CSU-X1; Yokogawa, Japan) and

emCCD camera (iXon 897; Andor, UK). For illumination 514 (Cobolt) or 561 (Cobolt) nm lasers were used. Where indicated the CO_2 level was maintained at 5% and the temperature at 37°C using a microscopre-top unit (INUBG2E-ZILCS, TokaiHit, Japan).

4.2.6 Dual reporter activity assay

HEK 293 cells were co-transfected with the reporter element fused to the firefly luciferase (RE-*luc*), *Renilla* and one of the test sequences. We used a transfection mixture of plasmid DNA and Lipofectomine diluted separately in 12.5 μL of opti-MEM medium (Sigma Life Science, USA). Premixed components were incubated together for 20 minutes and added to the cells. After overnight incubation cells were supplemented with 100 nM of 9-cis retinal followed by 16 hours incubation. Cell activation was performed inside an incubator that was equipped with 502 nm LED illumination of uniform intensity of 200 μW/cm^2 for 6 hours. For the control (non-transfected sample) and for the sample transfected with CXCR4 (wt), activation was achieved by the addition of 100 nM of the CXCR4-specific ligand CXCL12. Subsequently the dual-luciferase detection was performed as described by the manufacturer. Briefly, cells were incubated for 15 min with luciferase assay reagent II (Promega) after which the luminescence signal was detected. Then, the cells were supplemented with Stop&Go®Reagent (Promega), which simultaneously quenches firefly luminescence and activates *Renilla* luciferase. After 15 min incubation *Renilla* luminescence was measured. The firefly luminescence was normalized to the luminescence of *Renilla*, in order to eliminate artefacts caused by, e.g. a difference in the number of cells in the sample. Further the average signals of activated samples was normalized to the average signal of non-activated samples. As negative control, samples transfected with RE-*luc* and *Renilla* only were used. All data are presented as mean of 2 to 5 independent experiments and the spread as standard deviation.

4.3 Design and characterization of an optoCXCR4 receptor

4.3.1 Design of optoCXCR4

Rhodopsin is the most extensively studied G-protein coupled receptor (GPCR). It was discovered in 1851 (Costanzi et al., 2009) and in 1970 identified as GPCR (Costanzi et al., 2009). In 1982 the receptor was sequenced (Costanzi et al., 2009) which revealed its 7-transmembrane (TM) topology. In 2000 rhodopsin was the first membrane protein for which the X-ray crystal structure was obtained (Palczewski et al., 2000).

Due to the sequence homology of the rhodopsin sub-family of GPCRs the resolved crystal structure of rhodopsin served as a base for the structure of other GPCRs of this family. The structure of a GPCR consists of three parts: (1) the extracellular, (2) the transmembrane and (3) the intracellular part (Fig. 4.1A). The extracellular part includes the N-terminus and three extracellular loops (EL1-EL3) together responsible for modulation of ligand access and ligand specificity. The transmembrane part consists of seven α-helices (TM1-TM7), forming the structural core of the receptor. The helices of the TM region are responsible for ligand recognition and signal transduction (Rajagopalan and Rajarathnam, 2006; Rosenkilde et al., 2000). The intracellular region includes intracellular loops (IL1-IL3), a small amphipathic helix (H8) and C-terminus. The intracellular parts determine downstream signalling via its G-protein binding sites on IL3 and the modulation of receptor activity on its C-terminal responsible for receptor downregulation and internalization (Venkatakrishnan et al., 2013). Thus, the TM region is thought of as communication link between the ligand-binding pocket and the G-protein-coupling region (Venkatakrishnan et al., 2013). The activation of the receptor results in its structural change. Multiple biochemical and biophysical studies suggested a common model of the TM helixes movements (Hoffmann et al., 2008; Venkatakrishnan et al., 2013; Wess et al., 2008). Mainly the TM helix 6 undergoes the largest movement (Hoffmann et al., 2008; Wess et al., 2008) inducing a rotational movement leading to a concomitant shift of the intracellular loop 3 (IL3) that controls the G-protein interaction and reorientation of its cytoplasmic end.

In contrast to all other GPCRs in which the ligand binds to the N-terminal part followed by interaction with the TM part, in rhodopsin

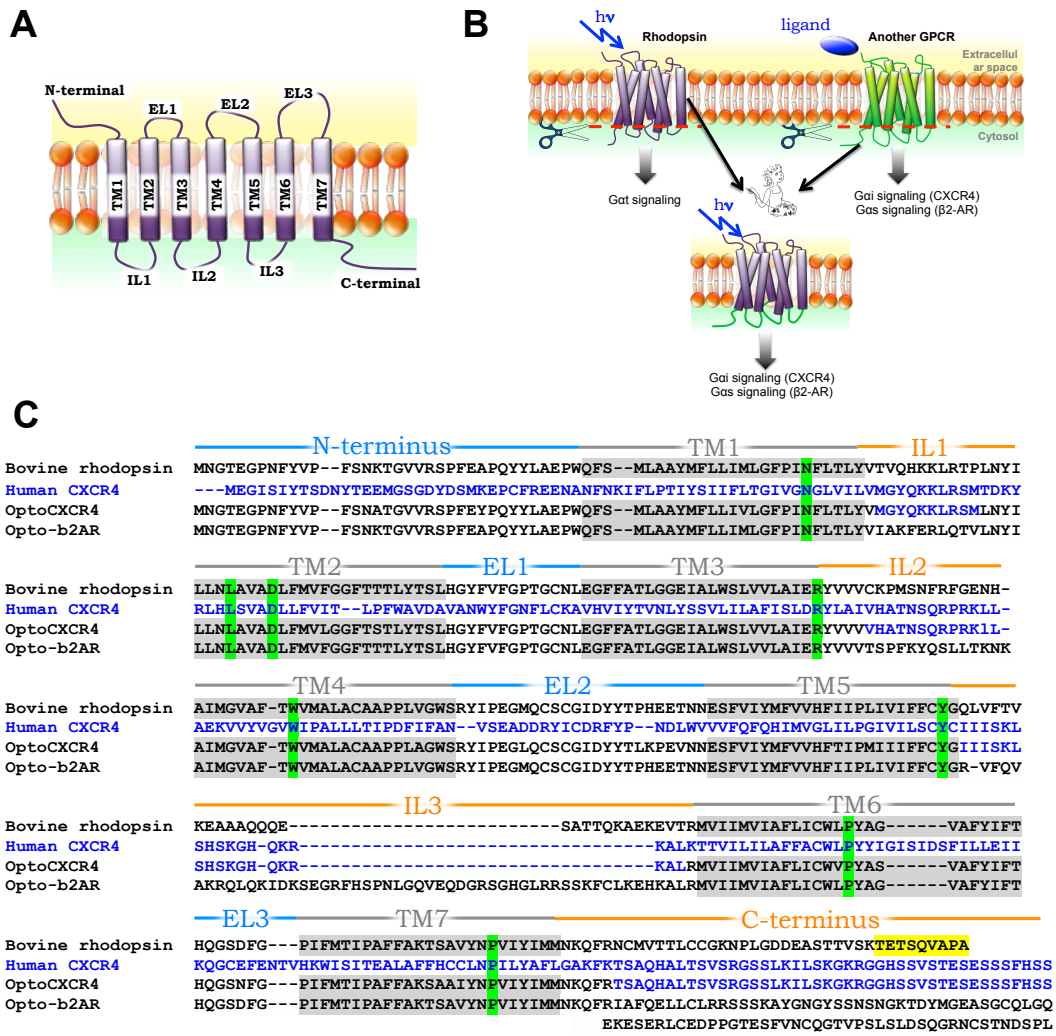

Figure 4.1
Design of the chimeric protein. ***A.*** *Schematic of the GPCR structure containing N-terminal, extracellular loops (EL1-EL3), transmembrane helixes (TM1-TM7), intracellular loops (IL1-IL3) and C-terminal.* ***B.*** *Schematic representation of the chimeric protein design. The IL of rhodopsin are exchanged with the IL of the GPCR of interest. The resulting chimeric receptor exhibit signalling of GPCR of interest when triggered by light activation (hν).* ***C.*** *Alignment of the bovine rhodopsin with human CXCR4 for construction of photo-activatable chimeric protein - optoCXCR4, compared to opto-β_2AR (Airan et al., 2009) .*

the ligand (retinal) is bound to the receptor though Lys_{296} (TM7) in the inactive state of the receptor. On light absorption an isomerization of retinal occurs and subsequently triggers a series of conformational changes including the rotation of TM6 leading to the G-protein activation (for review see Hofmann et al., 2009).

The high structural similarities of GPCRs including their activation scheme allowed the application of an optogenetic approach to GPCRs. It is assumed, that the precise output signal of the receptor is controlled primarily by the intracellular parts of the GPCR. Receptor activation, however, is controlled by the TM regions where the conformational change is translated into a structural change of the intracellular regions. The latter subsequently leads to the activation of G-protein dependent and independent pathways. In particular IL3 is responsible for signaling by G-proteins (either $G_{\alpha i/o}$, $G_{\alpha q/11}$, $G_{\alpha s}$ or $G_{\alpha 12/13}$ and $G_{\beta\gamma}$), while the C-terminal part of the GPCR is responsible for recognition of receptor kinases, which regulate a balanced receptor trafficking. Hence, a strategy was developed to exchange all intracellular parts and C-terminal of the rhodopsin receptor with that of another GPCR to produce a chimeric protein of particular functionality being controlled by light (Fig. 4.1B).

Kim et al. in 2005 demonstrated the feasibility of this approach with the first design of a functional all-optically activated GPCR (Kim et al., 2005). The group showed that exchange of the intracellular loops and the carboxyl (C)-terminal domain of rhodopsin with those of the β_2 adrenergic receptor ($\beta_2$2AR) results in a chimeric receptor, opto-β_2AR, which exhibited full β_2AR functionality but was light-activated. Further this chimeric-receptor approach has been demonstrated to be successful for creation of functional α_1-adregeneric receptor as well (Airan et al., 2009).

4.3.2 Cloning of various optoCXCR4 constructs

Here we designed various rhodopsin-CXCR4 chimeras following the strategy described by Kim et al. In the decision for the exact exchange positions of intracellular loops and C-terminus we were led by the alignment of the nucleotide sequence to that of rhodopsin and CXCR4, superposition of crystal structure of rhodopsin with recent crystal structure of the CXCR4 receptor (Wu et al., 2010), and by an earlier study (Xu et al., 2014). We used these findings to design an optically activated CXCR4 receptor - optoCXCR4.

A

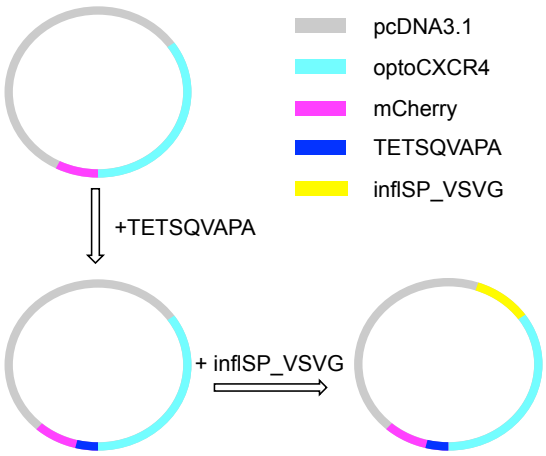

B

```
MHLDMNGTEGPNFYVPFSNKTGVVRSPFEAPQYYLAEPWQFSMLAAYMFLLIMLGFPINFLTLYVMGYQKKLRSMLNYILLNLAVADLFMVFGG
FTTTLYTSLHGYFVFGPTGCNLEGFFATLGGEIALWSLVVLAIERYVVVVHATNSQRPRKLLAIMGVAFTWVMALACAAPPLVGWSRYIPEGMQ
CSCGIDYYTPHEETNNESFVIYMFVVHFIIPLIVIFFCYGIIISKLSHSKGHQKRKALRMVIIMVIAFLICWLPYAGVAFYIFTHQGSDFGPIF
MTIPAFFAKTSAVYNPVIYIMMNKQFRTSAQHALTSVSRGSSLKILSKGKRGGHSSVSTESESSSFHSSTETSQVAPATGGSSGGSSGTVSKGE
EDNMAIIKEFMRFKVHMEGSVNGHEFEIEGEGEGRPYEGTQTAKLKVTKGGPLPFAWDILSPQFMYGSKAYVKHPADIPDYLKLSFPEGFKWER
VMNFEDGGVVTVTQDSSLQDGEFIYKVKLRGTNFPSDGPVMQKKTMGWEASSERMYPEDGALKGEIKQRLKLKDGGHYDAEVKTTYKAKKPVQL
PGAYNVNIKLDITSHNEDYTIVEQYERAEGRHSTGGMDELYK*
```

C

```
MKTIIALSYIFCLVFAMYTDIEMNRLGKDSLMNGTEGPNFYVPFSNKTGVVRSPFEAPQYYLAEPWQFSMLAAYMFLLIMLGFPINFLTLYVMG
YQKKLRSMLNYILLNLAVADLFMVFGGFTTTLYTSLHGYFVFGPTGCNLEGFFATLGGEIALWSLVVLAIERYVVVVHATNSQRPRKLLAIMGV
AFTWVMALACAAPPLVGWSRYIPEGMQCSCGIDYYTPHEETNNESFVIYMFVVHFIIPLIVIFFCYGIIISKLSHSKGHQKRKALRMVIIMVIA
FLICWLPYAGVAFYIFTHQGSDFGPIFMTIPAFFAKTSAVYNPVIYIMMNKQFRTSAQHALTSVSRGSSLKILSKGKRGGHSSVSTESESSSFH
SSRTQPVEICCTVSKGEEDNMAIIKEFMRFKVHMEGSVNGHEFEIEGEGEGRPYEGTQTAKLKVTKGGPLPFAWDILSPQFMYGSKAYVKHPAD
IPDYLKLSFPEGFKWERVMNFEDGGVVTVTQDSSLQDGEFIYKVKLRGTNFPSDGPVMQKKTMGWEASSERMYPEDGALKGEIKQRLKLKDGGH
YDAEVKTTYKAKKPVQLPGAYNVNIKLDITSHNEDYTIVEQYERAEGRHSTGGMDELYK*
```

```
MKTIIALSYIFCLVFAMYTDIEMNRLGKDSLMNGTEGPNFYVPFSNKTGVVRSPFEAPQYYLAEPWQFSMLAAYMFLLIMLGFPINFLTLYVMG
YQKKLRSMLNYILLNLAVADLFMVFGGFTTTLYTSLHGYFVFGPTGCNLEGFFATLGGEIALWSLVVLAIERYVVVVHATNSQRPRKLLAIMGV
AFTWVMALACAAPPLVGWSRYIPEGMQCSCGIDYYTPHEETNNESFVIYMFVVHFIIPLIVIFFCYGIIISKLSHSKGHQKRKALRMVIIMVIA
FLICWLPYAGVAFYIFTHQGSDFGPIFMTIPAFFAKTSAVYNPVIYIMMNKQFRTSAQHALTSVSRGSSLKILSKGKRGGHSSVSTESESSSIH
SSTETSQVAPATGGSSGGSSGTVSKGEEDNMAIIKEFMRFKVHMEGSVNGHEFEIEGEGEGRPYEGTQTAKLKVTKGGPLPFAWDILSPQFMYG
SKAYVKHPADIPDYLKLSFPEGFKWERVMNFEDGGVVTVTQDSSLQDGEFIYKVKLRGTNFPSDGPVMQKKTMGWEASSERMYPEDGALKGEIK
QRLKLKDGGHYDAEVKTTYKAKKPVQLPGAYNVNIKLDITSHNEDYTIVEQYERAEGRHSTGGMDELYK*
```

Figure 4.2
Design of enhanced optoCXCR4 plasmids. ***A.*** *Schematic representation of the addition of the C-terminus amino acids of rhodopsin -TETSQVAPA (dark blue), and the influenza SP - VSV g-epitope (yellow) to optoCXCR4-mCherry (light blue - pink).* ***B.*** *Amino-acid sequence of the final optoCXCR4-TETSQVAPA-mCherry plasmid.* ***C.*** *Amino-acid sequence of the final inflSP_VSVG-optoCXCR4-mCherry (top) and inflSP_VSVG-optoCXCR4-TETSQVAPA-mCherry (bottom) plasmids.*

In our base-design the intracellular loops and the C-terminus of the chimeric receptor were identical to those of human CXCR4, the rest was equal to that of rhodopsin (Fig. 4.2B,C). The rhodopsin intracellular loop IL1 (V_{61}-I_{75}) was replaced starting from T_{62} with IL1 of CXCR4 (M_{63}-M_{72}). Similarly, IL2 of rhodopsin (Y_{135}-H_{151}) was replaced starting from C_{139} with IL2 of CXCR4 (V_{139}-L_{151}). Rhodopsin-IL3 (Q_{224}-R_{251}) was completely replaced with IL3 of CXCR4 (I_{221}-L_{239}). Finally, the C-terminal part of rhodopsin was exchanged five amino acids after TM7 (N_{309}-R_{314}) with the C-terminal part of CXCR4 (T_{311}-S_{352}). Furthermore, at the C-terminus the construct was fused to either of the fluorescent proteins YFP or mCherry to enable visualization of the chimeric receptor. This base-design for an optoCXCR4 containing 355 amino acids was translated into a DNA sequence optimized for mammalian expression, synthesized (Genscript) and cloned into the pUC57 plasmid vector (Invitrogen). For further application we subsequently re-cloned the construct into the pcDNA3.1(+)-eYFP C1 vector.

Additionally to the base-construct we designed other constructs with modifications to the N- and C-terminus in order to putatively facilitate protein trafficking and assist proper protein targeting (Fig. 4.2).

To facilitate protein trafficking the last 9 amino-acids of the C-terminal domain of rhodopsin (TETSQVAPA) were added to the C-terminal of the base-construct. The QVS(A)PA amino-acid sequence is highly conserved for various opsins and shown to play an essential role in the formation of post-Golgi vesicles (Deretic, 1998; Deretic et al., 1998). Mutations in the C-terminal region of rhodopsin caused mislocalization of the protein (Deretic, 1998). To introduce the C-terminal sequence of rhodopsin (TETSQVAPA) a cloning technique based on PCR multiplication of the entire plasmid was used. We designed primers with homologous sequences to optoCXCR4-mCherry and the TETSQVAPA sequence as shown in the Supplementary Fig. S1. The whole-plasmid cloning procedure was performed as detailed in the Materials and Methods section. The final amino-acid sequence of optoCXCR4-TETSQVAPA-mCherry (further referred to as optoCXCR4-C9) is shown in Fig. 4.2B.

Further, we added a signalling peptide to the N-terminus of the base-construct to assist proper protein targeting towards the plasma membrane. It has been demonstrated that a N-terminal signalling peptide is required for receptor translocation across the endoplasmic reticulum (ER). GPCRs lacking this signalling peptide were retained in the ER

in a non-functional form (Kochl et al., 2002). As a N-terminal signalling motif we used an epitope of the vesicular stomatitis virus-G protein (VSVG) followed by the influenza A signalling peptide (inflSP). VSVG is a trans-membrane glycoprotein that contains a six amino acid signalling sequence facilitating efficient export of the protein from the endoplasmatic reticulum (ER). VSVG enhances viral envelope fusion with the plasma membrane (Roche et al., 2008). The six-residue epitope was shown to be sufficient for enhanced ER export (Sevier et al., 2000). For cloning the whole-plasmid strategy was used. Given that the inflSP-VSVG sequence was too long to be coded into one primer, a silent mutation was introduced in the middle of the sequence to create a restriction site (Supplementary Fig. S2). That allowed us to incorporate inflSP-VSVG in such a way, that one part was included in forward and the other in reverse primer. Using optoCXCR4-mCherry and optoCXCR4-TETSQVAPA-mCherry as base-construct DNA, we generated inflSP_VSVG-optoCXCR4-TETSQVAPA-mCherry and inflSP_VSVG-optoCXCR4-mCherry plasmids (further referred to as v-optoCXCR4-C9 and v-optoCXCR4, respectively) encoding the desired inflSP_VSVG sequence with or without the TETSQVAPA sequence (Fig. 4.2C).

In total five plasmids were created including the base-construct optoCXCR4: optoCXCR4-YFP, optoCXCR4-mCherry, optoCXCR4-C9, v-optoCXCR4 and, v-optoCXCR4-C9.

4.3.3 Optimization of cell transfection

Human embryonic kidney HEK 293 cells have a substantial endogenous expression of CXCR4. Thus, this cell line appeared as an appropriate system to follow optoCXCR4 signalling. We first optimized the transfection conditions for HEK 293 cells with the optoCXCR4 constructs using two different transfection reagents: FuGene and TurboFect. For transfections with FuGene 6 to 20 μL of reagent was mixed with 0.5-2 μg of plasmid DNA resulting in reagent:DNA ratios of 3:1, 6:1, 10:1 and 12:1. The incubation time with the FuGene-based transfection mixtures was kept at 3 hours. For transfections with TurboFect, 1-4 μL of the reagent were mixed with 1 μg of plasmid DNA resulting in reagent:DNA ratios of 1:1, 2:1 and 4:1. T he incubation time for TuboFect-based transfection mixtures ranged from 0.5-2 hours. We found that using 4 μL of TurboFect, 1 μg of DNA and 1.5 hours of incubation time led to optimal

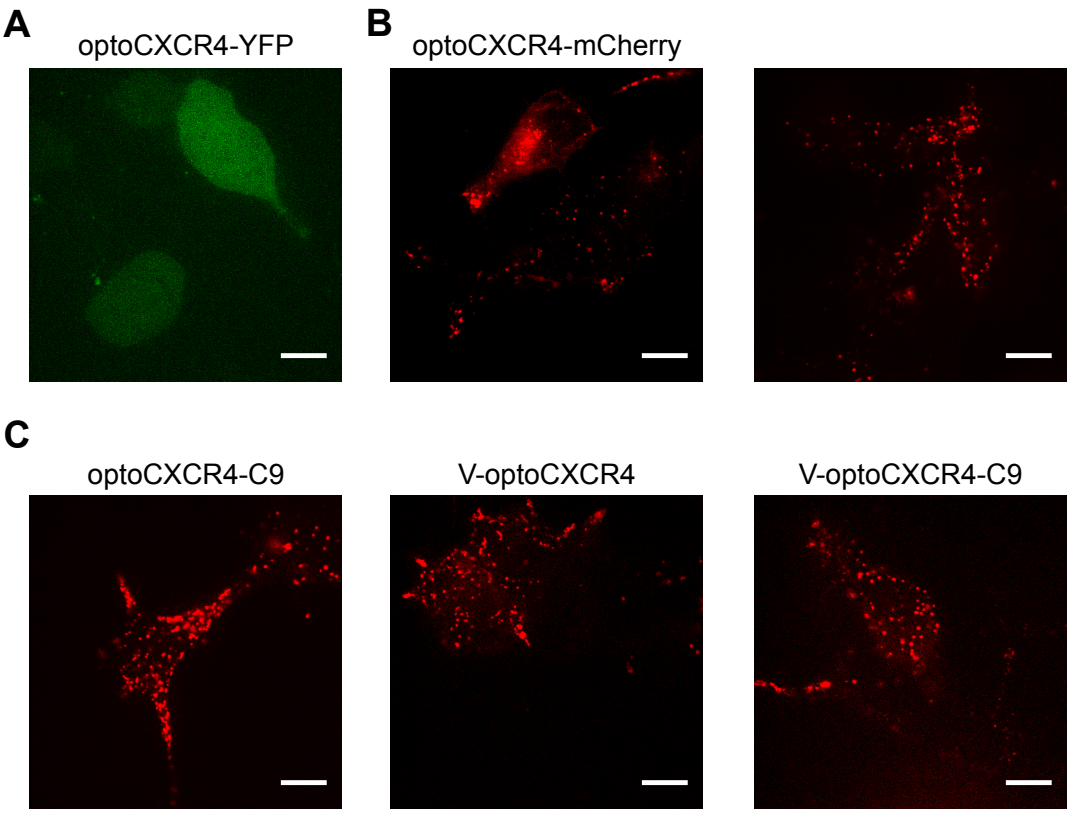

Figure 4.3
Transfection with optoCXCR4. ***A.*** *HEK 293 cells transfected with optoCXCR4-YFP using 1.5 hours of incubation with a transfection mixture containing 4 μL of TurboFect and 1 μg of DNA.* ***B.*** *HEK 293 cells transfected with optoCXCR4-mCherry using same transfection protocol after 1 (left) or 3 (right) days of expression.* ***C.*** *HEK 293 cells transfected with different variants of optoCXCR4-mCherry plasmid. Scale bar - 10 μm.*

transfection condition. the transfection efficiency was estimated from the percentage of fluorescent cells, 30-50% (data not shown). Hence, this transfection protocol was used for all further experiments on HEK 293 cells with optoCXCR4, if not indicated otherwise.

4.3.4 Localization of the chimeric receptors

To check the localization of the chimeric protein we performed fluorescence imaging on transfected HEK 293 cells. Imaging was done using spinning-disk confocal microscopy with 514 nm and 561 nm laser excitation for YFP- and mCherry-fused constructs, respectively. As shown in Figure 4.3 the chimeric proteins did not exhibit any pronounced

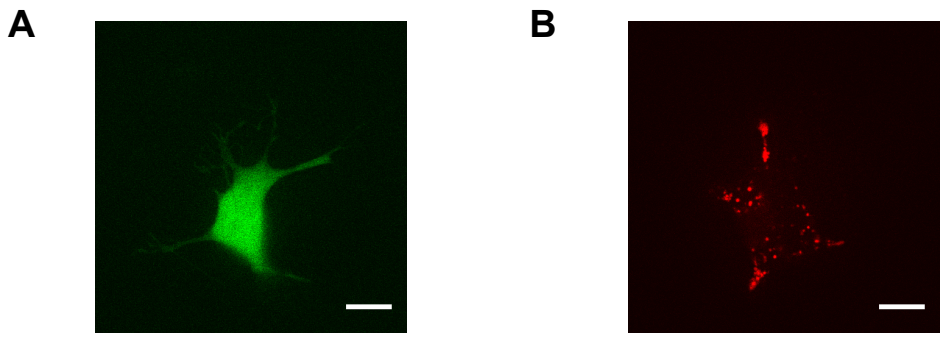

Figure 4.4
Localization of retinal-supplemented optoCXCR4-YFP. ***A.*** *SH-YSY5 cells transfected with optoCXCR4.* ***B.*** *HEK 293 cells transfected with optoCXCR4-mCherry plasmid after overnight incubation with 100 nM 9-cis retinal. Scale bar - 10 μm.*

plasma membrane localization. The fluorescent signals indicated that the optoCXCR4-YFP protein was uniformly distributed throughout the cell (Fig. 4.3A) and the optoCXCR4-mCherry protein presumably localized in vesicular structures (Fig. 4.3B, left). A longer incubation time after transfection did not change the localization of the optoCXCR4 constructs (Fig. 4.3B, right). Surprisingly, vesicular localization was observed for optoCXCR4-C9, v-optoCXCR4 and v-optoCXCR4-C9 constructs that were expected to exhibit enhanced plasma membrane targeting (Fig. 4.3C).

To avoid receptor activation during imaging the experiments described in Figure 4.3 were performed without addition of retinal, the rhodopsin ligand. Since it is unclear whether HEK 293 cells produced retinal endogenously, we questioned whether lack of the ligand might cause a disruption in the protein folding or protein targeting. Hence, we repeated the experiments in the neuroblastoma-derived cell line, SH-YSY5, which was shown to express both receptors CXCR4 and rhodopsin endogenously (Liberman et al., 2012; Saliba et al., 2002), and supposedly also produced the retinal. SH-YSY5 cells were transfected as described in Materials and Methods section. Confocal imaging of transfected SH-YSY5 cells was performed after overnight incubation. However, similar to our findings in HEK 293, optoCXCR4-YFP did not show any pronounced plasma membrane localization (Fig. 4.4A). Likewise, overnight incubation of HEK 293 cells with 100 nM of 9-cis retinal did not alter the localization of the chimeric receptor (Fig. 4.4B). Hence, the mislo-

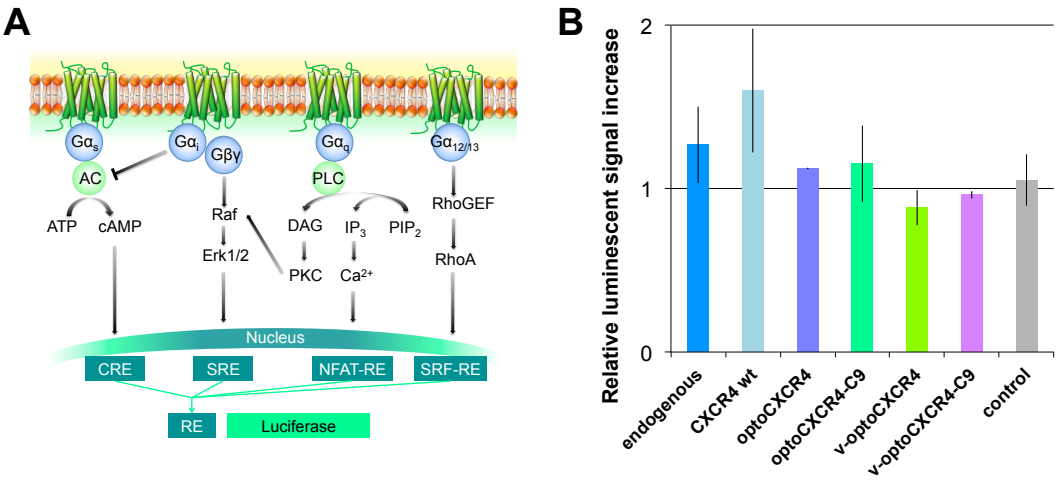

Figure 4.5
Luciferase assay. ***A.*** *Schematic representation of the luciferase assay adopted from Promega (Literature # TM040).* ***B.*** *Relative increase of the luciferase luminescence detected in HEK 293 cells for different constructs.*

calization of optoCXCR4 could not be attributed to the absence of the ligand.

Another potential reason for the mislocalization of the optoCXCX4 constructs could be due to receptor activation and initiation of the G-protein signalling cascade followed by a fast internalization of the receptor. Hence, the vesicular localization could potentially be attributed to the functionality of the receptor.

4.3.5 Functionality of the optoCXCR4 constructs

We tested the various optoCXCR4 constructs for functionality by analysing the G-protein activity using a dual-reporter luciferase assay (for details see Materials and Methods). HEK 293 cells were co-transfected with one of the optoCXCR4 constructs together with a reporter luciferase (Re-*luc*) and a *Renilla* luciferase construct. The Re-*luc* construct contains the firefly luciferase gene placed downstream of G-protein specific response elements (REs) (Fig. 4.5A). Stimulation of the receptor results in activation of a specific G-protein. In turn, the downstream biochemical cascade triggers the respective transcription factors that bind to the REs leading to luciferase expression. Luminescence of the *Renilla* luciferase was used to normalize the Re-*luc* luminescence for each sample.

For our experiments the $G_{\alpha i}/G_{\alpha 12}$-RE was used. Figure 4.5B shows the increase of relative luciferase luminescence for the various optoCXCR4 constructs after light stimulation. Cells transfected with the CXCR4 (wt) construct stimulated by 100 nM CXCL12 were used as a positive control. All data are presented as the relative change in the luciferase luminescence after stimulation with respect to the luciferase luminescence for non-stimulated cells. As negative control, light-activated cells transfected with Re-*luc* and *Renilla* but without any optoCXCR4 construct were used.

As expected, cells that contain either endogenous CXCR4 or that were transfected with a CXCR4 (wt) construct exhibited a relative luciferase luminescence increase of 1.2±0.2 and 1.6±0.4 after stimulation with CXCL12, respectively. Light activation of the optoCXCR4 and optoCXCR4-C9 constructs resulted in a relative luciferase increase of 1.1±0.1 and 1.2±0.2, respectively. The v-optoCXCR4 and v-optoCXCR4-C9 constructs exhibited a relative luminescence change of 0.9±0.1 and 1.0±0.1, respectively. Hence, within error-bars the activity of all optoCXCR4 constructs were not different to that of the negative control cells (1.1±0.2).

The negative results should not be taken as conclusive. In preparation of the dual-reporter assay cells were frequently exposed to light, which presumably leads to fast internalization of the chimeric receptors, and concomitantly to the inability to activate the G-protein pathways.

4.3.6 Fast optoCXCR4 internalization

Many GPCRs are known to undergo internalization upon continued activation. The internalization process in GPCRs is related to cellular adaptation, which allows cells to properly function in a wide concentration range of the ligand. We (Chapter 2 of this thesis), and others (Venkatesan, 2003) have reported that CXCR4 is efficiently internalized after stimulation with its natural ligand CXCL12.

Stimulation of rhodopsin by light is an extremely efficient process. The absorption of a single photon in the range between 400 and 600 nm suffices for receptor activation. In the experiments described above, we assumed that optoCXCR4 was inactive when it was not loaded with 9-cis retinal. However, any presence of retinal in the culture medium or plausible endogenous production of retinal in HEK 293 cells could not be completely excluded. Hence, we performed an experiment in complete dark-

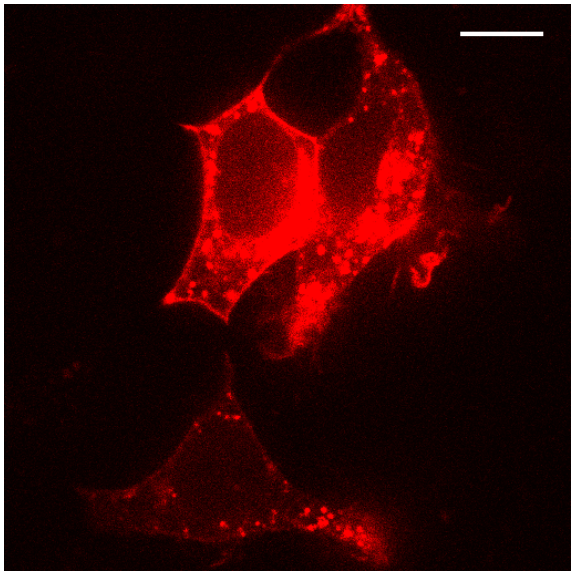

Figure 4.6
Transfection with optoCXCR4-mCherry. HEK 293 cells imaged 12 hours after transfection with optoCXCR4-mCherry plasmid. Extra precaution was taken to keep the cells in dark during the whole experimental procedure. Scale bar - 10 μm.

ness and limited the subsequent imaging time to 20 minutes. HEK 293 cells where transfected and incubated in a light-protected microscope-top incubator at 5% CO2 and 37°C (INCUBG2E-ZILS, Tokai Hit). After 12 hours the cells were imaged without additional steps. Following this transfection procedure resulted in localization of the optoCXCR4-mCherry largely at the plasma membrane (Fig. 4.6). This result implies that the cytosolic localization of the optoCXCR4 constructs in the earlier experiments was related to receptor internalization. Hence, the continued receptor stimulation during experiment preparation led to the receptor internalization and loss of the plasma membrane localization.

4.4 Conclusions

Here we described the construction of an all-optical controllable chemokine G-protein coupled receptor optoCXCR4. Inasmuch as the activation of rhodopsin is extremely fast and efficient, the optoCXCR4 protein was destined for internalization shortly after activation. A functional and correctly localized chimeric receptor was only observed when all preparatory steps were performed in complete darkness. A successful application of

optogenetic approach to GPCRs in cell-based or whole animal experiments have been shown by various groups. Nevertheless, it appears that further development is required to optimize this promising research tool for biophysical studies on GPCR dynamics at high special and temporal control. One way might be to make a design based on color opsins, which have a narrower excitation band, making imaging without receptor activation more feasible. Another way might include the use of bistable pigments. The bistable pigments can convert isomerized retinal into the pre-activated state: they contain an intrinsic bleach-recovery system and, thus, are capable of repeated activation of the receptor. (Bailes et al., 2012; Tsukamoto and Terakita, 2010)

4.5 Supplemental figures

Forward primer:

- Start point +AgeI +linker(GSSGGSSG) +**homologus part**
  - gatcaccggtggaagctctggcggatccagtggt**acagtgagcaagggcgagg**

Reverse primer:

- Start point + AgeI +TETSQAPA +**homologus part (reverse)**
  - gatcaccggtggcaggcgccacttggctggtttctgt**gctgctatgaaagctgctgc**

atgaacggcaccgaaggcccgaacttttatgtgccgtttagcaacaaaaccggcgtggtgcgcagcccgtttgaagcgccgcagtattatctgg
cggaaccgtggcagtttagcatgctggcggcgtatatgtttctgctgattatgctgggctttccgattaactttctgaccctgtatgtgatggg
ctatcagaaaaaactgcgcagcatgctgaactatattctgctgaacctggcggtggcggatctgtttatggtgtttggcggctttaccaccacc
ctgtataccagcctgcatggctattttgtgtttggcccgaccggctgcaacctggaaggctttttgcgaccctgggcggcgaaattgcgctgt
ggagcctggtggtgctggcgattgaacgctatgtggtggtggtgcatgcgaccaacagccagcgcccgcgcaaactgctggcgattatgggcgt
ggcgtttacctgggtgatggcgctggcgtgcgcggcgccgccgctggtgggctggagccgctatattccggaaggcatgcagtgcagctgcggc
attgattattataccccgcatgaagaaaccaacaacgaaagctttgtgatttatatgtttgtggtgcattttattattccgctgattgtgattt
ttttttgctatggcattattattagcaaactgagccatagcaaaggccatcagaaacgcaaagcgctgcgcatggtgattattatggtgattgc
gtttctgatttgctggctgccgtatgcgggcgtggcgttttatatttttacccatcagggcagcgattttggcccgatttttatgaccattccg
gcgtttttttgcgaaaaccagcgcggtgtataacccggtgatttatattatgatgaacaaacagtttcgcaccagcgcgcagcatgcgctgacca
gcgtgagccgcggcagcagcctgaaaattctgagcaaaggcaaacgcggcggccatagcagcgtgagcaccgaaa**gcgaaagcagcagctttca**
tagcagccgtacgcaaccggtcgagatctgctgt**acagtgagcaagggcgagg**aggataacatggccatcatcaaggagttcatgcgcttcaag
gtgcacatggagggctccgtgaacggccacgagttcgagatcgagggcgagggcgagggccgcccctacgagggcacccagaccgccaagctga
aggtgaccaagggtggcccccctgcccttcgcctgggacatcctgtcccctcagttcatgtacggctccaaggcctacgtgaagcaccccgccga
catccccgactacttgaagctgtccttccccgagggcttcaagtgggagcgcgtgatgaacttcgaggacggcggcgtggtgaccgtgacccag
gactcctccctccaggacggcgagttcatctacaaggtgaagctgcgcggcaccaacttcccctccgacggccccgtaatgcagaagaagacca
tgggctgggaggcctcctccgagcggatgtaccccgaggacggcgccctgaagggcgagatcaagcagaggctgaagctgaaggacggcggcca
ctacgacgctgaggtcaagaccacctacaaggccaagaagcccgtgcagctgcccggcgcctacaacgtcaacatcaagttggacatcacctcc
cacaacgaggactacaccatcgtggaacagtacgaacgcgccgagggccgccactccaccggcggcatggacgagctgtacaagtag

Figure S1
Design of primers for TETSQVAPA cloning. The forward primer contains a starting sequence, specific restriction enzyme AgeI (green), linker sequence and sequence homologues to the base-construct DNA. The reverse primer contains a starting sequence, specific restriction enzyme AgeI (green), TETSQAPA sequence and sequence homologues to the base-construct DNA. Start codon and spot codon are colored red, the sequence of CXCR4 highlighted in blue, the sequence of mCherry - in pink.

inflSP_VSV-Gepitope
accatgaagacgatcatcgccctgagctacatcttctgcctggtattcgccatgtacacc**GATATA**gagatgaacaggctgggaaaggatagcc
tc

point mutation to create silent **EcoRV** site
accatgaaaacgatcatcgccctgagctacatcttctgcctggtattcgccatgtacacc**GATATC**gagatgaacaggctgggaaaggatagcc
tc

Forward primer:

- Start point +**EcoRV** and part of inflSP_VSV-g-epitope +**homologos part**
  - gatc**GATATC**gagatgaacaggctgggaaaggatagcctc**atgaacggcaccgaaggc**

Reverse primer:

- start point +**EcoRV** and part of inflSP_VSV-g-epitope +**homologus part (reverse)**
  - gatc**GATATC**ggtgtacatggcgaataccaggcagaagatgtagctcagggcgatgatcgttttcatgg**taccaagcttaagtttaaa**

cgaaattaatacgactcactatagggagacccaagctggctagcg**tttaaacttaagcttggta**cctcgcgaatgcatctagat**atg**aacggca
ccgaaggccgaactttatgtgccgtttagcaacaaaaccggcgtggtgcgcagcccgtttgaagcgccgcagtattatctggcggaaccgtg
gcagtttagcatgctggcggcgtatatgtttctgctgattatgctgggctttccgattaactttctgaccctgtatgtgatgggctatcagaaa
aaactgcgcagcatgctgaactatattctgctgaacctggcggtggcggatctgtttatggtgtttggcggctttaccaccaccctgtatacca
gcctgcatggctattttgtgtttggcccgaccggctgcaacctggaaggctttttgcgaccctgggcggcgaaattgcgctgtggagcctggt
ggtgctggcgattgaacgctatgtggtggtggtgcatgcgaccaacagccagcgcccgcgcaaactgctggcgattatgggcgtggcgtttacc
tgggtgatggcgctggcgtgcgcggcgccgccgctggtgggctggagccgctatattccggaaggcatgcagtgcagctgcggcattgattatt
ataccccgcatgaagaaaccaacaacgaaagctttgtgatttatatgtttgtggtgcattttattattccgctgattgtgatttttttttgcta
tggcattattattagcaaactgagccatagcaaaggccatcagaaacgcaaagcgctgcgcatggtgattattatggtgattgcgtttctgatt
tgctggctgccgtatgcgggcgtggcgttttatatttttacccatcagggcagcgattttggcccgatttttatgaccattccggcgtttttg
cgaaaaccagcgcggtgtataacccggtgatttatattatgatgaacaaacagtttcgcaccagcgcgcagcatgcgctgaccagcgtgagccg
cggcagcagcctgaaaattctgagcaaaggcaaacgcggcggccatagcagcgtgagcaccgaaagcgaaagcagcagctttcatagcagccgt
acgcaaccggtcgagatctgctgtacagtgagcaagggcgaggaggataacatggccatcatcaaggagttcatgcgcttcaaggtgcacatgg
agggctccgtgaacggccacgagttcgagatcgagggcgagggcgagggccgcccctacgagggcacccagaccgccaagctgaaggtgaccaa
gggtggcccccctgcccttcgcctgggacatcctgtcccctcagttcatgtacggctccaaggcctacgtgaagcaccccgccgacatccccgac
tacttgaagctgtccttccccgagggcttcaagtgggagcgcgtgatgaacttcgaggacggcggcgtggtgaccgtgacccaggactcctccc
tccaggacggcgagttcatctacaaggtgaagctgcgcggcaccaacttcccctccgacggccccgtaatgcagaagaagaccatgggctggga
ggcctcctccgagcggatgtaccccgaggacggcgccctgaagggcgagatcaagcagaggctgaagctgaaggacggcggccactacgacgct
gaggtcaagaccacctacaaggccaagaagcccgtgcagctgcccggcgcctacaacgtcaacatcaagttggacatcacctcccacaacgagg
actacaccatcgtggaacagtacgaacgcgccgagggccgccactccaccggcggcatggacgagctgtacaag**tag**

Figure S2

Design of primers for inflSP_ VSVG cloning. A silent mutation is inserted at GATATA sequence. The forward primer contains a starting sequence, specific restriction enzyme EcoRV (green), part of inflSP_ VSVG (yellow) and sequence homologues to the base-construct DNA. The reverse primer contains a starting sequence, specific restriction enzyme EcoRV (green), second part of inflSP_ VSVG (yellow) and sequence homologues to the base-construct DNA. Start codon and spot codon are colored red, the sequence of CXCR4 highlighted in blue, the sequence of mCherry - in pink.

4.6 Acknowlegement

We thank Harald Janovjak for valuable comments and discussion. Additionally we thank the Janovjak Lab for the opportunity to perform part of the cloning and analysis experiments at the IST in Vienna.

4.7 References

Airan, R.D., Thompson, K.R., Fenno, L.E., Bernstein, H., and Deisseroth, K. (2009). Temporally precise in vivo control of intracellular signalling. Nature 458, 1025-1029.

Arenkiel, B., Peca, J., Davison, I., Feliciano, C., Deisseroth, K., Augustine, G., Ehlers, M., and Feng, G. (2006). In Vivo Light-Induced Activation of Neural Circuitry in Transgenic Mice Expressing Channelrhodopsin-2. Neuron.

Bailes, H.J., Zhuang, L.-Y.Y., and Lucas, R.J. (2012). Reproducible and sustained regulation of Gas signalling using a metazoan opsin as an optogenetic tool. PLoS ONE 7, e30774.

Costanzi, S., Siegel, J., Tikhonova, I.G., and Jacobson, K.A. (2009). Rhodopsin and the others: a historical perspective on structural studies of G protein-coupled receptors. Curr. Pharm. Des. 15, 3994-4002.

Deretic, D. (1998). Post-Golgi trafficking of rhodopsin in retinal photoreceptors. Eye (Lond) 12 (Pt 3b), 526-530.

Deretic, D., Schmerl, S., Hargrave, P.A., Arendt, A., and McDowell, J.H. (1998). Regulation of sorting and post-Golgi trafficking of rhodopsin by its C-terminal sequence QVS(A)PA. Proc. Natl. Acad. Sci. U.S.A. 95, 10620-10625.

Fredriksson, R., Lagerstrom, M.C., Lundin, L.-G.G., and Schioth, H.B. (2003). The G-protein-coupled receptors in the human genome form five main families. Phylogenetic analysis, paralogon groups, and fingerprints. Mol. Pharmacol. 63, 1256-1272.

Hoffmann, C., Zurn, A., Bunemann, M., and Lohse, M.J. (2008). Conformational changes in G-protein-coupled receptors-the quest for functionally selective conformations is open. Br. J. Pharmacol. 153 Suppl 1, S358-66.

Hofmann, K., Scheerer, P., Hildebrand, P., Choe, H.-W., Park, J., Heck, M., and Ernst, O. (2009). A G protein-coupled receptor at work: the rhodopsin model. Trends in Biochemical Sciences.

Kim, J.-M.M., Hwa, J., Garriga, P., Reeves, P.J., RajBhandary, U.L., and Khorana, H.G. (2005). Light-driven activation of beta 2-adrenergic receptor signaling by a chimeric rhodopsin containing the beta 2-adrenergic receptor cytoplasmic loops. Biochemistry 44, 2284-2292.

Kochl, R., Alken, M., Rutz, C., Krause, G., Oksche, A., Rosenthal, W., and Schulein, R. (2002). The signal peptide of the G protein-coupled human endothelin B receptor is necessary for translocation of

the N-terminal tail across the endoplasmic reticulum membrane. J. Biol. Chem. 277, 16131-16138.

Liberman, J., Sartelet, H., Flahaut, M., Muhlethaler-Mottet, A., Coulon, A., Nyalendo, C., Vassal, G., Joseph, J.-M.M., and Gross, N. (2012). Involvement of the CXCR7/CXCR4/CXCL12 axis in the malignant progression of human neuroblastoma. PLoS ONE 7, e43665.

Mattis, J., Tye, K.M., Ferenczi, E.A., Ramakrishnan, C., O'Shea, D.J., Prakash, R., Gunaydin, L.A., Hyun, M., Fenno, L.E., Gradinaru, V., et al. (2012). Principles for applying optogenetic tools derived from direct comparative analysis of microbial opsins. Nat. Methods 9, 159-172.

Nagel, G., Szellas, T., Huhn, W., Kateriya, S., Adeishvili, N., Berthold, P., Ollig, D., Hegemann, P., and Bamberg, E. (2003). Channelrhodopsin-2, a directly light-gated cation-selective membrane channel. Proc. Natl. Acad. Sci. U.S.A. 100, 13940-13945.

Palczewski, K., Kumasaka, T., Hori, T., Behnke, C., Motoshima, H., Fox, B., Trong, I., Teller, D., Okada, T., Stenkamp, R., et al. (2000). Crystal Structure of Rhodopsin: A G Protein-Coupled Receptor. Science.

Rajagopalan, L., and Rajarathnam, K. (2006). Structural basis of chemokine receptor function–a model for binding affinity and ligand selectivity. Biosci. Rep. 26, 325-339.

Rein, M.L., and Deussing, J.M. (2012). The optogenetic (r)evolution. Mol. Genet. Genomics 287, 95-109.

Roche, S., Albertini, A.A., Lepault, J., Bressanelli, S., and Gaudin, Y. (2008). Structures of vesicular stomatitis virus glycoprotein: membrane fusion revisited. Cell. Mol. Life Sci. 65, 1716-1728.

Rosenkilde, M.M., Kledal, T.N., Holst, P.J., and Schwartz, T.W. (2000). Selective elimination of high constitutive activity or chemokine binding in the human herpesvirus 8 encoded seven transmembrane oncogene ORF74. J. Biol. Chem. 275, 26309-26315.

Saliba, R.S., Munro, P.M., Luthert, P.J., and Cheetham, M.E. (2002). The cellular fate of mutant rhodopsin: quality control, degradation and aggresome formation. J. Cell. Sci. 115, 2907-2918.

Sevier, C.S., Weisz, O.A., Davis, M., and Machamer, C.E. (2000). Efficient export of the vesicular stomatitis virus G protein from the endoplasmic reticulum requires a signal in the cytoplasmic tail that includes both tyrosine-based and di-acidic motifs. Mol. Biol. Cell 11, 13-22.

Tsukamoto, H., and Terakita, A. (2010). Diversity and functional properties of bistable pigments. Photochem. Photobiol. Sci.

Tye, K.M., and Deisseroth, K. (2012). Optogenetic investigation of neural circuits underlying brain disease in animal models. Nat. Rev. Neurosci. 13, 251-266.

Venkatakrishnan, A.J., Deupi, X., Lebon, G., Tate, C.G., Schertler, G.F., and Babu, M.M. (2013). Molecular signatures of G-protein-coupled receptors. Nature 494, 185-194.

Venkatesan (2003). Distinct Mechanisms of Agonist-induced Endocytosis for Human Chemokine Receptors CCR5 and CXCR4. Molecular Biology of the Cell.

Wess, J., Han, S.-J.J., Kim, S.-K.K., Jacobson, K.A., and Li, J.H. (2008). Conformational changes involved in G-protein-coupled-receptor activation. Trends Pharmacol. Sci. 29, 616-625.

Wu, B., Chien, E.Y., Mol, C.D., Fenalti, G., Liu, W., Katritch, V., Abagyan, R., Brooun, A., Wells, P., Bi, F.C., et al. (2010). Structures of the CXCR4 chemokine GPCR with small-molecule and cyclic peptide antagonists. Science 330, 1066-1071.

Xu, Y., Hyun, Y.-M.M., Lim, K., Lee, H., Cummings, R.J., Gerber, S.A., Bae, S., Cho, T.Y., Lord, E.M., and Kim, M. (2014). Optogenetic control of chemokine receptor signal and T-cell migration. Proc. Natl. Acad. Sci. U.S.A. 111, 6371-6376.

Chapter 5

The mechanical phenotype of Ewing sarcoma cell lines predicts their metastatic niche[1]

[1]This chapter is based on: E. Beletkaia, O. Iendaltseva, H. E. Balcioglu, P. C.W. Hogendoorn, E. H.J. Danen, T. Schmidt, The mechanical phenotype of Ewing sarcoma cell lines predicts their metastatic niche *(in preparation)*

Ewing sarcoma develops mostly in bone and lest often in the somatic soft tissues and their primary site of metastasis are the lungs. Thus, the mechanical micro-environment of the primary tumor and that of the metastasis site is drastically different. The stiffness of the lungs (∼2 kPa) is about 50 times lower as compared to the stiffness of bone tissue (100 kPa). It was shown earlier that the expression of the Ewing sarcoma-defining chimeric protein EWS/FLI has a dramatic effect on the cellular architecture, the development of actin stress fibers, and the formation of cell-matrix adhesions. Here we address the question whether distinct responses to mechanical cues may impact guidance of Ewing sarcoma cells towards their site of metastasis. We show that Ewing sarcoma cells have a preference to soft substrates in two- and three-dimensional assays. In soft 3D gels cells exhibit an elevated migratory phenotype together with a more spread morphology, and on softer 2D surfaces an enhanced formation of stress fibers and cell-matrix adhesions. Our data suggest that the mechanical phenotype of Ewing sarcoma cells is micro-environment dependent and may impact on the metastatic profile of Ewing sarcoma.

5.1 Introduction

Ewing sarcoma (ES) is a highly malignant tumor affecting predominantly children and young adults. ES belongs to a family of small-blue-round-cell tumors. It develops within bone and at later age sometimes in soft tissues, with lungs as the primary site of metastasis. Genetically ES is defined by a chromosomal translocation t(11;22)(q24;q12) (Kovar, 2005; Sand et al., 2015). This translocation leads to fusion of a portion of the EWS gene to the transcription factor-like gene EST, mostly FLI1 (Kovar, 2005). The resulting EWS/FLI chimeric protein has no described putative enzymatic activity (Erkizan et al., 2010). EWS/FLI acts as transcriptional factor (Kovar, 2005) causing changes in the expression of multiple genes including the chemokine receptor 4 (CXCR4) (Bennani-Baiti et al., 2010). It is believed that up-regulation of CXCR4 is a hallmark in alteration of cell behavior and potentially promotes ES metastasis. Overexpression of CXCR4 leads to enhanced directional cell migration towards the sites of tissue where it's chemokine ligand CXCL12 (stromal-derived factor 1, SDF-1) is expressed. However, in terms of tumor migration it appears unlikely that the metastatic niche of ES is solely dependent on CXCL12 given that most ES metastasis locates to the lungs but not other highly CXCL12-expressing tissues.

It has been shown that the chimeric protein EWS/FLI further modulates the expression of genes that regulate the cytoskeleton. Cells affected by the EWS/FLI expression exhibit a dramatic change in their cellular architecture. EWS/FLI reduces expression of zyxin and α_5 integrin which together leads to a loss of organized actin stress fibers and focal adhesions, to a reduction of cell spreading, to an inhibition of cell migration, and to an enhanced growth-rate (Chaturvedi et al., 2012, 2014). Moreover, expression of EWS/FLI causes a downregulation of haptotactic cell migration in a Boyden chamber assay (Chaturvedi et al., 2012). Knock-down of EWS/FLI as well as re-expression of zyxin and α_5 integrin results in a partial recovery of the phenotype including a drastic increase in cell adherence, and an increase in cell migration (Chaturvedi et al., 2012, 2014). Hence, it appears likely that the EWS/FLI translocation in Ewing sarcoma leads, next to a chemotactic phenotype with high CXCL12 sensitivity, to an altered mechanical phenotype that affects cell adhesion, migration and more general cell mechanics.

Lately it has been demonstrated that the mechanical properties of the cellular micro-environment, like its stiffness, can alter cellular behavior.

Changes in micro-environment stiffness can alter cell growth, proliferation and spreading (Engler et al., 2006; Mierke, 2013; Park et al., 2011; Paszek et al., 2005; Schrader et al., 2011; Wolf et al., 2013). Similarly, in tumor environment variation of the physiological stiffness play a key role in cancer cell migration (Liou et al., 2014; Mierke, 2013; Chaudhuri et al., 2014) as well as chemotherapeutic response (Schrader et al., 2011). Hence, research on mechanics of the tumor micro-envieronment and tumor cells' mechanosensing could lead to emerging of novel cancer treatment strategies.

In the current study we address the relation between mechanical phenotypes and metastatic profiles of Ewing sarcoma cells. For this study we chose two Ewing sarcoma cell lines, 6647 and CHP100, which display largely disparate metastatic behavior including their final metastatic niche in lung and bone, respectively. We show that these two cell lines exhibit markedly different mechanical phenotypes (spreading, migration and force application) both in two- and three-dimensional assays. A soft microenvironment induced an enhanced formation of stress fibers and cell-matrix adhesions for 6647 cells, but not for CHP100 cells. Unlike 6647 cells, CHP100 cells displayed a mechanical phenotype which induce cellular forces with increased matrix stiffness. We were further surprised to find that the activation of the CXCR4 receptor by its ligand CXCL12 did not alter the phenotype or the mechanical response in either of the cell lines. Our results suggest, that the mechanical properties of the microenvironment are one of the key cues that dictate the choice of metastasis site for Ewing sarcoma cells, while CXCL12 does not alter the effect.

5.2 Materials and Methods

5.2.1 Cell culture and viral transfection

6647 (generously granted by T.J. Triche Lab) and CHP100 (EurBoNET consortium collection (Ottaviano et al., 2010)) cells were maintained in IMDM cell culture medium (Gibco, USA) supplemented with 10% fetal bovine serum (FBS, Gibco, USA) at 37°C and 5% CO_2.

Where indicated, 6647 cells were transduced using a lentiviral mCherry-LifeAct cDNA expression vector (provided by Olivier Pertz, University of Basel, Switzerland) for visualization of the actin cytoskeleton. Cell selection was performed in a culture medium containing 2

μg/mL puromycin (Acros Organics/Fisher).

5.2.2 Collagen gel assay

Collagen 3D migration experiments were performed and analysed as described elsewhere (Balcioglu et al., 2015; Fig. 5.2A). Briefly, collagen isolated from rat tails using acid extraction was diluted to final working concentration in culture medium containing 0.1M Hepes and fixed to pH 7.5 by addition of NaHCO3. 60 μL of this solution was then pipetted into a glass bottom 96-well plate (Greiner) and incubated 72 hours at 4°C, or for 1 hour at 37°C to polymerize. Subsequently, an automated microinjector (Life Science Methods BV, Leiden, Netherlands) was used to inject 3 spheroids of 60-75 μm radius, at 200 μm above the glass bottom with an inter-spheroid distance of ∼3.5 mm. Where indicated 100 nM CXCL12 was added to the medium after the injections. Spheroids were imaged using a Nikon TE2000 confocal microscope equipped with a Prior stage controlled by NIS Element Software (Nikon) and a temperature and CO_2-controlled incubator. Differential interference contrast (DIC) images were captured with a CCD-camera. In house written Matlab (Mathworks, Natick, MA, USA) scripts were used to perform image analysis. Isolation of the injection core was achieved by intensity thresholding. Canny edge detection was used to extract the injection outline and single cells. Spheroid radius was calculated from the combined image of injection core and injection outline. For single cell analysis, binary image obtained by canny-edge filtering was watersheded to separate cell clusters. Areas larger than 200 μm^2 were considered as individual cells. Due to irregular shape some cells were not included with such size thresholding. For those a convex hull filter was applied to areas smaller than 200 μm^2. The areas exhibiting sizes larger than 200 μm^2 after convex hull filtering were also included in the single-cells analysis. In single-cell analysis the distance of each cell to the injection border was calculated by subtracting the spheroid radius at day 0 from the distance of the cell center to the injection center.

5.2.3 Micropillar preparation

Poly(dimethylsiloxane) (PDMS) micropillar arrays were prepared as described before (van Hoorn et al., 2014). Briefly, silicon wafers (Bonda thechnology PTE LDT) with a hexagonal-ordered negative pattern of 2

micropillar height (μm)	Effective array stiffness (kPa)
3.2	137.1
4.1	47.2
10	7.5

Table 5.1
Effective stiffness of the micropillar array surfaces of different hight

μm diameter holes and 2 μm spacing were used. PDMS (Sylgard 184, Dow Corning) was mixed in a 10:1 ratio of base to crosslinker. The mixture was degassed for 1 hour, poured over the master wafers and baked at 110°C for 20 hours. This preparation resulted in an elastomer of 2.5±0.1 MPa bulk stiffness (van Hoorn et al., 2014). The depth of the wafer holes set the final height of the micropillars, and hence the micropillar spring constant, and the effective stiffness of the micropillar array surface (Table 5.1). Micromicropillar arrays were flanked by 50 μm spacers to enable upside-down imaging with a high-resolution microscope.

The top of the micropillar arrays were subsequently stamped with fluorescencently-labeled fibronectin using micro-contact printing. A mixture of 10 μg/mL Alexa 647 or 405 NHS-labeled fibronectin and 50 μg/mL non-labelad fibronectin (Sigma) was used. To prevent aspecific binding, the micropillar surface was blocked with 0.2% pluronic F127 (Sigma) in phosphate buffered saline (PBS) for at least 30 minutes.

5.2.4 Microscopy

Brightfield microscopy and confocal imaging was performed as described by van Hoorn et al. (van Hoorn et al., 2014). Briefly, images were acquired using an Axiovert200 microscope (Zeiss, Germany) combined with a spinning disk unit (CSU-X1, Yokogawa, Japan) and an emCCD camera (iXon 897, Andor, UK). Imaging control and data acquisition was achieved in IQ-software (Andor, UK). For illumination 405 nm (CrystalLaser), 514 nm (Cobolt), 561 nm (Cobolt) and 642 nm (SpectraPhysics) lasers were used.

During imaging of live samples the CO_2 level was maintained at 5% and the temperature at 37°C using an INUBG2E-ZILCS unit (TokaiHit, Japan). Where indicated, 100 nM CXCL12 was added to cells 10 minutes prior to imaging.

5.2.5 Force detection

Detection of micropillar deflections and following forces analysis was performed using algorithms written in MatLab (Mathworks Inc., USA) as described elsewhere (van Hoorn et al., 2014). Briefly, positions of the micropillar tops were detected with a ∼30 nm accuracy using fluorescent images acquired at 642 or 405 nm excitation. Micropillar deflections were extracted by referencing to a perfect hexagonal grid. Forces were analyzed for 300-900 micropillars per condition. Force-distributions were calculated and subsequently analyzed in terms of their most probable value and a standard error for the latter (Supplementary Fig. S4B).

5.2.6 Immunostaining

After overnight incubation on micropillars, cells were fixed with 4% PFA in PBS for 15 min, and permeabilized using 0.1% TritonX in PBS. Subsequently, cells were blocked with 1% BSA (Sigma, USA) for 1 hour. Paxillin was detected using a monoclonal mouse-anti-human antibody against paxillin (Invitrogen) and an Alexa405-labeled goat-anti-mouse IgG antibody (Life Technologies). Actin staining was performed using phalloidin conjugated to Alexa532 (Invitrogen).

5.2.7 Cell area detection

Cell area was determined using built-in 'measurments' plugins of FIJI software. The cell edge was determined after background subtraction and thresholding, followed by the tracing tool in FIJI. The results are reported as mean±sem from 20-130 cells per condition.

5.2.8 2D migration rate detection

The 2D migration rate detection was acquired from brightfield images of the cels. In each frame the center of mass of a cell was detected. From acquired traces (Fig. 1E) mean square displacement of the cells was calculated. Fit to a diffusion model (MSD=4Dt) yielded in $D_{migration}$.

5.3 Results

5.3.1 Cell phenotype depends on substrate modification

We investigated the Ewing sarcoma (ES) derived cell lines 6647 and CHP100. Both cell lines were established in early 1970's and later identified as Ewing sarcoma by characteristic reciprocal translocation t(11;22)(q24;q12) (Giovannini et al., 1994; Whang-Peng et al., 1986). The 6647 cell line, established from a biopsy of a tumor that developed in the femur, represents a prototypical Ewing sarcoma phenotype that metastasizes into the lungs. In comparison, the metastatic niche of the CHP100 cell line, which was derived from an epidural tumor surrounding the spine, was bone (Schlesinger et al., 1976). Many ES cells, like 6647, prefer to grow in tight connection forming spheroids in suspension (Landuzzi et al., 2000). This was confirmed with our observations; 6647 cells formed spheroids that were stable and span a range of sizes, 20-150 μm in diameter containing 25-50000 cells. Cells mainly resided in suspension with weak attachment to plastic substrates (Fig. 5.1A).

The suspension-phenotype of 6647 cells dramatically changed on the dishes coated with extracellular matrix (ECM) proteins. When plated on dishes, which were pre-coated with 0.1% gelatin (mainly collagen I), 6647 cells firmly adhered within a few hours. Individual cells spread out of the spheroids over time invading the surface within 24 hours (Fig. 5.1B). Cells that moved out of the spheroid exhibited a stretched, fibroblast-like, morphology (Fig. 5.1B inset). Spread cells did not form new spheroids. A similar behavior was observed for 6647 cells on surfaces coated with 10 μg/ml fibronectin (Fig. S1).

In contrast to 6647 cells, as was shown previously (Bernal et al., 1983; Schlesinger et al., 1976) CHP100 cells grew as individual cells, independent of the surface modifications (Fig. 5.1C,D). Cells did not show any morphological differences while plated on plastic (Fig. 5.1C), or on dishes coated with gelatin (Fig. 5.1D). Cells did not form spheroids, neither in suspension nor on a surface. Individual cells firmly adhered to surfaces and displayed a spread morphology (Fig. 5.1C, inset). Notably, CHP100 cells did not exhibit any active migratory behavior ($D_{migration}$ = 75±2 $\mu m^2/h$; Fig. 5.1E,F) within the 24 hours observation time.

These results showed that addition of ECM dramatically changes morphology of the 6647 cells and their migratory abilities, while for the CHP100 cells the presence of ECM did not have any influence. Hence,

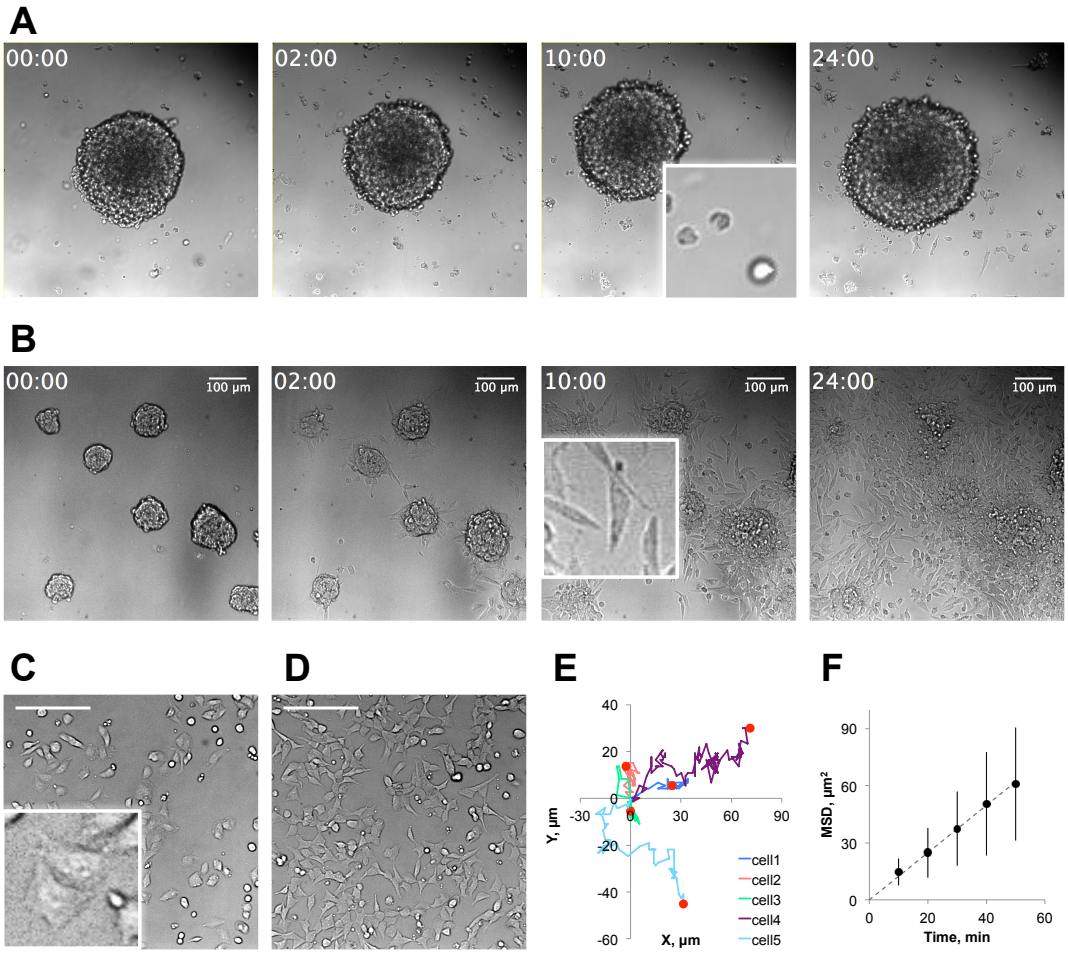

Figure 5.1

Ewing sarcoma cells growing at different conditions. 6647 cells growing on the plastic petri dish ***(A)*** *coated with gelatin/collagen I* ***(B)*** *followed for 24 hours after plating. CHP100 cells growing on the plastic petri dish* ***(C)*** *pre-treated with gelatin/collagen I* ***(D)*** *imaged after overnight incubation. Scale bar - 100 µm; time shown in hours; inserts - 8 times zoom in.* ***E.*** *Migratory tracks of individual CHP100 cells.* ***F.*** *Change of mean square displacement in time determined from shift of the center of mass of individual cells.*

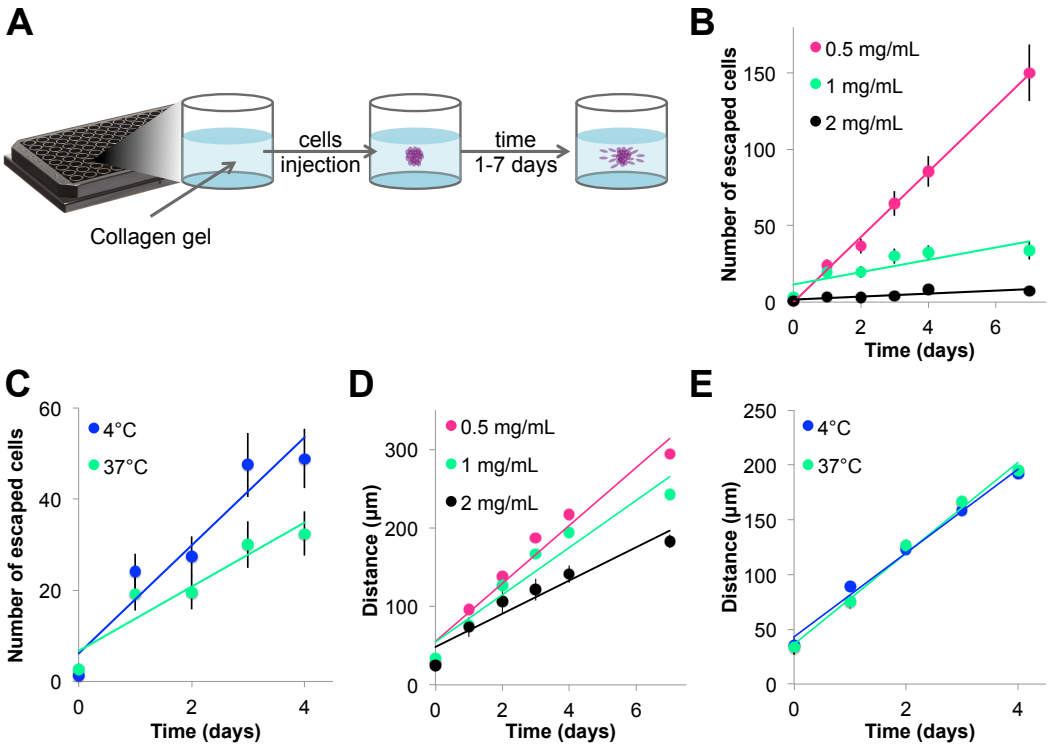

Figure 5.2
Microinjection of 6647 cells. ***A.*** *Experiment scheme. Scale bar - 50 µm. Comparison of number of the cells escaped from the spheroid* ***(B and C)*** *and the average distance migrated by individual cells* ***(D and E)*** *at day 0-7 after injection in 0.5-2 mg/mL collagen gels polymerized at 37°C and after injection in 1 mg/mL collagen gels polymerized at 4°C or 37°C, respectively. Data presented as mean ± standard error.*

our results on cell phenotype with respect to substrate modification illustrate the difference in cell behavior that might be an early indicator of the cell line dependent preference for metastatic niche.

5.3.2 Cell invasion in 3D is stiffness dependent

Given our finding that the chemical composition of the surface leads to different cellular response of the two cell lines, we explored whether and how the mechanical characteristics of the environment determined their migratory phenotype. 3D migration assays in collagen gels were performed on both 6647 and CHP100 cells. Gels with elastic modulus up to 230 Pa (Paszek et al., 2005), were prepared. Cells were injected

into gels and imaged 1, 2, 3, 4 and 7 days after injection. We used 0.5, 1 and 2 mg/mL collagens gels polymerized at 4°C or 37°C. Highly concentrated cell suspension was injected into the gels creating spheroids of 60-75 μm radius (Supplemental Fig. S2A). Time-laps DIC-images were subsequently taken from those spheroids for further analysis.

Initially we analyzed the number of the cells that escaped from the spheroids. Escaped cells were identified as described in Materials and Methods section. The results of the analysis for 6647 cells are summarized in Figure 5.2B-E. The number of escaped cells increased with time and decreased with gel stiffness. Assuming a linear relationship during the 7-days observation window, we found an escape rate of 21, 4, and 1 cells/day, for gels prepared from 0.5, 1 and 2 mg/mL collagen at 37°C, respectively (Fig. 5.2B). It should be noted that changes in the concentration of collagen not only results in a variation of the stiffness, but also the gel microstructure, in particular its pore size differs (Raub et al., 2007; Wolf et al., 2013) : the smaller the concentration of collagen the bigger the pore size. Therefore, we created soft and stiff gels in which the collagen concentration was kept constant (1 mg/ml). In this way the collagen density was kept constant while the stiffness varied from soft to stiff, at temperatures of 4 to 37°C respectively. Like in the experiments in which the colagen concentration was varied, the initial escape rate decreased in stiffer gels from 11 to 7 cells/day (Fig. 5.2C).

Further, we analyzed the migratory behavior of cells. We followed the distance distribution of cells that escaped with respect to the initial border of the spheroid in time. Data are shown for the mean distance of escaped 6647 cells from 0 to 7 days after injection (Fig. 5.2D,E). Next to the increased escape rate, cells exhibited an enhanced migratory behavior in softer gels. We found that the mean distance increased linear with time after injection, which suggests that cell migration was directed in the outward direction and not governed by a diffusion. For the latter one would predict that the mean squared-distances scale linear in time, which contradicts our experimental findings (Fig. S2B,C). The drift velocity was 36, 30, and 21 μm/day, for gels prepared at 37°C from 0.5, 1 and 2 mg/mL collagen, respectively (Fig. 5.2D). Our data suggest, that the velocity of cell migration was primarily defined by the collagen density. Accordingly, the initial drift velocity for gels that were prepared at 4 and 37°C was similar - 38 and 41 mg/day, respectively (Fig. 5.2E), implying that the increased number of escaped cells was not related to

the cell migration velocity, but primary determined by probability to detach from the spheroid, which was defined by the stiffness of the gel.

CHP100 cells showed a similar, yet overall reduced migratory behavior with respect to gel stiffness and pore size (supplemental Fig. S3A-D). Cells injected in 0.5 mg/mL collagen gels showed the largest rate of migratory cells of 16 cells/day (Fig. S3A), as well as the highest drift velocity of 38 μm/day (Fig. S3C). Notably the drift velocity was similar to that we found for 6647 cells. However, the onset of the migratory behavior, which was prompt (within 1 day) for 6647 cells, was delayed to $\sim$2 days for CHP100 cells (compare Fig. 5.2B,C with Fig. S3A,B).

In summary, our results suggest that the mechanical properties of the micro-environment modulates ES cell behavior. ES cells exhibit an enhanced migratory behavior in soft micro-environments independent of cell origin and metastatic niche. Likely this finding is a reflection of the preference to the gel stiffness rather than the pore size of the gel.

5.3.3 Ewing sarcoma cells change their mechanical phenotype on micropillar arrays of varying stiffness

For further support of our hypothesis we analyzed the response of Ewing sarcoma cells when the stiffness of the microenvironment was varied in a more controlled manner. We used elastomeric micropillar arrays of various heights to change the substrate stiffness without changing the chemistry, the network properties or the topology of the substrate (Tan et al., 2003). Micropillars of 2 μm diameter and heights of 3.2, 4.1 and 10 μm, corresponding to an effective array stiffness of 137.1, 47.2 and 7.5 kPa, were produced from poly(dimethylsiloxane). The micropillar arrays were stamped with fluorescencently-labeled Alexa647-conjugated fibronectin to enable visualization of the micropillars, and to allow cells to form specific adhesions on the micropillar tops. Cells plated onto the micropillars were incubated overnight, followed by cell fixation and immunostaining for paxillin and F-actin (Fig. 5.3A for 6647 cells, and Supplemental Fig. S4 for CHP100 cells).

For both cell lines we found a behavior that could be predicted from their behaviour on continuous substrates. 6647 cells grown on stiff, 47.2 and 137.1 kPa, micropillar arrays were small, areas of 300$\pm$20 and 310$\pm$15 μm^2 (Fig. 5.3A,B), and only weakly adherent. However, when grown on soft, 7.5 kPa, micropillar arrays, 6647 cells presented a fibroblast-like morphology (Fig. 5.3A) and significantly increased in size

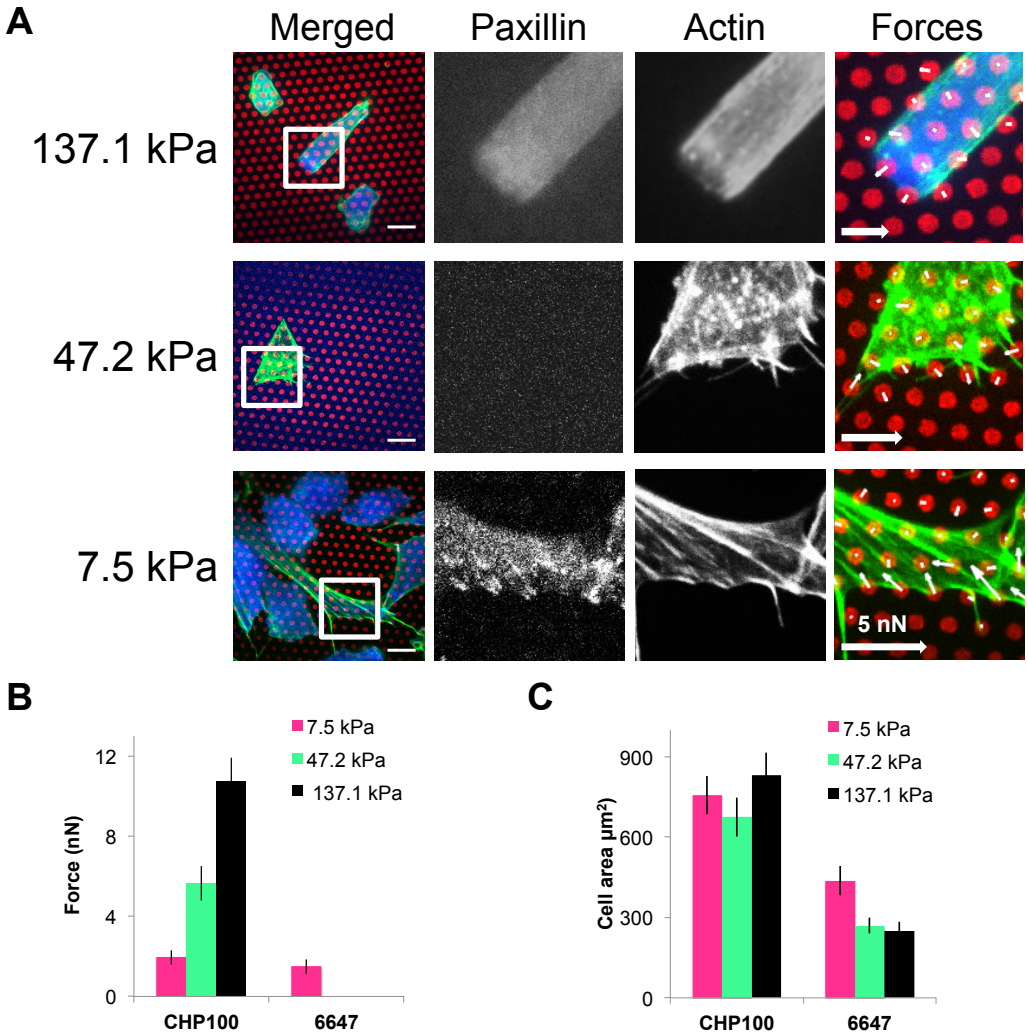

Figure 5.3
Ewing sarcoma cells on micropillars. ***A.*** *Confocal images of the 6647 cells placed on the micropillars of various stiffness. Pseudo colors represent fibronectin/micropillar tops (red), actin (green) and paxillin (blue). The scale bar - 10 µm; force scale bar (arrow) - 20 nN, if not indicated otherwise.* ***B.*** *Average cell area detected for CHP100 and 6647 cells.* ***C.*** *Maximum probable forces determined for CHP100 and 6647 cells on the micropillars of different stiffness.*

to 470±20 μm^2 (Fig. 5.3B). On stiff substrates, the morphological phenotypes were paralleled by the inability to form cell-matrix adhesions (no paxillin recruitment, Fig. 5.3A) and the inability to apply forces (Fig. 5.3A,C). On soft, 7.5 kPa, substrates paxillin was recruited to elongated patches characteristic for cell-matrix adhesions (Fig. 5.3A), and cells applied a mean force of 1.5±0.4 nN to individual micropillars (Fig. 5.3A,C).

The morphology (Fig. S4) and cell area (900±50, 760±50 and 850±40 μm^2) was independent of substrate stiffness (137.1, 47.2 and 7.5 kPa, respectively) for CHP100 cells (Fig. 5.3B). On substrates of all stiffnesses, paxillin was recruited to form clearly developed cell-matrix adhesions coupled to actin stress fibers (Fig. S4A). Forces increased with substrate stiffness (Fig. S4B and Fig. 5.3C). The force distributions shown in Fig. 5.3C were characterized by their most probable force for individual micropillars of 2.0±0.4, 5.6±0.8 and 10.7±1.1 nN for substrate stiffness of 7.5, 47.2 and 137.1 kPa, respectively (Fig. S4B). Hence, although the morphological phenotype of CHP100 cells was unchanged, a mechanical phenotype developed in which the cellular forces increased with the stiffness of the substrate. Such behavior has been reported for various cell types including fibroblasts (Balcioglu et al., 2015).

Taken together our results confirm the hypothesis that the two cell lines develop into mechanically divergent phenotypes, which react on the mechanical properties of their environment. Whereas 6647 cells favored soft surfaces CHP100 cells showed no preference, however reacted on stiffer substrates with higher forces.

5.3.4 Dynamic force development depends on substrate stiffness

We further characterized the dynamics of force built-up and release in a live-cell setting. For visualization we stably transfected 6647 cells with LifeAct-mCherry (further referred to as 6647-mCherry), which allowed us to image the dynamics of the actin network. Similar to the fixed-cell experiments, micropillars were fluorescently labeled with Alexa405-conjugated fibronectin to allow for the force readout. Cells were incubated overnight on soft (7.5 kPa) and stiff (137.1 kPa) micropillar arrays. On the stiff arrays approximately 50% of the 6647-mCherry spheroids adhered to the micropillar surface (data not shown). Only very few cells escaped from the spheroids. Those individual cells were further analyzed

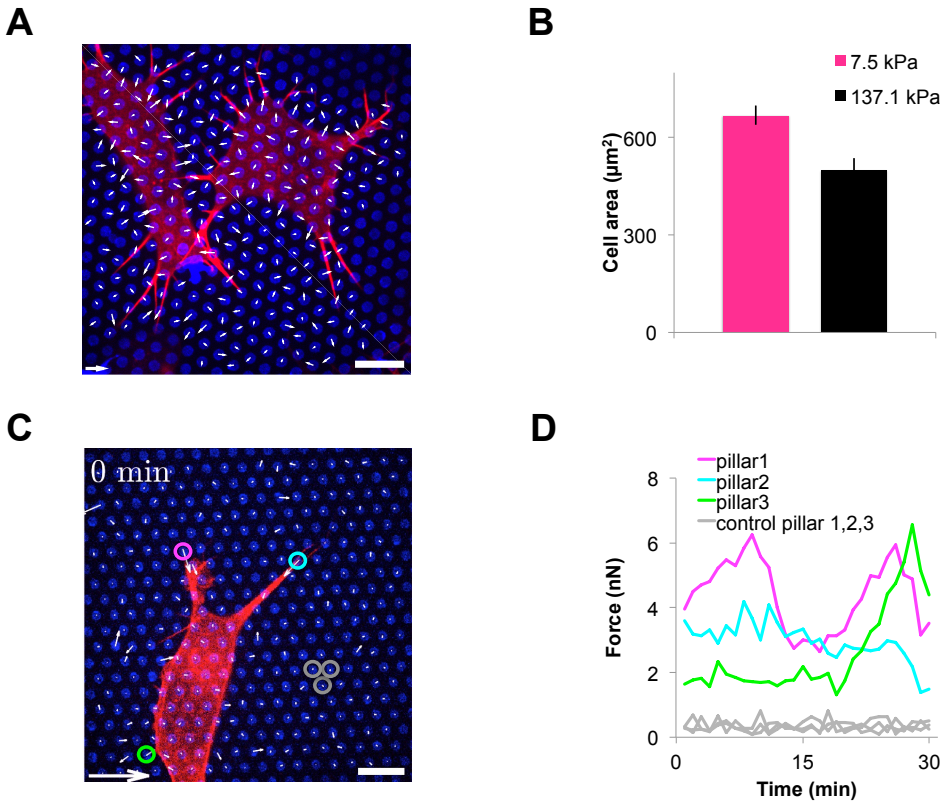

Figure 5.4
Life imaging of 6647-mCherry cells on the micropillars. ***A.*** *Confocal image of the 6647-mCherry cells on 137.1 kPa micropillars after overnight incubation. Pseudo colors correspond to fibronectin/micropillar tops (blue) and actin (red).* ***B.*** *Cell area determined at micropillars of different stiffness.* ***C.*** *6647-mCherry on 7.5 kPa micropillars.* ***D.*** *Time trace of the forces applied to individual micropillars (pink, blue and green) and control micropillars (grey). The scale bar - 10 µm; force scale bar (arrow) - 20 nN.*

in terms of single-cell and single-micropillar forces. The slight differences in morphology when compared to the results on fixed cells presumably reflect fixation artefacts: the morphology of the cells appeared more spread with a mean cell area of 500±35 (compare Fig. 5.3B with Fig. 5.4B). As in the fixed-cell setting 6647-mCherry cells did not exert any detectable forces (Fig. 5.4A), even no short transients, which could have been overlooked in the fixed cell setting.

On soft micropillar arrays the live-cell experiments also confirmed our findings on fixed cells. For individual cells which spread out from the initial spheroids, the cell morphology was significantly larger when com-

pared to hard substrates with a mean cell area of 670±30 μm^2. Spread cells applied mean forces of 2.1±0.4 nN on individual micropillars (Fig. 5.5D). The increase in force from 1.5 to 2.1 nN when compared to fixed cells is an observation that has been reported earlier and attributed to cell fixation (Balcioglu et al., 2015). The live-cell setting subsequently allowed us to directly observe the built-up and release of cellular forces. Force built-up and release was observed to occur on a similar timescale characterized by a rate of 0.4±0.2 nN/min and a typical half time of $t_{1/2}$= 4.2±0.3 min. This timescale was comparable to that we earlier found for a fibroblast cell line of $t_{1/2}$ ≈3 minutes (not published). Presumably this implies that initiation of ES cells migration is similar to that found for cell motility of fibroblasts.

5.3.5 Activation of cells did not alter their morphological and mechanical phenotype

Many cancer cells, including Ewing sarcoma, are characterized by a significant overexpression of the chemokine receptor CXCR4. Overexpression of CXCR4 was found to be strongly correlated with the metastastatic state and invasiveness of cells (Bennani-Baiti et al., 2010). Both cell lines, 6647 and CHP100, investigated here, were reported for their high expression level of CXCR4 (Sand et al., in print). Hence, we addressed the hypothesis whether stimulation of CXCR4 would result in higher motility and potentially associated increased force phenotype.

Migration of 6647 cells in 1 mg/mL collagen gels that were polymerized at either 4°C or 37°C did not show any significant difference in the number of cells which escaped from the spheroid for global stimulation with 100 nM CXCL12 (Fig. 5.5A). This finding suggested that activation of CXCR4 did not induce enhanced cell migration. The result for 3D gels was in agreement with our experiments on Ewing sarcoma cells on 2D substrates (data not shown), but in contrast to other findings which indicated that CXCR4 overexpression enhanced 2D migratory behavior of ES cells (Jin et al., 2012; Krook et al., 2014). Further, we did not observe any significant change in the force application neither on stiff (137.1 kPa, Fig. 5.5B) nor on soft (7.5 kPa) micropillars (Fig. 5.5C,D), respectively.

Hence, activation of the CXCR4 receptor did not alternate the response of ES cells on the stiffness of their micro-environment, at least within the 24 hours timescale of the current experiment, implying that

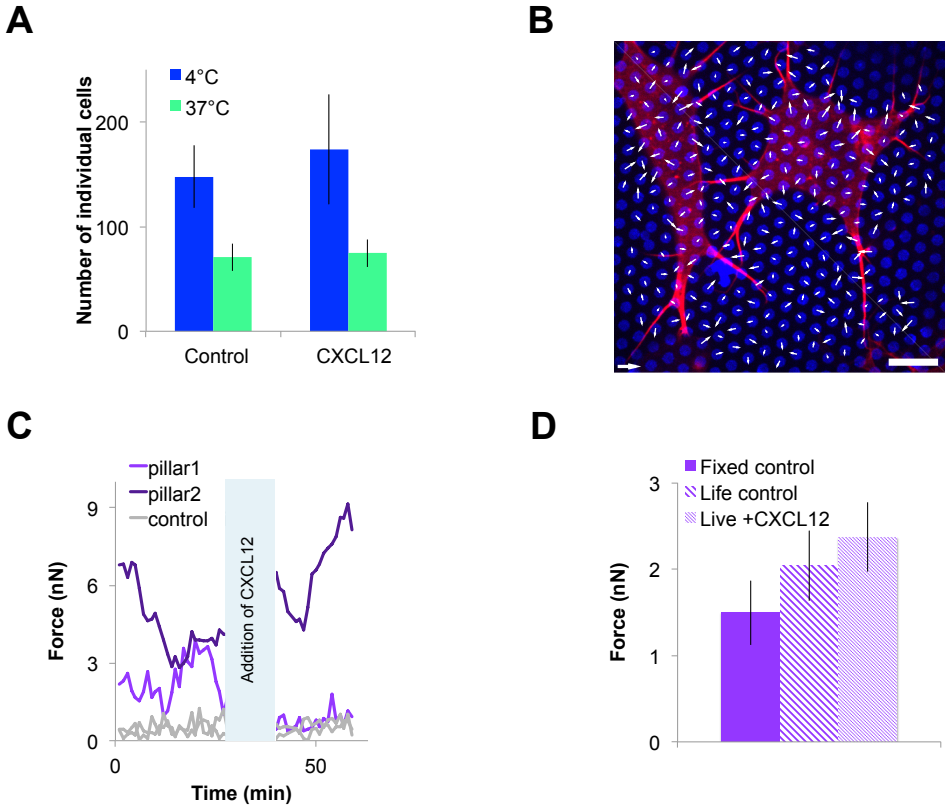

Figure 5.5

Influence of CXCR4 activation on 6647 response to the stiffness. ***A.*** *Comparison of the number of the cells escaped from the spheroid at day 3 after injection in 1 μg/mL collagen gels polymerized at 4°C or 37°C with and without CXCL12 in the medium.* ***B.*** *Confocal image of the 6647-mCherry cells on 137.1 kPa micropillars 15 minutes after CXCL12 addition. Pseudo colors correspond to fibronectin/micropillar tops (blue) and actin (red). The scale bar - 10 μm; force scale bar (arrow) - 20 nN.* ***C.*** *Time trace of the forces applied by 6647-mCherry cells to individual 7.5 kPa micropillars (purple) and control micropillars (grey) before and after CXCL12 stimulation.* ***D.*** *Maximum probable forces determined on the 7.5 kPa micropillars under different conditions.*

mechanosensing and response to micro-environment stiffness is not correlated with CXCR4 signaling in ES cells.

5.4 Discussion

Ewing sarcoma is a cancer, which develops in bone and soft tissue. The cell of origin for Ewing sarcoma is so-far unknown (Ludwig, 2008). There is however evidence indicating that Ewing sarcoma derives from cells determined to become neuronal or pluripotent cells that show blocked differentiation (Kovar, 2005). Some cell lines established from primary tumors were initially characterized as neuroblastoma (Bernal et al., 1983; Schlesinger et al., 1976) or rhabdomyosarcoma (Giard et al., 1973; Martinez-Ramirez et al., 2003), but later characterized as Ewing sarcoma by analysis for the EWS/FLI expression (Giard et al., 1973; Martinez-Ramirez et al., 2003). The Ewing sarcoma develops in the bone, and the primary site of metastasis are the lungs, with other metastatic niches have been found to be the bone and bone marrow. Hence, the microenvironment of the primary tumor (stiffness 100 kPa; Engler et al., 2006; Moore et al., 2010) is significantly more stiff than that of the metastasis site ($\sim$2 kPa for lungs; Booth et al., 2012). This observation spurred our investigation, to identify a potential role of mechanosensing in Ewing sarcoma metastasis. We hypothesized that mechanical cues could lead to guidance of Ewing sarcoma cells towards their site of metastasis. A similar modulation of the cellular mechanical phenotype was achieved via alternation of the substrate stiffness for other cell types (Engler et al., 2006). Our hypothesis was supported by reports that adhesion of the Ewing sarcoma cells is largely modulated by the chimeric protein EWS/FLI. EWS/FLI expression was found to cause a loss of organized actin stress fibers, focal adhesion and cell spreading (Chaturvedi et al., 2012, 2014).

In order to find a correlation between mechanical phenotype and metastatic niche of Ewing sarcoma cells we compared cells derived from patients with metastasis localized in lungs (6647) or in bone (CHP100). These two cell lines showed a significant difference in response to changes in the mechanical properties of their microenvironment both in 2D and 3D. 6647 cells, showed a clear preference to softer substrate. Similar to other ES cells (Kodama et al., 1991) 6647 migrated best in soft substrates. Furthermore, 6647 cells exhibited a different cell morphology on

the softer substrate: cells were more spread and showed indications of paxillin recruitment as well as actin stress fiber formation, all indicators of stronger cell adherence. Remarkably, such alteration in cell morphology on the soft substrates is in contrast with findings for fibroblasts and other cell lines, which spread significantly better on stiff as compared to soft gels (Paszek et al., 2005). Likewise, 6647 cells showed force application only when placed on softest substrate, while many other cell lines, including CHP100, exhibit increased contractile forces when cultured on stiffer matrices. Additionally, in contrast to 6647, CHP100 cells did not show any strong substrate-stiffness dependence in their morphological or migratory behavior. Hence, our results point to a correlation between cellular response to the substrate stiffness and Ewing sarcoma metastasis localization. Thereby, suggesting that Ewing sarcoma cells could be following a mechanical cue when choosing the site for metastasis formation.

Taken that both cell lines showed reduced migration in stiffer 3D gels, one could argue that lack of migration of ES cells in stiff microenvironment would severely obstruct their escape into the blood stream as an initial step in metastatic development. However, following Chaturvedi et al. due to the tumor localization Ewing sarcoma cells have an easy access to the intravascular space and do not need active cell migration (Chaturvedi et al., 2012). It is tempting to speculate on the further mechanism of ES metastasis. Taken that both, our results and findings of other groups, showed anchorage-independent growth of ES cells (Landuzzi et al., 2000), in the blood stream individual cells would probably further form spheroids. Spheroids would be easily transported through the body, eventually acquiring a critical size that would jam in the smallest capillaries. Further, as our data suggest that, 6647 cells would only escape the speroid in soft tissue, e.g lungs ($\sim$2 kPa), but not in stiff tissues like kidney ($\sim$4 kPa; Bensamoun et al., 2011) or bone (100 kPa). Thus, for 6647 cells lungs are the preferential site for metastasis. In contrast, CHP100 cells which do not change migratory phenotype with substrate stiffness, but increase their force application and concomitantly strengthen their adhesion with increasing stiffness, would suggest their tendency to metastasise into the hardest environments of the body, i.e. bone.

In summary, our results point out that the mechanical properties of the microenvironment does modulate Ewing sarcoma cell morphology and mechanical phenotype. Our model imply that mechanosensing is

potentially one of key regulators during Ewing sarcoma metastasis and has a great impact on directing cells to their specific metastasis site.

5.5 Supplemental figures

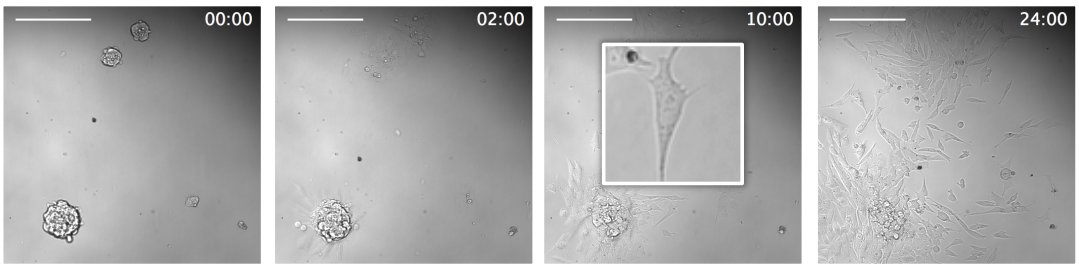

Figure S1
6647 cells growing on the plastic petri dish coated with fibronectin followed for 24 hours after plating. Scale bar - 100 μm; time shown in hours; inserts - 8 times zoom in.

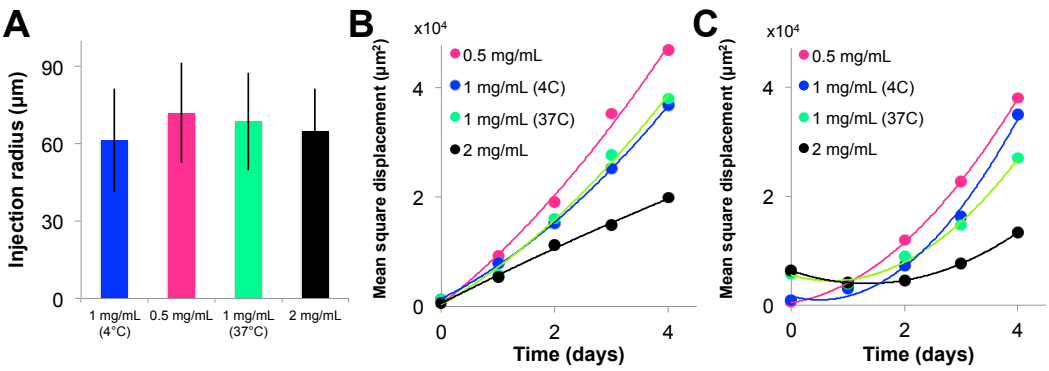

Figure S2
Comparison of the injected spheroids at day 0 ***A.****and the average square displacement of individual 6647* ***B.*** *and CHP100* ***C.*** *cells at day 0-7 after injection in 0.5-2 mg/mL collagen gels polymerized at 37°C and after injection in 1 mg/mL collagen gels polymerized at 4°C or 37°C, respectively.*

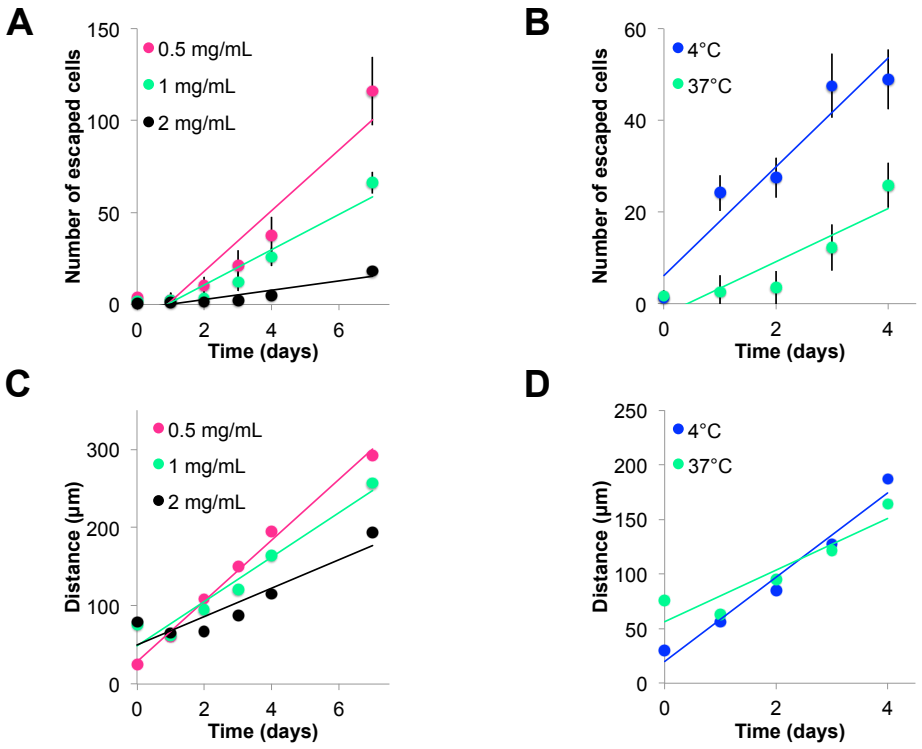

Figure S3

Comparison of the number of the cells escaped from the spheroid ***(A and B)*** *and the average distance migrated by individual cells* ***(C and D)*** *at day 0-7 after injection in 0.5-2 mg/mL collagen gels polymerized at 37°C and after injection in 1 mg/mL collagen gels polymerized at 4°C or 37°C, respectively.*

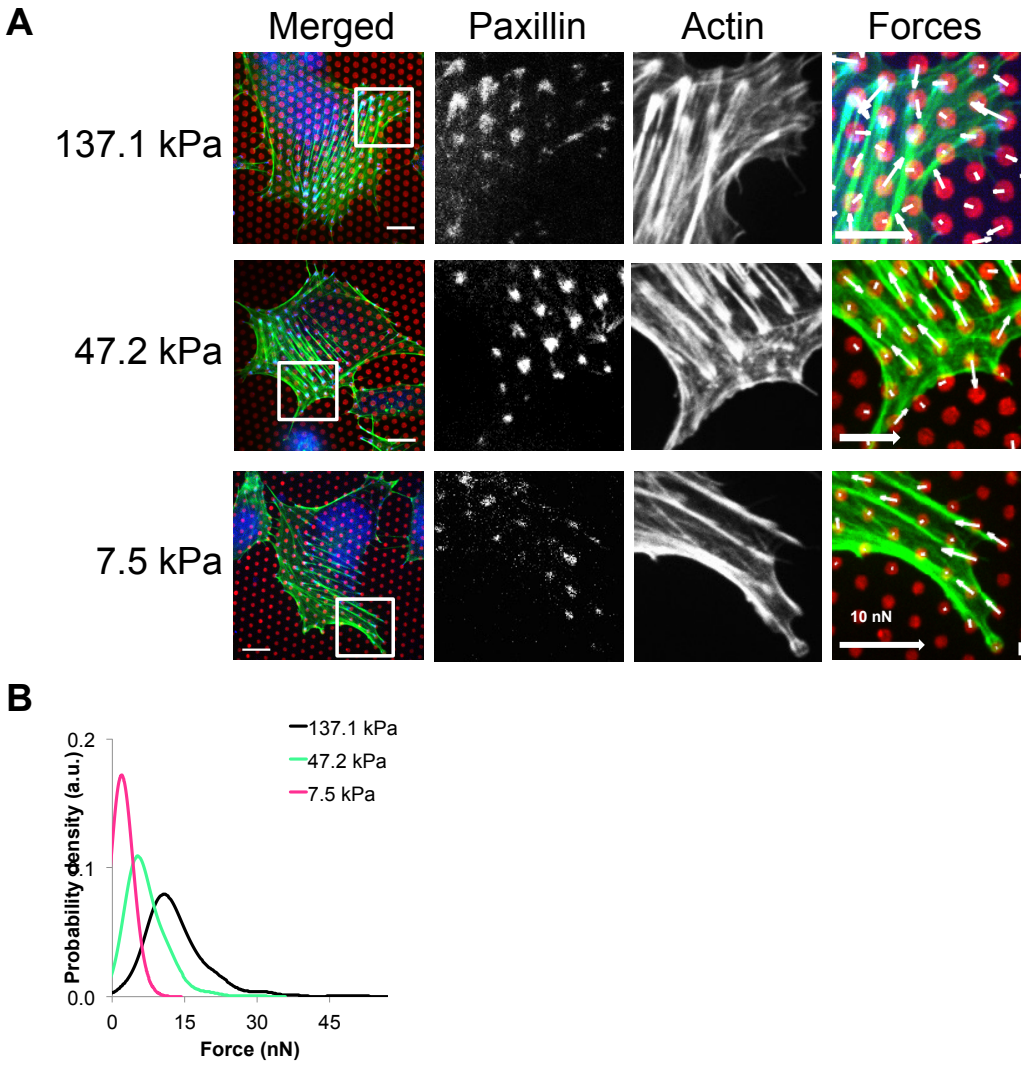

Figure S4

CHP100 cells on micropillars. ***A.*** *Confocal images of the CHP100 cells placed on the micropillars of various stiffness. Pseudo colors represent febronectin/micropillar tops (red), actin (green) and paxillin (blue). The scale bar - 10 μm; force scale bar (arrow) - 20 nN, if not indicated otherwise.* ***B.*** *Distribution of the probability density of the forces detected for CHP100 cells on micropillars of various stiffness.*

5.6 References

Balcioglu, H.E., van Hoorn, H., Donato, D.M., Schmidt, T., and Danen, E.H. (2015). The integrin expression profile modulates orientation and dynamics of force transmission at cell-matrix adhesions. J. Cell. Sci. 128, 1316-1326.

Bennani-Baiti, I.M., Cooper, A., Lawlor, E.R., Kauer, M., Ban, J., Aryee, D.N., and Kovar, H. (2010). Intercohort gene expression co-analysis reveals chemokine receptors as prognostic indicators in Ewing's sarcoma. Clin. Cancer Res. 16, 3769-3778.

Bensamoun, S.F., Robert, L., Leclerc, G.E., Debernard, L., and Charleux, F. (2011). Stiffness imaging of the kidney and adjacent abdominal tissues measured simultaneously using magnetic resonance elastography. Clin Imaging 35, 284-287.

Bernal, S., Thompson, R., Gilbert, F., and Baylin, S.B. (1983). In vitro and in vivo growth characteristics of two different cell populations in an established line of human neuroblastoma. Cancer Res. 43, 1256-1260.

Booth, A.J., Hadley, R., Cornett, A.M., Dreffs, A.A., Matthes, S.A., Tsui, J.L., Weiss, K., Horowitz, J.C., Fiore, V.F., Barker, T.H., et al. (2012). Acellular normal and fibrotic human lung matrices as a culture system for in vitro investigation. Am. J. Respir. Crit. Care Med. 186, 866-876.

Chaturvedi, A., Hoffman, L.M., Welm, A.L., Lessnick, S.L., and Beckerle, M.C. (2012). The EWS/FLI Oncogene Drives Changes in Cellular Morphology, Adhesion, and Migration in Ewing Sarcoma. Genes Cancer 3, 102-116.

Chaturvedi, A., Hoffman, L.M., Jensen, C.C., Lin, Y.-C.C., Grossmann, A.H., Randall, R.L., Lessnick, S.L., Welm, A.L., and Beckerle, M.C. (2014). Molecular dissection of the mechanism by which EWS/FLI expression compromises actin cytoskeletal integrity and cell adhesion in Ewing sarcoma. Mol. Biol. Cell 25, 2695-2709.

Chaudhuri, O., Koshy, S.T., Branco da Cunha, C., Shin, J.-W.W., Verbeke, C.S., Allison, K.H., and Mooney, D.J. (2014). Extracellular matrix stiffness and composition jointly regulate the induction of malignant phenotypes in mammary epithelium. Nat Mater 13, 970-978.

Engler, A.J., Sen, S., Sweeney, H.L., and Discher, D.E. (2006). Matrix elasticity directs stem cell lineage specification. Cell 126, 677-689.

Erkizan, H.V., Uversky, V.N., and Toretsky, J.A. (2010). Oncogenic

partnerships: EWS-FLI1 protein interactions initiate key pathways of Ewing's sarcoma. Clin. Cancer Res. 16, 4077-4083.

Giard, D.J., Aaronson, S.A., Todaro, G.J., Arnstein, P., Kersey, J.H., Dosik, H., and Parks, W.P. (1973). In vitro cultivation of human tumors: establishment of cell lines derived from a series of solid tumors. J. Natl. Cancer Inst. 51, 1417-1423.

Giovannini, Biegel, Serra, Wang, Wei, Nycum, Emanuel, and Evans (1994). EWS-erg and EWS-Fli1 fusion transcripts in Ewing's sarcoma and primitive neuroectodermal tumors with variant translocations. J. Clin. Invest.

Van Hoorn, H., Harkes, R., Spiesz, E.M., Storm, C., van Noort, D., Ladoux, B., and Schmidt, T. (2014). The nanoscale architecture of force-bearing focal adhesions. Nano Lett. 14, 4257-4262.

Jin, Z., Zhao, C., Han, X., and Han, Y. (2012). Wnt5a promotes ewing sarcoma cell migration through upregulating CXCR4 expression. BMC Cancer 12, 480.

Kodama, K., Doi, O., Higashiyama, M., Mori, Y., Horai, T., Tateishi, R., Aoki, Y., and Misawa, S. (1991). Establishment and characterization of a new Ewing's sarcoma cell line. Cancer Genet. Cytogenet. 57, 19-30.

Kovar, H. (2005). Context matters: the hen or egg problem in Ewing's sarcoma. Semin. Cancer Biol. 15, 189-196.

Krook, M.A., Nicholls, L.A., Scannell, C.A., Chugh, R., Thomas, D.G., and Lawlor, E.R. (2014). Stress-induced CXCR4 promotes migration and invasion of ewing sarcoma. Mol. Cancer Res. 12, 953-964.

Landuzzi, L., De Giovanni, C., Nicoletti, G., Rossi, I., Ricci, C., Astolfi, A., Scopece, L., Scotlandi, K., Serra, M., Bagnara, G.P., et al. (2000). The metastatic ability of Ewing's sarcoma cells is modulated by stem cell factor and by its receptor c-kit. Am. J. Pathol. 157, 2123-2131.

Liou, Y.-R.R., Torng, W., Kao, Y.-C.C., Sung, K.-B.B., Lee, C.-H.H., and Kuo, P.-L.L. (2014). Substrate stiffness regulates filopodial activities in lung cancer cells. PLoS ONE 9, e89767.

Ludwig, J.A. (2008). Ewing sarcoma: historical perspectives, current state-of-the-art, and opportunities for targeted therapy in the future. Curr Opin Oncol 20, 412-418.

Martinez-Ramirez, A., Rodriguez-Perales, S., MelÃ©ndez, B., Martinez-Delgado, B., Urioste, M., Cigudosa, J.C., and Benitez, J. (2003). Characterization of the A673 cell line (Ewing tumor) by molecular cytogenetic techniques. Cancer Genet. Cytogenet. 141, 138-142.

Mierke, C.T. (2013). Physical break-down of the classical view on cancer cell invasion and metastasis. Eur. J. Cell Biol. 92, 89-104.

Moore, S.W., Roca-Cusachs, P., and Sheetz, M.P. (2010). Stretchy proteins on stretchy substrates: the important elements of integrin-mediated rigidity sensing. Dev. Cell 19, 194-206.

Ottaviano, L., Schaefer, K.-L.L., Gajewski, M., Huckenbeck, W., Baldus, S., Rogel, U., Mackintosh, C., de Alava, E., Myklebost, O., Kresse, S.H., et al. (2010). Molecular characterization of commonly used cell lines for bone tumor research: a trans-European EuroBoNet effort. Genes Chromosomes Cancer 49, 40-51.

Park, J.S., Chu, J.S., Tsou, A.D., Diop, R., Tang, Z., Wang, A., and Li, S. (2011). The effect of matrix stiffness on the differentiation of mesenchymal stem cells in response to TGF-β. Biomaterials 32, 3921-3930.

Paszek, M.J., Zahir, N., Johnson, K.R., Lakins, J.N., Rozenberg, G.I., Gefen, A., Reinhart-King, C.A., Margulies, S.S., Dembo, M., Boettiger, D., et al. (2005). Tensional homeostasis and the malignant phenotype. Cancer Cell 8, 241-254.

Raub, C.B., Suresh, V., Krasieva, T., Lyubovitsky, J., Mih, J.D., Putnam, A.J., Tromberg, B.J., and George, S.C. (2007). Noninvasive assessment of collagen gel microstructure and mechanics using multiphoton microscopy. Biophys. J. 92, 2212-2222.

Sand, L.G., Szuhai, K., and Hogendoorn, P.C. (2015). Sequencing Overview of Ewing Sarcoma: A Journey across Genomic, Epigenomic and Transcriptomic Landscapes. Int J Mol Sci 16, 16176-16215.

Schlesinger, H.R., Gerson, J.M., Moorhead, P.S., Maguire, H., and Hummeler, K. (1976). Establishment and characterization of human neuroblastoma cell lines. Cancer Res. 36, 3094-3100.

Schrader, J., Gordon-Walker, T.T., Aucott, R.L., van Deemter, M., Quaas, A., Walsh, S., Benten, D., Forbes, S.J., Wells, R.G., and Iredale, J.P. (2011). Matrix stiffness modulates proliferation, chemotherapeutic response, and dormancy in hepatocellular carcinoma cells. Hepatology 53, 1192-1205.

Tan, J.L., Tien, J., Pirone, D.M., Gray, D.S., Bhadriraju, K., and Chen, C.S. (2003). Cells lying on a bed of microneedles: an approach to isolate mechanical force. Proc. Natl. Acad. Sci. U.S.A. 100, 1484-1489.

Whang-Peng, J., Triche, T.J., Knutsen, T., Miser, J., Kao-Shan, S., Tsai, S., and Israel, M.A. (1986). Cytogenetic characterization of selected

small round cell tumors of childhood. Cancer Genet. Cytogenet. 21, 185-208.

Wolf, K., Te Lindert, M., Krause, M., Alexander, S., Te Riet, J., Willis, A.L., Hoffman, R.M., Figdor, C.G., Weiss, S.J., and Friedl, P. (2013). Physical limits of cell migration: control by ECM space and nuclear deformation and tuning by proteolysis and traction force. J. Cell Biol. 201, 1069-1084.

Summary

The first description of cancer dates back to the ancient Papyrus Ebers in 1500 B. C. The term 'metastasis', the uncontrolled cell growth at distant sites, was first introduced by Lobstein in the beginning of 19th century. In 1889 Stephen Paget suggested a predisposition for sites of metastasis based on 735 fatal cases of breast cancer in multiple reports. He introduced the 'seed and soil' concept, where 'seeds' are the cancer cells with metastatic capacities, and 'soil' is the tissue or organ providing the proper microenvironment for growth. To date this concept is widely accepted with a stunning amount of molecular insights, which have led to a better understanding of both the 'seed' and the 'soil'.

Ewing sarcoma, discovered in 1921, is a neoplasm in the bone, which forms metastasis even at an early stage of tumor development. The development of metastasis is correlated with poor patient prognosis and, hence, low long-term survival rate. Interestingly, Ewing sarcoma metastasis exhibits a well-defined distribution along the body. Ewing sarcoma metastasis is predominantly restricted to the lungs, followed by bone/bone marrow localization. In some cases simultaneous combined lung/bone/bone marrow metastasis localization have been reported. Metastatic sites in other locations rarely occur. As such, the microenvironment of Ewing sarcoma metastasis can be either that of the primary tumor (bone) or it can be drastically different (lung). Hence, the consistency of Ewing sarcoma metastasis localization implies a cellular predisposition.

Many studies attempted to obtain an understanding of the mechanism underpinning the metastatic behavior of Ewing sarcoma. The metastatic capacity was found to be correlated with the expression of the chemokine receptor CXCR6, the G-protein coupled receptor GPR64, increased level of interleukin 6, Caveolin 1, IGF-1R and an enhanced activity of the metalloproteinases 2 and 9. A special role was attributed

to the chemokine receptor CXCR4, which is overexpressed in metastatic Ewing sarcoma, and is regulated by the Ewing sarcoma-specific fusion protein EWS/FLI1. EWS/FLI1 was previously shown to modulate the architecture and integrity of the cytoskeleton, which is viewed as further prerequisite for ES metastasis. Although a significant amount of data is available, a comprehensive model of Ewing sarcoma metastasis is yet to be developed. In this thesis the biochemical and biophysical factors involved in Ewing sarcoma metastasis are further explored.

In **Chapter 2** a single-molecule imaging technique was applied to examine the dynamics of the chemokine receptor CXCR4 on the plasma membrane of an Ewing sarcoma-derived cell line (A673). The CXCR4 mobility on the plasma membrane was detected at 30 nm positional accuracy and 50 ms temporal resolution. This temporal and positional resolution enabled distinguishing different mobility fractions/states of CXCR4 and following the transition between the mobile and immobile state of the receptor upon different conditions. Immobilization of CXCR4 occurred upon stimulation with its ligand CXCL12 in a concentration-dependent manner. The receptors' mobility change during activation appeared to be dependent on its signaling both through G-protein dependent and independent pathways. Signaling through G-proteins resulted in CXCR4 immobilization potentially into a supramolecular scaffold (signalosome), which could then enhance signaling. In contrast, activation of the G-protein independent pathway caused receptor immobilization into clathrin-coated vesicles leading to its internalization and, thus, receptor desensitization. As signaling through G-proteins appeared to interfere with receptor endocytosis, the findings of this study indicate a functional cross-talk between different biochemical cascades.

The involvement of G-protein activation in regulation of CXCR4 was further addressed in the study described in **Chapter 3**. The dynamics of two G_α subunits was examined in A673 cells. Both $G_{\alpha q}$ and $G_{\alpha i}$ exhibited a fast response on activation of CXCR4 by the formation of cluster-like structures. Single-molecule imaging revealed that the two G_α subunits follow a different coupling mode with the receptor. $G_{\alpha q}$ appeared pre-coupled to the receptor and exhibited uncoupling upon receptor activation. In contrast, $G_{\alpha i}$ was not coupled to CXCR4 prior to receptor activation and exhibited elevated coupling with the receptor upon stimulation with CXCL12. Such difference in coupling modes of $G_{\alpha q}$ and $G_{\alpha i}$ suggested a sequential coupling of the G-proteins to

CXCR4. This finding is in agreement with experiments that analyze the time needed for $G_{\alpha q}$ and $G_{\alpha i}$ to initiate downstream cascades. Taken that signaling through $G_{\alpha q}$ is a prerequisite for enhanced $G_{\alpha i}$ signaling, the ability of CXCR4 to subsequently activate both G_{α} subunits might act as a receptor signaling regulatory mechanism.

In **Chapter 4** the development of a light-activated chimeric receptor, usable for high temporally and spatially resolved activation and detection was described. The base construct was developed by exchange of the intracellular loops and C-terminus of the light-activated GPCR, rhodopsin, with the intracellular loops and the C-terminus of the chemokine receptor CXCR4. The cloning steps resulted in a chimeric receptor, optoCXCR4, which presumably was able to initiate CXCR4-specific signaling cascades by light-activation. The optoCXCR4 was further modified on both N- and C-terminals. All the constructs were tested for plasma membrane localization and functionality properties. A successful construct representing a promising tool for further biophysical investigation of chemokine receptor CXCR4 was developed. A key to proper functionality of the construct was the correct light-protection settings during all experimental procedures. The applicability of this promising approach in optogenetics was further discussed.

The involvement of the stiffness of the micro-environment in Ewing sarcoma metastasis was addressed in the study described in **Chapter 5**. The development of Ewing sarcoma in bones with metastasis sites to either bones or lungs, suggested the existence of a mechanical cue for Ewing sarcoma metastasis. This hypothesis was tested using Ewing sarcoma-derived cell lines, which preferred a largely disparate metastatic niche of bone (CHP100) and lungs (6647). In 2D and 3D assays 6647 cells exhibited a strong preference towards the mechanically soft micro-environment. Only on soft substrates 6647 cells were able to develop adhesions and developed an organized actin cytoskeleton. In contrast, CHP100 cells exhibited a higher adhesion potential on stiff substrates. Thus, the mechanical properties of the micro-environment caused a differential behavior of Ewing sarcoma cells of different metastatic profile. It was further evident that this mechanical phenotype was independent of CXCR4 receptor activation.

Taken together, the results presented in this thesis provide deeper insights into the mechanisms controlling signaling of the chemokine receptor CXCR4 and into the role of the micro-environment in Ewing sar-

coma cells behavior. Through various experimental approaches it was shown that both biochemical and biophysical guidance control how Ewing sarcoma develops into its distinct metastatic phenotype.

Samenvatting

De eerste omschrijving van kanker dateert uit het eeuwenoude Ebers Papyrus uit 1500 BC. De term 'metastase', ongecontroleerde groei van cellen op ver afgelegen locaties, werd voor het eerst geïntroduceerd door Lobstein in het begin van de 19e eeuw. Stephen Paget suggereerde in 1889 een aanleg voor metastase gebaseerd op 735 dodelijke gevallen van borstkanker in verscheidene verslagleggingen. Hij introduceerde het concept van 'zaad en voedingsbodem', waarbij 'zaden' de kankercellen zijn die metastatische capaciteit hebben en de 'voedingsbodem' het weefsel of orgaan aanduidt dat de micro-omgeving voor groei geeft. Tot op heden is dit concept wijdverspreid geaccepteerd met een indrukwekkende hoeveelheid aan moleculaire inzichten, welke hebben geleid tot een beter begrip van zowel de 'zaden' als de 'voedingsbodem'.

Ewing sarcoma, ontdekt in 1921, is een neoplasme in het bot, welke metastase vertoont op een vroeg tijdstip van de tumorontwikkeling. De ontwikkeling van metastase is gerelateerd aan een slechte prognose voor de patiënt en dus een lage overlevingskans op de lange termijn. Opmerkelijk is dat Ewing sarcoma metastase een goedgedefinieerde verdeling vertoont in het lichaam. Ewing sarcoma metastase is voornamelijk beperkt tot de longen, gevolgd door bot/beenmerg lokalisatie. In sommige gevallen wordt gelijktijdige long/bot/beenmerg metastase lokalisatie gerapporteerd. Metastase op andere locaties zijn zeldzaam. Zodoende kan de micro-omgeving van Ewing sarcoma metastase ofwel van de primaire tumor (bot) of heel erg verschillend (long) zijn. De consistentie van Ewing sarcoma lokalisatie impliceert daarmee een specifieke cellulaire voorkeur.

Vele studies probeerden het mechanisme achter het metastatisch gedrag van Ewing sarcoma te begrijpen. De metastatische aanleg bleek gecorreleerd te zijn met de expressie van de chemokine receptor CXCR6, de G-eiwit gekoppelde receptor GPR64, verhoogd niveau van interleukin

6, Caveolin 1, IGF-1R en een verhoogde activiteit van metalloproteinases 2 en 9. Een bijzondere rol werd toegekend aan de chemokine receptor CXCR4, welke tot overexpressie kwam in metastatische Ewing sarcoma, en is gereguleerd door het Ewing sarcoma-specifieke fusie-eiwit EWS/FLI1. Het was eerder aangetoond dat EWS/FLI1 de architectuur en integriteit van het cytoskelet moduleert, wat wordt gezien als een verdere voorwaarde voor Ewing sarcoma metastase. Hoewel een significante hoeveelheid data beschikbaar is, is een volledig model van Ewing sarcoma metastase nog niet ontwikkeld. In dit proefschrift worden de biochemische en biofysische factoren betrokken bij Ewing sarcoma metastase verder verkend.

In **Hoofdstuk 2** werd microscopie van enkele moleculen toegepast om de dynamische eigenschappen van chemokine receptor CXCR4 op het plasmamembraan van een Ewing sarcoma cellijn (A673) te onderzoeken. De mobiliteit van CXCR4 op het plasmamembraan werd gedetecteerd met 30 nm positienauwkeurigheid en 50 ms tijdsresolutie. Deze tijds- en positieresolutie maakte het mogelijk om verschillende fracties/toestanden van de mobiliteit van CXCR4 te onderscheiden en transities tussen mobiele en immobiele toe-standen van de receptor onder verschillende toestanden te volgen. Immobilisatie van CXCR4 vond plaats wanneer stimulatie met de ligand CXCL12 werd toegediend afhankelijk van de concentratie. De verandering van mobiliteit van de receptoren gedurende activatie leek afhankelijk te zijn van zowel signalen door G-eiwit afhankelijke en onafhankelijke cascades. Signalen via G-eiwitten resulteerden in CXCR4-immobilisatie mogelijk door een supramoleculair schavot (signalosoom), welke dan het signaal zou kunnen versterken. Activatie van de G-eiwit onafhankelijke cascade, daarentegen, veroorzaakte immobilisatie van de receptor in clathrin-bedekte blaasjes welke geïnternaliseerd werden met minder gevoeligheid voor de receptor als gevolg. Aangezien signalen door G-eiwitten belemmerd leken te worden door endocytose van receptoren, geven de resultaten van deze studie aan dat er een functionele overspraak is tussen verschillende biochemische cascades.

De betrokkenheid van G-eiwit activatie in de regulatie van CXCR4 werd verder geadresseerd in de studie die wordt beschreven in **Hoofdstuk 3**. De dynamica van twee G_α subunits werd onderzocht in A673 cellen. Zowel $G_{\alpha q}$ als $G_{\alpha i}$ toonden een snelle respons op activatie van CXCR4 door de vorming van clusterachtige structuren. Enkel-molecuul beeldvorming openbaarde dat de twee G_α subunits een verschillende kop-

pelingsmodus volgen met de receptor. $G_{\alpha q}$ leek al vooraf gekoppeld aan de receptor en toonde ontkoppeling wanneer de receptor activeerde. $G_{\alpha i}$, daarentegen, was niet gekoppeld aan CXCR4 voor receptor activatie en toonde toegenomen koppeling met de receptor wanneer er werd gestimuleerd met CXCL12. Een dergelijk verschil in koppelingsmoduli van $G_{\alpha q}$ en $G_{\alpha i}$ suggereerde een sequentiële koppeling van de G-eiwitten aan CXCR4. Deze bevinding is in overeenkomst met de experimenten die de benodigde tijd analyseerden voor $G_{\alpha q}$ and $G_{\alpha i}$ om verdere cascades te initiëren. Gezien signalen via $G_{\alpha q}$ een vereiste zijn voor versterkte $G_{\alpha i}$ signalen is het vermogen van CXCR4 om beide G_{α} subunits te activeren wellicht een regulerend mechanisme voor het signaal van de receptor.

In **Hoofdstuk 4** wordt de ontwikkeling van een licht-geactiveerde chimerische receptor omschreven, inzetbaar voor activatie en detectie met hoge tijds- en positieresolutie. Het basisconstruct werd ontwikkeld door de uitwisseling van de intracellulaire lussen van de licht-geactiveerde GPCR rhodopsin met de intracellulaire lussen en het C-uiteinde van de chemokine receptor CXCR4. De kloonstappen resulteerden in een chimerische receptor, optoCXCR4, welke vermoedelijk CXCR4-specifieke signaalcascades kon initiëren door middel van licht-activatie. De optoCXCR4 werd verder aangepast op zowel de N- als de C-uiteinden. Alle constructen werden getest op lokalisatie aan het plasmamembraan en op functionele eigenschappen. Een succesvol construct dat een veelbelovend werktuig voor verdere biofysische onderzoeken van chemoking receptor CXCR4 is werd ontwikkeld. Cruciaal voor de juiste functionaliteit van het construct was de correcte licht-beschermingsomstandigheden tijdens de experimentele procedures. De toepasbaarheid van deze veelbelovende aanpak in optogenetica werd verder bediscussieerd.

De afhankelijkheid van de stijfheid van de micro-omgeving van Ewing sarcoma metastase werd geadresseerd in de studie beschreven in **Hoofdstuk 5**. De ontwikkeling van Ewing sarcoma in botten met metastase naar ofwel bot of longen suggereerde een mogelijke mechanische invloed voor Ewing sarcoma metastase. Deze hypothese werd onderzocht met Ewing sarcoma-afgeleide cellijnen, welke de voorkeur toonden voor ver uiteen gelegen niches van bot (CHP100) en longen (6647). In 2D en 3D assays toonden 6647 cellen een sterke voorkeur voor een mechanisch zachte micro-omgeving. 6647 cellen konden alleen op zachte substraten aanhechtingen vormen en ontwikkelden een georganiseerd actine cytoskelet. CHP100 cellen, daarentegen, hechtten zich beter aan stij-

vere substraten. De mechanische eigenschappen van de micro-omgeving veroorzaakten dus een verschil in gedrag van Ewing sarcoma cellen uit een verschillend metastatisch profiel. Bovendien werd het duidelijk dat dit mechanische phenotype onafhankelijk was van CXCR4 receptor activatie.

De resultaten in dit proefschrift geven tezamen een dieper inzicht in de mechanismes achter zowel de signalen van CXCR4 als de micro-omgeving respons waarin cellulair gedrag van Ewing sarcoma cellen worden bepaald. Door verschillende experimentele methodes is aangetoond dat zowel biochemische als biofysische geleiding bepalen hoe Ewing sarcoma ontwikkelt naar een specifiek metastatisch phenotype.

Publications

1. ”CXCR4 signaling is controlled by immobilization at the plasma membrane”
   E. Beletkaia, S.F. Fenz, W. Pomp, E.B. Snaar-Jagalska, P.W.C. Hogendoorn, T. Schmidt
   under review at BBA - Molecular cell research

2. ”The mechanical phenotype of Ewing sarcoma cell lines predicts their metastatic niche”
   E. Beletkaia, O. Iendaltseva, H.E. Balcioglu, P.C.W. Hogendoorn, E.H.J. Danen, T. Schmidt
   in preparation

3. ”CXCR4-CXCL12 axis is conserved between zebrafish and humans and drives breast cancer micrometastasis formation in a zebrafish xenograft model”
   C. Tulotta, C. Stefanescu, E. Beletkaia, J. Busmann, T. Schmidt, B.E. Snaar-Jagalska
   in preparation

4. "Novel splice variants of CXCR4 identified by transcriptome sequencing"
   L.G. Sand, A.G. Jochemsen, E. Beletkaia, T. Schmidt, P.C.W. Hogendoorn, K. Szuhai
   Biochem. Biophys. Res. Commun., **466** (1), 89-94 (2015)

5. "Subcellular trafficking and transfection efficacy of polyethylenimine-polyethylene glycol polyplex nanoparticles with a ligand to melanocortin receptor-1."
   M. Durymanov, E. Beletkaia, A. Ulasov, Y. Khramtsov, G. Trusov, N. Rodichenko, T. Slastnikova, T. Vinogradova, N. Uspenskaya, E. Kopantsev, A. Rosenkranz, E. Sverdlov, A. Sobolev
   J. Control Release, **163** (2), 211-9 (2012)

6. "Investigation of transport and unpacking mechanisms of polyplexes for transfection efficiency on different cell lines"
   G. Trusov, A. Ulasov, E. Beletkaia, Y. Khramtsov, M. Durymanov, A. Rosenkranz, E. Sverdlov, A. Sobolev
   Dokl. Biochem. Biophys., **437** (1), 77 (2011)

Curriculum vitae

Elena Beleţkaia was born on May 4, 1989 in Chisinau, Moldova. She did her undergraduate studies at the Lomonosov Moscow State University (MSU) specializing in biophysics. She performed her pre-diploma and diploma projects in the Laboratory of Molecular Genetics at the Institute of Gene Biology under supervision of Prof. dr. A.S. Sobolev. During her diploma project she investigated physico-chemical properties of the polyethilenimine-based polyplexes and intracellular trafficking of polyplexes in different types of cells. In 2011 Elena successfully finished her diploma project and graduated from the MSU with a diploma with honors.

In September 2011 Elena Beleţkaia joined the group of Prof. dr. T. Schmidt as a PhD student. During her PhD research she focused on studying molecular mechanisms of various processes underlying metastasis of Ewing sarcoma. She presented results of her work at various international conferences in the USA, France, Germany, Austria, and the Netherlands. Through the time of her PhD Elena guided students during practical courses and during a bachelor project.

As her next step, Elena will join the group of Dr. D. Heinrich at Leiden University as a postdoctoral fellow.